3-22-2019

Aerial Simultaneous Localization and Mapping Using Earth's Magnetic Anomaly Field

Taylor N. Lee

Follow this and additional works at: https://scholar.afit.edu/etd

Part of the Navigation, Guidance, Control and Dynamics Commons

**Aerial Simultaneous Localization and Mapping
Using Earth's Magnetic Anomaly Field**

THESIS

Taylor Lee, 1st Lieutenant, USAF

AFIT-ENG-MS-19-M-039

**DEPARTMENT OF THE AIR FORCE
AIR UNIVERSITY**

AIR FORCE INSTITUTE OF TECHNOLOGY

Wright-Patterson Air Force Base, Ohio

AFIT-ENG-MS-19-M-039

AERIAL SIMULTANEOUS LOCALIZATION AND MAPPING USING

EARTH'S MAGNETIC ANOMALY FIELD

THESIS

Presented to the Faculty

Department of Electrical Engineering

Graduate School of Engineering and Management

Air Force Institute of Technology

Air University

Air Education and Training Command

in Partial Fulfillment of the Requirements for the

Degree of Master of Science in Electrical Engineering

Taylor Lee, B.S.E.E.

1st Lieutenant, USAF

March 21, 2019

AERIAL SIMULTANEOUS LOCALIZATION AND MAPPING USING

EARTH'S MAGNETIC ANOMALY FIELD

THESIS

Taylor Lee, B.S.E.E.
1st Lieutenant, USAF

Committee Membership:

Capt Aaron Canciani, PhD
Chair

Dr. Robert Leishman
Member

Dr. Clark Taylor
Member

Abstract

Instances of Global Positioning System (GPS) jamming and spoofing have identified the vulnerabilities of using GPS as a sole means of positioning, navigation, and timing (PNT) for the world's critical systems. A fusion of alternative positioning methods is necessary to replace the characteristics of GPS the world has become reliant upon. Aerial navigation using magnetic field crustal anomalies is a globally available, passively sensed, and nearly unjammable GPS-alternative positioning method. The Earth's outer core produces a magnetic field which is perturbed by magnetically susceptible materials in the Earth's crust. The resulting deviation from a core field reference model is a world-wide magnetic anomaly field shown to be a viable signal for navigation. This method required prior-surveyed magnetic anomaly maps of sufficient quality. Aerial geomagnetic surveys require more grid lines to fully sample the higher spatial variation of the magnetic anomaly field at low altitudes. This makes producing high-quality low-altitude magnetic maps expensive and therefore less common. The miniaturization of scalar magnetometers opened the potential for magnetic navigation on low-flying unmanned aerial vehicles (UAVs), which operate at altitudes lacking high quality magnetic maps. This motivated a method to remove magnetic navigation's dependency on a magnetic map. Indoor robotic and pedestrian magnetic navigation have employed simultaneous localization and mapping (SLAM) techniques to overcome this obstacle. This research extends SLAM concepts to eliminate the map dependency in aerial magnetic navigation. This research presents three main contributions. An aerial magnetic SLAM filter was designed which constrained the drift of an aircraft's inertial navigation system (INS) on a real flight-test dataset from 1 kilometer to tens of meters over a 100 minute flight without a prior magnetic

map. A commercial off-the-shelf (COTS) fixed-wing magnetic surveying UAV was configured and produced six consistent magnetic maps at various altitudes over a 2 kilometer area. The UAV's magnetic measurements were used to constrain three simulated INS grades to tens of meters over a 14 minute flight. Together, these three contributions demonstrated the viability of aerial magnetic navigation as a GPS alternative for manned aircraft and UAVs without requiring prior-surveyed magnetic maps.

Table of Contents

List of Figures

x

List of Tables

Acronyms

MEMS micro electro-mechanical systems. 4, 9, 12, 57–59, 61

MFAM micro-fabricated atomic magnetometer$^{\text{TM}}$. 57, 60–67, 71, 73, 74, 88

PMF probability mass function. 30

PNT positioning, navigation, and timing. iv, 2

PTP precision time protocol. 60

RBPF Rao-Blackwellized particle filter. 12, 13, 15, 25, 26, 39, 45, 46, 55, 86, 93

RMS root mean square. 52

SI ScatteredInterpolant. 48

SLAM simultaneous localization and mapping. iv, 1–5, 10–13, 15, 16, 24, 39–42, 45, 52, 55, 86–89, 92, 97, 101–103

sUAS small unmanned aerial systems. 2, 4, 39, 85, 87

UAV unmanned aerial vehicle. iv, v, 1–4, 8, 9, 14, 57, 58, 60, 62, 79, 81, 83–88, 97, 101, 102

AERIAL SIMULTANEOUS LOCALIZATION AND MAPPING USING EARTH'S MAGNETIC ANOMALY FIELD

I. Introduction

1.1 Overview

This document presents the progression of three research objectives aimed at conducting magnetic navigation on an unmanned aerial vehicle (UAV) without the aid of a prior magnetic map. The first step was the development of a navigation filter which simultaneously created a magnetic map and constrained inertial navigation system (INS) position errors. The second step was to configure and calibrate a UAV to collect magnetic measurements of the Earth's magnetic anomaly field using new miniaturized scalar magnetometers. The resulting UAV consistently measured the magnetic anomaly field within 2 nano-Teslas over a 2 kilometer by 1 kilometer area. The third step was to apply the navigation filter to the UAV magnetic measurements for simultaneous localization and mapping (SLAM).

The document is organized as follows. Chapter 1 explains the background of the problem, research objectives, and the limitations and assumptions made in this research. Chapter 2 is split into two parts. The first part is a review of previous works in relevant literature which has led to this research. The second part presents background information on Earth's magnetic field, aeromagnetic calibration, SLAM, non-linear stochastic state estimation, INS error modeling, and scattered data interpolation. Chapters 3, 4 and 5 are three papers. The first paper presents the results of aerial magnetic SLAM on a real flight test dataset with a full-sized manned aircraft.

The second paper presents the development, calibration, mapping capabilities of a UAV built by Air Force Institute of Technology (AFIT)'s Autonomy and Navigation Technology (ANT) center. The third paper presents the results of aerial magnetic SLAM on the UAV flight data. Chapter 6 is a brief recap of these developments, with a focus on their potential application and areas of future research. An appendix includes relevant implementation and calibration details that escaped the brevity of a succinct paper.

1.2 Problem Background

The world has become increasingly reliant on global navigation satellite systems (GNSSs) for positioning, navigation, and timing (PNT) applications. Many critical military and commercial systems have become solely dependent on the unparalleled characteristics of the Global Positioning System (GPS). Persistent world-wide availability, passive sensing, and sub-meter accuracy are difficult attributes to replace by any other navigation method. A fusion of alternative methods is necessary to maintain navigation capabilities without GPS. Airborne magnetic navigation uses spatial information from the Earth's magnetic anomaly field to constrain errors in an INS. Aerial magnetic navigation is passively sensed, globally available, impervious to jamming or spoofing, and accurate to tens of meters. However, magnetic anomaly maps become increasingly under-sampled, inaccurate, or just unavailable at lower altitudes, preventing applications in small unmanned aerial systems (sUAS) [4].

1.3 Research Objectives

This research extended the work of Canciani and Raquet [5], where extensive research into airborne magnetic navigation identified a large dependency on the accuracy and availability of prior-surveyed crustal magnetic anomaly maps. This research

first identified how SLAM had been used in magnetic navigation using man-made magnetic anomalies for robots and pedestrians without a map, and set the following research objectives:

- Apply SLAM techniques to remove aerial magnetic navigation's dependency on prior crustal magnetic anomaly maps.

- Design, calibrate, and deploy a UAV capable of collecting navigation-quality measurements of Earth's magnetic anomaly field.

- Determine the feasibility of magnetic navigation on a UAV.

1.4 Limitations and Assumptions

This research prioritized the demonstration of combining aerial magnetic navigation and SLAM as a proof-of-concept. As a result, simplistic methods were chosen without stressing computational efficiency.

Assumptions of airborne magnetic SLAM.

1. There is a measurable and spatially varying magnetic field.

2. A barometric altitude measurement is available.

3. A source of dead-reckoning is available.

4. A vehicle trajectory exists which intersects or overlaps itself providing loop closures.

5. Revisiting a the same point in space yields the same magnetic intensity measurement.

Magnetic navigation applies to a well-calibrated vehicle which traverses an area with a measurable and spatially varying magnetic field. Loop closures are a powerful

3

constraint in SLAM, which occur when current measurements are correlated to previously observed points in a vehicle's path. As a result, magnetic SLAM is specific to a calibrated vehicle which measures a spatially variant magnetic field while traversing a path over previously visited areas.

The typical uses of sUASs and autonomous underwater vehicles (AUVs) often result in trajectories that are likely to revisit over time. This makes magnetic SLAM a niche but relevant area of research with the most obvious application being sUASs or AUVs loitering near the Earth's surface where the spatial variance of the crustal magnetic anomaly field yields the most navigation potential, but navigation quality magnetic anomaly maps are especially unavailable.

1.5 Primary Contributions

This research produced Three primary contributions.

1. 1 Aerial magnetic navigation was demonstrated without a prior magnetic map on a full-sized aircraft.

2. 2 A UAV capable of producing compensated magnetic intensity measurements during flight was configured and flown.

3. 3 UAV magnetic navigation was demonstrated without a prior magnetic map with real magnetic intensity measurements and simulated UAV INSs solutions.

The methods demonstrated in this research provide full-sized and miniature aircraft a new globally-available and passively-sensed GPS-alternative navigation capability which does not require prior map data.

II. Background and Literature Review

This chapter provides a literature review and conceptual background for reference in the subsequent standalone papers. Section 2.1 reviews GNSS alternative navigation methods, map-based magnetic navigation, SLAM, magnetic vector field SLAM, and the open research area of aerial SLAM using the Earth's magnetic anomaly scalar field. Section 2.2 introduces Earth's magnetic intensity anomaly field, aircraft magnetic calibration, FastSLAM, Rao-Blackwellized particle filters, a probabilistic motion error model for an INS, and sparse data interpolation.

2.1   Literature Review of GPS Denied Navigation

This section identifies key literary works in GPS-denied navigation, magnetic navigation, and simultaneous localization and mapping (SLAM).

Key civilian and military infrastructure systems have become increasingly reliant on GPS for positioning and timing information and are therefore vulnerable to GPS unavailability [6, 7]. Occurrences of GPS jamming and spoofing have shown that critical systems require backups for when GPS is unavailable [8]. Modern navigation typically uses GPS positioning information to correct for drifting inertial measurement errors through Kalman filtering, resulting in systems which combine long-term and short-term navigation to improve navigation [9]. The global availability, passive sensing, and accurate positioning characteristics of GPS are difficult to replace by any one system. When GPS position updates are made unavailable, other sensors are required to supplement an inertial system to bound the drifting errors in accelerometers and gyroscopes. For example, some current alternative methods include: machine vision, terrain following, star tracking, and exploiting signals of opportunity. Each GPS alternative has it's own benefits and downsides, but the most valuable characteristics

of GPS to replace are its persistent global availability, position accuracy, independence of prior data, and passive use. We discuss the weaknesses of each approach in the following subsections.

2.1.1 Machine Vision.

Machine vision is a technique which correlates features in calibrated imagery with known locations in the environment. The relative orientation of the platform can be determined using stereo cameras or with a single camera observing a known feature from different angles. Camera-based navigation relies on the recognition of stable visual features which may vary depending on seasons, times of day, weather, or local topography, and are especially unavailable over featureless landscapes like water, snow, desert, or forests. [10, 11, 12].

2.1.2 Terrain Following.

Terrain following involves the use of range and bearing sensors to match measurements of the environment to a map. Active sensing methods used in terrain navigation such as laser range-finders, radar, or sonar [13, 14, 15] are often undesirable in discrete operations since they require emitting detectable energy [16]. This method is limited by the presence of distinguishable terrain, which can be a problem when considering that over two-thirds of the planet is covered with water.

2.1.3 Star Tracking.

Stars triangulation has been a means of global navigation for centuries. Modern celestial or satellite tracking using optical equipment requires an unobstructed line of sight and precise trajectory knowledge of the satellite or celestial object, as well as precise and expensive equipment. Cloud cover is more detrimental in aircraft

than for ships because intermittent position fixes from sporadic star spotting will still aid a slow-moving ship with an INS over a long journey [17]. Although flying above the clouds can remove cloud obstruction problems, this is not always feasible for low-altitude aircraft or surveillance platforms requiring a clear line-of-sight to the ground.

2.1.4 Signals of Opportunity.

Using signals of opportunity for trilateration has been shown as a viable method for positioning but requires prior knowledge of available and cooperative signals in the desired areas of operations [18]. An obviously problematic area would be over the oceans, which cover the majority of the Earth and where signal availability is an issue.

2.1.5 Map-based Magnetic Navigation.

Magnetic fields have been exploited for navigation since the invention of the compass. Goldenberg's Geomagnetic Navigation Beyond the Magnetic Compass [19] provided an in-depth discussion regarding the concept of referencing the geomagnetic field for navigation. He concluded that the geomagnetic field is a viable, globally-available navigation signal for positioning. He also concluded that magnetic sensing technologies are mature enough for geomagnetic positioning by the Earth's magnetic field. Pasku [20] surveyed more recent applications of magnetic navigation to include passive and active magnetic sources. Navigation by matching magnetic measurements to a map of the magnetic anomaly field is an advantageous GPS-denied method that boasts global signal availability, resistance to jamming, passive sensing, technological maturity, and effectiveness in INS aiding in the air [21], space [22], on land [23], and underwater [24]. The largest weakness of map-based magnetic navigation is the de-

pendence on the availability and accuracy of previously-surveyed geomagnetic maps. Unlike the magnetic signal, maps may not be globally available at high-enough quality for precise localization [25]. Aerial and underwater magnetic navigation use the magnetic anomaly field which is most spatially variant near the ground. Indoor magnetic navigation focuses instead on structural man-made magnetic disturbances in the Earth's magnetic field. We discuss various applications of *map-based* magnetic navigation in the following subsections.

2.1.5.1   Land-Based Magnetic Navigation.

Magnetic map matching with an INS can reduce navigation errors for GPS-denied ground vehicle navigation. Shockley demonstrated that using magnetic field variation in ground vehicles achieves adequate performance for road level navigation [26]. This method leveraged local magnetic field perturbations caused from ferrous materials in urban infrastructure as well as the crustal anomaly field. Kauffman and Raquet demonstrated that combining the global positioning accuracy of magnetic navigation with the short term precision of an INS improves navigation quality [23].

2.1.5.2   Aerial Magnetic Navigation.

Aerial magnetic navigation matches measurements of the Earth's magnetic anomaly field to a prior-surveyed magnetic anomaly map. Canciani and Raquet have thoroughly covered aerial magnetic navigation in the literature [4, 21, 27]. They demonstrated the viability of using the Earth's magnetic anomaly field as a time-invariant GPS-alternative system by achieving aerial navigation using a three-year old geomagnetic anomaly map, scalar magnetic intensity measurements, an INS, and barometer-sourced altitude measurements to achieve distance root mean squared (DRMS) errors of 13 meters over the span of a one hour flight. Liu et al. also demonstrated that

scalar magnetic intensity measurements can be used to aide an INS using contour constraints to a magnetic anomaly map and coarse-fine searching methods [28]. Yang et al. simulated that incorporating magnetic anomaly measurements into a cooperative localization framework extends the method to improving the navigation accuracy in UAVs [29].

2.1.5.3   Underwater Magnetic Navigation.

The concept of utilizing magnetic intensity maps like a terrain map underwater has been around for a long time [30, 24]. More recently, Quintas et al. demonstrated underwater magnetic navigation to position an AUV with less than 5 meters error [31]. Interestingly, magnetic navigation outperformed terrain navigation due to the lack of local topological variation; showcasing the ability of magnetic navigation to supplement existing navigation methods underwater. They also determined the improvement of magnetic navigation when simulated closer to the sea-floor where the spatial variation of the magnetic field increases. Lager, Topp, and Malec simulated a mean error of below 13 meters by fusing depth and magnetic measurements to poor quality maps to estimate drifting INS errors using a particle filter [32]. Zhou, Zhang, and Guo also show that an integration of an inertial system and magnetic map matching corrects for drifting INS errors [33].

2.1.5.4   Orbital Magnetic Navigation.

Satellites can use vector magnetometers and a model of Earth's core field to determine position and orientation through Kalman filtering approaches [34, 22, 35, 36, 37]. Earth's crustal anomaly field attenuates rapidly with increasing altitude and is negligible for satellites in orbital navigation [38].

9

2.1.5.5 Indoor Magnetic Navigation.

Indoor ambient magnetic anomaly fields have been used in conjunction with micro electro-mechanical systems (MEMS) vector magnetometers for pedestrian and robot localization using prior magnetic maps [39, 40, 41, 42, 43, 44]. Brzozowski et al. introduce a concept of a low-cost vector magnetometer array on a small UAV to survey a magnetic map for future indoor localization of cooperative UAVs. They attempted to map the interior of a building at three different elevations, placing permanent neodymium magnets along corridors as additional magnetic disturbance signal, while focusing on the development of the measuring platform without producing any attempt at navigation.

2.1.6 Simultaneous Localization and Mapping.

Mapping an environment involves applying sensor data to a known vehicle position. Vehicle localization compares current observations of the environment to information from a map. SLAM solves the mapping and localization problems concurrently using probabilistic techniques. SLAM can be used for making maps and navigating in unknown or changing environments. Recognizing a previously observed part of the environment is called a loop closure and corrects the entire trajectory history. This reduces estimation errors in both the vehicle trajectory estimate and environment map model. SLAM has been commonly implemented using Kalman filters, advancing with particle filters, and most recently through the application of graph-based methods [45, 46]. While the study of SLAM is daunting in it's range of application, a comprehensive introduction into the subject is provided by [47]. Some common SLAM applications are discussed in the following subsections.

2.1.6.1 Machine Vision SLAM.

SLAM is commonly used in the robotics community where machine vision is heavily leveraged. Stereo and monocular vision have been successfully used to navigate in a variety of environments with stable features. Correlating the large amount of spatial information in calibrated images with vehicle positions provides an information-rich front end to many implementations of SLAM filters [48]. Increasing interest in virtual reality and the popularity in airborne camera platforms have naturally transitioned SLAM from being used in ground robotics to hand-held devices and airborne vehicles [11, 49, 50]. The drawback of using camera-based SLAM is the ability to detect and identify features requires good visibility and a stable, feature-rich environment. This technique would fall short for aircraft looking at featureless landscapes like desert, grass, or water.

2.1.6.2 Laser/Sonar SLAM.

Laser and sonar range finders have been another primary focus in SLAM. Bearing and range sensors leverage scan matching algorithms like iterative closest points to incorporate measurements into the odometry proposal and identify revisiting map features to close loops [51, 52, 50]. Pose-graph methods are considered the most advanced to date [53]. A relevant example for this thesis is in underwater bathymetric sensing which has far less information available than a scanning lidar sensor. Chaves et al. discusses the concepts of pose-graph SLAM for underwater navigation. Bichucher et al. apply factor-graph slam with a sparse point cloud comprised of Doppler velocity log (DVL) measurements which sense the local water column depth [54]. This sparse sensing paradigm is more analogous to SLAM using a scalar field, thereby demonstrating the potential in factor-graph approaches with sparse measurements and ambiguous data association. An important contribution from [54] is the

method of associating sub-maps based on the heuristics that sub-maps *should* align using dynamic covariance scaling to handle erroneous data association. Their experimental implementation of the filter on an actual AUV constrained the dead-reckoning solution with a navigation accuracy of less than 5 meters over a 1 hour collection. The major drawback to using these sensors is that they are actively emitting, which may not be desired in all cases, and require observable features which may be unavailable.

2.1.6.3   Vector Field MagSLAM.

Vector magnetometers provide a measurement of the magnetic gradient in three directions. These three magnetic measurements have been used in SLAM with various robotics and pedestrian dead-reckoning systems. SLAM using a magnetic instrument to aide a dead-reckoning estimator has been referred to in literature as MagSLAM [55] which will be used for the duration of this paper. The following subsections present the successful use of magnetic navigation using vector magnetometers without prior magnetic field maps.

Ground Vector MagSLAM.   Ground-based MagSLAM utilizes structural ferromagnetic anomaly fields common in industrial settings [46, 40]. Commercial MEMS grade vector magnetometers have been used in magnetic localization and SLAM for small robots and pedestrians with a variety of SLAM frameworks for efficiency [56].

Vallivaara, Haverinen, and Kemppainen implemented indoor magnetic vector field SLAM with a roomba-style robot using a Rao-Blackwellized particle filter (RBPF) and Gaussian process regression (GPR) to constrain odometry errors with a positioning accuracy of less than one meter [57, 58]. Their GPR model treated each component of the magnetic vector measurement independently. They defined a path revisit using a euclidean distance threshold. Their expected measurement function

used in the residual weighting function of the RBPF modeled a particle's local magnetic map as a Gaussian process which was used to interpolate expected magnetic measurements. This filter structure benefited from it's simplicity and presented a valid framework for demonstrating the SLAM potential of the indoor magnetic field.

Kok and Solin corrected accumulating drift errors from a visual-inertial smartphone pedestrian dead-reckoning solution using a RBPF with hierarchical hexagonal magnetic maps [59]. Each particle's map was defined as an underlying Gaussian process prior by leveraging Maxwell's equations and the relationship between the components of magnetic vector measurements and the scalar potential field. This essentially defined a set of rules which better modeled the underlying physics of a scalar potential field and increased the filter performance. Although their method of pedestrian travel leveraged guaranteed path overlaps from walking path constraints, they obtained accurate position and orientation estimates of a pedestrian using vector magnetometer measurements from a smart-phone without a prior surveyed magnetic map. The framework for their filter made magnetic field SLAM scalable in both computational complexity and map storage; a major obstacle in map-based SLAM. Of key interest was their use of pre-computed eigen-functions of the negative Laplace operator in the hexagonal domain; numerically solving the eigendecomposition of the Laplace operator in the two-dimensional hexagonal domain before extending into the three-dimensional domain. Their implementation of the RBPF partitioned the phone's position and orientation as nonlinear states, with 256 nonlinear states per map tile to represent the combination of pre-computed eigenbasis expansions of the Gaussian process magnetic map. This method proved to be complex in it's map model but attractive in it's scalability and robustness with low cost sensors.

Jung, Oh, and Myung implemented a more recent pose-graph SLAM approach with a wheeled robot by associating sequences of magnetic vector field measurements

in overlapping paths to achieve sub-meter level accuracy [60]. Unfortunately, this method required overlapping path segments.

Chow uses a Gaussian Process SLAM framework to achieve a drift-free navigation solution with millimeter-level accuracy by exploiting the anomaly field created by indoor magnetic disturbances. This approach was a maximum a posteriori estimation problem which naturally performs loop closures, feature-to-feature distance minimization, global trajectory optimization, and magnetic field map estimation. This method boasted a navigation solution which is never worse than the inertially proposed navigation solution [61].

Aerial MagSLAM. The research field of magnetic navigation is quickly growing [23]. However, aerial vector MagSLAM has not been widely researched or demonstrated. One of the major obstacles with vector-field UAV MagSLAM lies in the hypersensitivity of vector magnetometer readings with regard to vehicle attitude errors. Inertial measurement units (IMUs)s with accumulating attitude errors create variations in reference frame transformations that drown out the useful magnetic vector components of the Earth's magnetic anomaly field. Future improvements in vector magnetometers and MEMS INSs may make this more feasible.

Autonomous Underwater Vehicle Magnetic SLAM. SLAM is especially useful under water since GNSS is typically unavailable under the surface and prior oceanic geomagnetic field maps may be unavailable [13, 62]. The use of magnetic sensors to aide an INS is attractive because low-light conditions deter the use of imaging sensors and active sensors often announce the presence of the vehicle or disrupt wildlife [63]. There has not been a successful implementation of underwater MagSLAM on a AUV using the Earth's magnetic crustal anomaly field. Liu et al. [64] come closest by simulating the potential application of using the geomagnetic

14

field using geomagnetic cues between a starting and target position. The large area AUV MagSLAM perspective is analogous to the UAV MagSLAM paradigm and the advances in methodology in the literature are applicable.

2.1.6.4 Scalar Field SLAM.

SLAM has traditionally been applied with cameras or scanning lasers which use the dense set of data-points in a single measurement to accurately model changes in the environment at a distance. A magnetic intensity measurement is an observation of a scalar field at a single point in space. The sparse amount of information from a single measurement of a scalar field is insufficient for localization because of its spatial ambiguity [60]. A sequence of scalar measurements and a moving platform's dead-reckoning estimate is required over time to provide unique position information. This combines short-term vehicle dynamic constraints and loop closures from revisiting scalar observations to provide global constraints.

Robertson et al. [55] implemented a scalable large-area indoor pedestrian SLAM with a foot-based inertial measurement unit and scalar magnetic intensity measurements. They used hierarchical magnetic intensity grid maps, particle filtering, and spatial measurement binning methods to constrain the drift in a pedestrian dead-reckoning system. They achieved pose-estimation accuracy on the decimeter level by addressing common filtering implementation challenges with various tuning methods. This is the first known instance where a scalar magnetic field has been used in SLAM with a RBPF. The significance of this success cannot be understated. The closest similar instance is [65], where the signal strengths of WiFi signals are used as continuous scalar maps to perform pose-graph SLAM.

One of the greatest challenges in using a scalar field for SLAM is the extremely little information regarding a vehicle's position or orientation in a single scalar magnetic

measurement. A valid dynamic motion model, high-quality dead-reckoning solution, and substantial scalar field variation is required to correct drifting errors. Scalar field navigation methods can be extended to gravitational fields, ambient lighting, wireless signal strength, and other continuous scalar fields. To our knowledge, no instance of scalar-field SLAM has been successfully simulated nor demonstrated with real data in the air or underwater.

2.2 Background

The purpose of this section is to introduce the concepts of Earth's magnetic field components, calibrating magnetic survey aircraft, SLAM, and nonlinear state estimation. The intent is to provide the reader with the basic tools required to understand the methodology and results discussed in the rest of this thesis.

2.2.1 Earth's Magnetic Field.

This section will briefly introduce some fundamental characteristics of the Earth's magnetic field and more importantly, the anomalies used as a navigation signal as explained by Reeves and Hinze et al. [66, 38].

Earth's magnetic field is a scalar potential field. It may provide some intuition to remember that Earth's gravitational field is also a potential field. There exists a singular value of magnetic potential at each point in three dimensional space. A scalar potential field is curl and divergence free, without any discontinuities or instantaneous drop-offs. The spatial gradient of the potential field is a vector field, where each Cartesian component's magnitude is the gradient of the potential field in that direction. The familiar magnetic compass is used to indicate the horizontal magnetic vector components, but there exists a vertical component which generally points up at the South pole, down at the North pole, and approximately level at the equator.

Magnetic intensity measurements measure the magnitude of the vector field. In short: A scalar magnetic intensity is the vector norm of the gradient of the scalar potential field.

$$B_{intensity} = ||\nabla B_{potential}|| \tag{1}$$

The total terrestrial magnetic field consists of various contributing fields within and outside the Earth. The geomagnetic field within the Earth is often considered to have three parts: core, mantle, and crust. Earth's liquid iron core contains convection processes which generate a bipolar field, roughly along the Earth's rotation axis. The outer core of the Earth generates electromagnetic currents which account for around 98% of the geomagnetic field. The mantle has a negligible interaction with Earth's magnetic field and is therefore often ignored in magnetic models. The crustal field comes from large distributions of magnetically susceptible mineral formations perturbing the Earth's core field. The resulting deviation from the core-field model is called the crustal anomaly field. External magnetic interactions between the core field and solar plasma from space contribute a highly time-varying component to the rest of the terrestrial magnetic field. The summation of the external fields can be grouped together as temporal space-weather effects.

2.2.1.1   World Magnetic Model.

The World Magnetic Model (WMM) is one current community-accepted model of the Earth's core magnetic field. The WMM models Earth's magnetic field as the gradient of Earth's scalar potential field as a function of time. The WMM can be used to calculate an expected Earth magnetic field vector based on latitude, longitude, and date. The WMM model also accounts for time varying secular variations in Earth's magnetic field. The WMM is periodically remodeled based on new observations from ground based observatories and satellites.
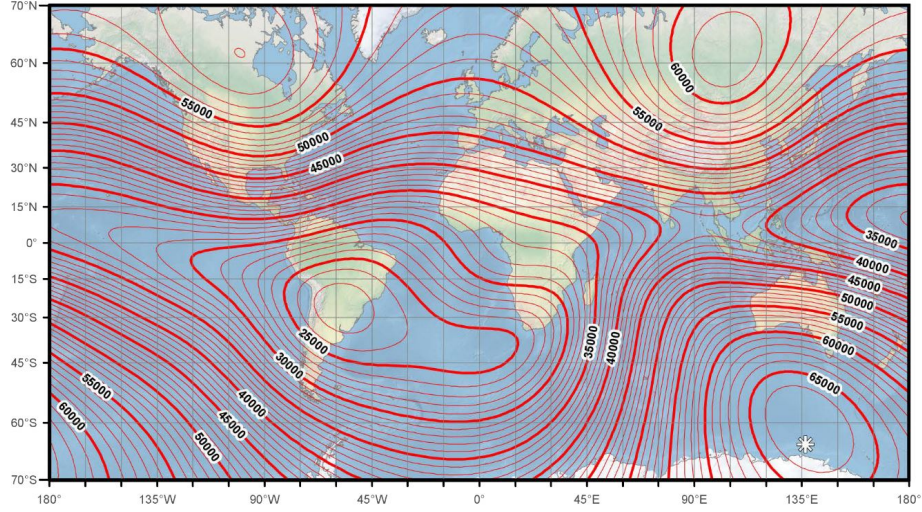
Figure 1. The 2015 World Magnetic Model Intensity [1]

2.2.1.2   Temporal Variations.

Earth's magnetic field changes from the summation of diurnal variations, micropulsations, magnetic storms, and secular variations. Diurnal variations are periodic affects from the solar wind's interaction between the day-night cycle and the magnetosphere of Earth [66]. Micro-pulsations are small, higher frequency variation from atmospheric interactions [67]. Magnetic solar storms vary over the course of days but can be of great magnitude. Secular variation reflects internal changes in the Earth's core field which vary slowly over the span of many years. A ground station magnetometer can measure these temporal variations and remove them from a survey flight dataset. An example of observed temporal variations from a stationary ground station is shown in figure 2.
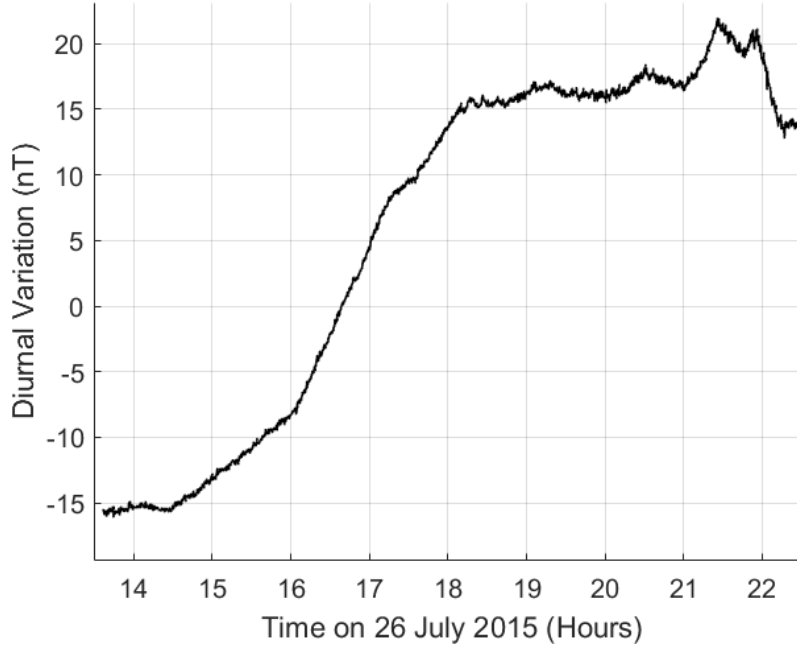
Figure 2. Magnetic variations as measured at a survey station near Louisa Virginia (WMM and mean removed).

2.2.1.3 Earth's Magnetic Anomaly Field.

The observable Earth field (B_{Earth}) is considered as the vector sum of Earth's core field, modeled by the WMM, and a crustal anomalous component $(B_{Anomaly})$. The WMM vector field is oriented according to the Earth core field model, whereas the anomalous vector component points in any direction. As long as Earth's core field vector component is around two orders of magnitude higher than the anomalous component, it is accepted in literature to approximate the $||B_{anomaly}||$ as $||B_{observed}|| - ||B_{WMM}||$. Total field magnetic anomaly maps record the projection of the anomaly vector onto the Earth's main field. The anomalous component is the summation of induced and remnant magnetic fields caused by ferrous materials in the Earth's crust [66]. Figure 3 illustrates the magnitude assumption used by models of the Earth's magnetic anomaly intensity scalar field.

19
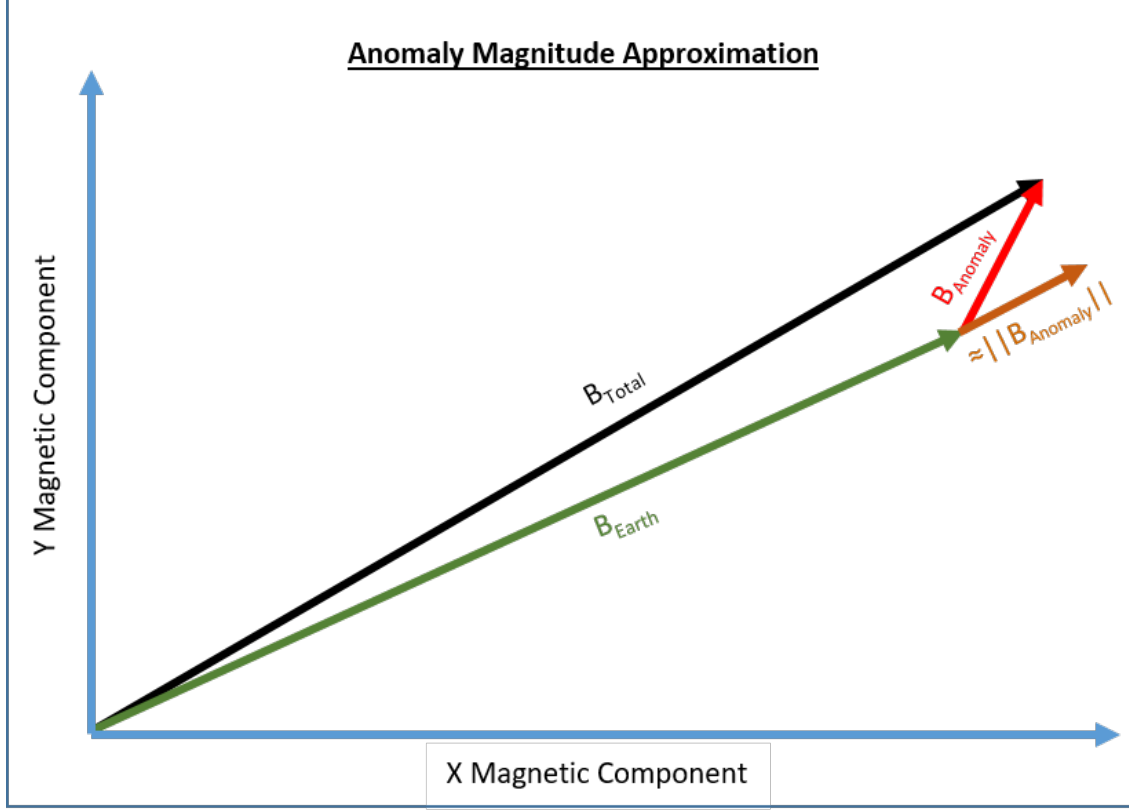
Figure 3. The magnitude of the anomaly field is approximated as the magnitude of the anomaly vector projected onto the total field $||B_{Anomaly}|| = ||B_{Total}|| - ||B_{WMM}||$ when $||B_{Earth}|| >> ||B_{Anomaly}||$.

2.2.2 Aeromagnetic Calibration.

Magnetic intensity scalar measurements need to be compensated for a survey vehicles magnetic disturbance field. The aircraft's magnetic field is a disturbance, denoted here as B_{dist}. The vehicle disturbance field is a major consideration of magnetic navigation and can be determined through vehicle calibration maneuvers. Similar methods are used for the calibration of underwater surveying vehicles [68]. This section provides a background on how a three-axis magnetometer and vehicle disturbance coefficient model can predict an aircraft's disturbance field.

2.2.2.1 Aircraft Calibration Flight.

A typical aircraft calibration flight is conducted at high altitude in an area of low magnetic gradient to minimize variation in the true magnetic field. Two square patterns are flown in opposite directions while exercising variations in roll, pitch, and yaw maneuvers along the straight legs of each square. It is assumed that any variation in the magnetic measurement will be caused by aircraft maneuvers and can therefore be identified as the aircraft s field. Solving for 18 coefficients using a calibration dataset provides an aircraft-specific characterization model as long as the aircraft configuration does not change. Flying a cloverleaf pattern and measuring the difference in calibrated magnetic measurements at the center provides a figure of merit for a survey flight which is often less than one nano-Tesla in professional surveys.

2.2.2.2 Tolles And Lawson Model.

Flux-gate vector magnetometer readings can capture the correlation between aircraft orientation (with regard to the Earth's magnetic field), and the aircraft's disturbance in the scalar intensity measurement [66]. A vector magnetometer returns three magnetic intensities, B_x, B_y, and B_z, in the directions of the sensor's Cartesian reference frame. The vector sum of all three components gives a measurement of the total field $B = \sqrt{B_x^2 + B_y^2 + B_z^2}$. The normalized direction cosines (2) of the main vector field and their derivatives in conjunction with an 18 coefficient characterization vector (3) can model an aircraft's contributing field as first introduced by Tolles and Lawson in 1950 [69].

$$\cos(x) = \frac{B_x}{B}, \ \cos(y) = \frac{B_y}{B}, \ \cos(z) = \frac{B_z}{B} \tag{2}$$

$$\eta = \begin{bmatrix} e_1 \\ \vdots \\ e_{18} \end{bmatrix} \tag{3}$$

The aircraft disturbance field is modeled as the summation of three primary sources: permanent field, induced field, and eddy currents.

$$B_{dist} = B_{perm} + B_{ind} + B_{eddy} \tag{4}$$

1. Permanent magnetization: The inherent static magnetic field of the survey aircraft components.

$$B_{perm} = e_1 \cos x + e_2 \cos y + e_3 \cos z \tag{5}$$

2. Induced magnetization: The magnetic field induced on the aircraft components by the Earth's magnetic field. The relative orientation of the aircraft to the geomagnetic field will determine the magnitude and direction of the induced magnetization. This component will be dependent on the position and orientation of the aircraft.

$$B_{ind} = B \times [e_4 + e_5 \cos x \cos y + e_6 \cos x \cos z + e_7 \cos y^2 + e_8 \cos y \cos z + e_9 \cos x^2] \tag{6}$$

3. Eddy Currents: The motion of the aircraft structure through the Earth's field

will induce eddy currents according to Biot-Savart's Law.

$$B_{eddy} = B \times [e_{10} \cos x \dot{\cos} x + e_{11} \cos x \dot{\cos} y + e_{12} \cos x \dot{\cos} z ...$$
$$+ e_{13} \cos y \dot{\cos} x + e_{14} \cos y \dot{\cos} y + e_{15} \cos y \dot{\cos} z ... \tag{7}$$
$$+ e_{16} \cos z \dot{\cos} x + e_{17} \cos z \dot{\cos} y + e_{18} \cos z \dot{\cos} z]$$

The disturbance component of a time-series dataset can be written as the $t \times 18$ matrix of direction cosine components $\mathbf{A}$ times a 18×1 coefficient vector η.

$$B_{dist} \approx \mathbf{A}\eta \tag{8}$$

The coefficients are the solution to minimizing the difference between the model and the aircraft disturbance measurements:

$$\underset{\eta}{argmin}(\mathbf{A}\eta - z) \tag{9}$$

In practice, isolating aircraft disturbance correlations involves applying band-pass filters which block out contributing noise sources outside of the bandwidth of an aircraft's manuevers. These filters are specific to an aircraft's rates of roll, pitch, and yaw. Equation 9 becomes:

$$\underset{\eta}{argmin}(X\eta - Y) \tag{10}$$

where X and Y are the finite impulse response (FIR) band-passed or high-passed $\mathbf{A}$ matrix and measurements z, respectively, during the calibration flight. Note how the FIR filter applied to both A and z is a linear transformation which maintains the correlation between the coefficients and aircraft effects in the bandwidth of the filter.

2.2.2.3 Accounting for Vector Magnetometer Errors.

Vector magnetometer measurement errors have a direct impact on the quality of an aeromagnetic calibration [70]. The imbalance in precision is accounted for by incorporating magnetometer error terms in the aircraft calibration process as discussed and demonstrated through simulation by [70, 71].

2.2.3 FastSLAM.

SLAM is a method by which a mobile vehicle can build a map of an environment and use this map to determine it's location concurrently [45]. This method allows a vehicle to estimate its trajectory and environment online without the need for a map. While the concept of SLAM has been around since 1986 [72], FastSLAM was first introduced by Montemerlo in 2003 as a factored solution to SLAM with unknown data association [73]. Until the early 2000's, online SLAM for robotic navigation was mainly implemented using extended Kalman filters. The two major downsides to extended Kalman filter (EKF) SLAM were quadratically scaling memory and time complexity, as well as sensitivity to incorrect data association. The key contribution in FastSLAM is that the full SLAM posterior can be factored into a product of recursive estimators: vehicle trajectory, and landmark positions conditioned on the same trajectory estimate. FastSLAM estimates the vehicle path using a particle filter, with the remaining N conditional landmark posteriors using EKFs. The following is an explanation of the FastSLAM algorithm as presented by Montemerlo [73].

2.2.3.1 Posterior Factorization of Map and Vehicle Trajectory.

A key, yet subtle, difference between traditional SLAM approaches and FastSLAM is that SLAM approaches are based on estimating the posterior over maps and vehicle position: $p(x_t, \theta | z_{1:t} u_{1:t}, n_{1:t})$, whereas FastSLAM is conditioned on the entire vehicle

path estimate: $p(x_{1:t}, \theta | z_{1:t} u_{1:t}, n_{1:t})$. Murphy [74] first presented the factorization of the full SLAM posterior into a product of N+1 recursive estimators: one estimator over robot paths, and N independent estimators over landmark positions, each conditioned on the path estimate as described in equation (11).

$$p(x_{1:t}, \theta_{1:n} | z_{1:t}, u_{1:t}, n_{1:t}) = \underbrace{p(x_{1:t} | z_{1:t}, u_{1:t}, n_{1:t})}_{\text{trajectory posterior}} \underbrace{\Pi_{n=1}^{N} p(\theta_n | x_{1:t}, z_{1:t}, u_{1:t}, n_{1:t})}_{\text{landmark estimators}} \qquad (11)$$

This factorization can be efficiently approximated with a particle filter where each sample path of the vehicle is a particle. Each particle has a bank of EKF landmark estimators; one EKF for each landmark. This method becomes a RBPF with a number of (N landmarks) times (M particles) Kalman filters. This method boasts two major advantages:

1. Logarithmic Complexity

   Organizing each particle as a binary tree of landmark estimators instead of an array removes redundant EKF landmark estimators since particle resampling leads to shared path history segments between particles.

2. Multi-Hypothesis Data Association

   With each particle representing a specific vehicle path, data associations can be made on a per-particle basis. Particles that choose correct data associations should naturally receive higher weights and be more likely to survive resampling. particles that choose incorrect associations will receive low weights over time.

2.2.3.2 FastSLAM Disadvantages.

FastSLAM is an implementation of a RBPF. Particle resampling consists removing low-probability particles while duplicating particles with high probability many times. This process keeps the target distribution most dense around the latest observations,

but gradually eliminates diversity in the trajectories represented by the particles. Consequently, all particles will eventually share a common trajectory. This can be thought of as the filter 'forgetting' correlation information smoothly over time. This creates an underestimated covariance, and can cause issues for closing loops. Both problems are the result of the relationship between convergence speed and loss of correlation information in FastSLAM.

2.2.4 Rao-Blackwellized Particle Filter.

Navigation algorithms commonly implement some form of stochastic state estimators called filters. These filters attempt to estimate a system's state based on a dynamics model and by applying measurement updates. The RBPF is a system state estimator which extends a basic particle filter by combining non-Gaussian and linearly Gaussian state variables. The RBPF is also known as a marginalized particle filter since the linear state variables are marginalized about the non-linear state variables. The non-linear states are represented as particles and the linear states are represented by Kalman filters. This technique allows for the feasible computation of high-dimensional state variables without encountering the dimensionality problem of particle filters. The following is a generalized form of the RBPF as shown and further derived by Schon, Gustaffson, and Nordlund [75].

2.2.4.1 General State-Space Model.

The problem of non-linear, non-Gaussian filtering recursively computes the posterior distribution of a state vector using observed measurements. The general form

is:

$$x_{t+1} = f(x_t, w_t), \tag{12a}$$

$$y_t = h(x_t, e_t) \tag{12b}$$

where x_t is the state variable at time t, w_t is the process noise, y_t is the measurement at time t, e_t is the measurement noise, $f(\cdot)$ is the system dynamics model, and $h(\cdot)$ is the measurement equation. The output of the function $f(\cdot)$ is the state variable at the next discrete time step x_{t+1}.

2.2.4.2 Posterior Distribution.

The posterior distribution $p(x_t|Y_t)$, where Y_t is the history of previous measurements $y_{i_{i=0}}^t$, is given by the measurement recursion and time recursion equations:

$$p(x_t|Y_t) = \frac{p(y_t|x_t)p(x_t|Y_{t-1})}{p(y_t|Y_{t-1})} \tag{13a}$$

$$p(y_t|Y_{t-1}) = \int p(y_t|x_t)p(x_t|Y_{t-1})dx_t \tag{13b}$$

$$p(x_{t+1}|Y_t) = \int p(x_{t+1}|x_t)p(x_t|Y_t)dx_t \tag{13c}$$

If these were Gaussian distribution models, then a Kalman filter would optimally model the system with the propagation of the state means and covariances. Non-linear and non-Gaussian models which are mathematically intractable require numerical approximations of the integrals in equation (13).

2.2.4.3 State Partitioning.

The state variable is partitioned as a combination of non-linear states x_t^n and conditionally linear states x_t^l:

$$x_t = \begin{bmatrix} x_t^n \\ x_t^l \end{bmatrix}.$$

(14)

The combined system can be expressed as the combination of the two parts. The general form of equation 12 becomes:

$$x_{t+1}^n = f_t^n(x_t^n) + A_t^n(x_t^n)x_t^l + G_t^n w_t^n,$$

(15a)

$$x_{t+1}^l = f_t^l(x_t^n) + A_t^l(x_t^n)x_t^l + G_t^l w_t^l,$$

(15b)

$$y_t = h_t(x_t^n) + C_t(x_t^n)x_t^l + e_t$$

(15c)

where the non-linear and linear states are propagated forward in time by some function of the non-linear states $f(\cdot)$ and some linear combination of the linear states conditioned on the non-linear states represented by $A_t^n(x_t^n)$ and $A_t^l(x_t^n)$. The measurement model is a function of both the non-linear states denoted by $h_t(x_t^n)$ and a linear combination of the conditionally linear states; defined by the matrix $C_t(x_t^n)$. The case where the system dynamics model is linear and the measurement model is a non-linear function dependent on only the non-linear states is a direct use of model 4 from [75]. This means that equation (15) can be rewritten as:

$$x_{t+1}^n = A_{n,t}^n x_t^n + A_{l,t}^n(x_t^n)x_t^l + w_t^n,$$

(16a)

$$x_{t+1}^l = A_{n,t}^l x_t^n + A_{l,t}^l(x_t^n)x_t^l + w_t^l,$$

(16b)

$$y_t = h_t(x_t^n) + e_t.$$

(16c)

The state noise is assumed to be white Gaussian noise defined as

$$w_t = \begin{bmatrix} w_t^n \\ w_t^l \end{bmatrix} \sim \mathcal{N}\left(0, Q_t\right), \quad Q_t = \begin{bmatrix} Q_t^n & Q_t^{nl} \\ (Q_t^{nl})^T & Q_t^l \end{bmatrix}. \tag{17}$$

The measurement noise e_t can be an arbitrary distribution but is assumed to be known.

2.2.4.4 Filter Algorithm.

The general sequence of the marginalized particle filter is:

Algorithm 1: Marginalized particle filter

---
1 Initialization

2 Particle filter measurement update

3 Kalman filter measurement update (if applicable)

4 Particle filter time update

5 Kalman filter time update

6 Reiterate from step 2

2.2.4.5 Initialization.

The initial condition of the linear states is assumed Gaussian

$$x_0^l \sim \mathcal{N}\left(\bar{x}_0^l, \bar{P}_0\right). \tag{18}$$

The initial condition of the nonlinear states x_0^n can be any distribution but is assumed to be known. The expected means and covariances of the linear state variables are

given by

$$
\hat{x}^l_{t|t} = \sum_{i=1}^{N} \tilde{q}^{(i)}_t x^l_{t|t} \approx E_{p(x^l_t|Y|t)}[x^l_t] \tag{19a}
$$

$$
\hat{P}_{t|t} = \sum_{i=1}^{N} \tilde{q}^{(i)}_t \left(P^{(i)}_{t|t} + \left(\hat{x}^{l,(i)}_{t|t} - \hat{x}^l_{t|t} \right) \left(\hat{x}^{l,(i)}_{t|t} - \hat{x}^l_{t|t} \right)^T \right) \tag{19b}
$$

$$
\approx E_{p(x^l_t|Y_t)} \left[\left((x^l_t)^2 - E_{p(x^l_t|Y_t)}[(x^l_t)^2] \right)^2 \right] \tag{19c}
$$

where $\tilde{q}^{(i)}_t$ are the normalized particle importance weights. When A^n_t, A^l_t, G^n_t, and G^l_t are independent of x^n_t, it implies:

$$
P^{(i)}_{t|t} = P_{t|t} \quad \forall i = 1, ..., N. \tag{20}
$$

This provides massive computational savings in that only one Riccati recursion is necessary in (19).

2.2.4.6 Particle Filter Measurement Update.

The particle filter uses a weighted set of particles to approximate $p(x_t|Y_t)$ from equation (13) with an inference function $g(\cdot)$ described as

$$
I(g(x_t)) = E_{p(x_t|Y_t)}[g(x_t)] = \int g(x_t) p(x_t|Y_t) dx_t. \tag{21}
$$

A common inference function is the Gaussian residual weighting function where the i-th particle's weight at time t , $q^{(i)}_t$ is determined by:

$$
q^{[i]}_t = q^{[i]}_{t-1} exp\left(- \frac{(z_t - \hat{z}^{[i]}_t)^2}{2R} \right) \tag{22}
$$

After particle weights are assigned, the set is normalized according to: $\tilde{\mathbf{q}}_t = \frac{\mathbf{q}}{\sum \mathbf{q}}$ as to create a valid probability mass function (PMF) such that the sum of the weights

equals 1. A standard selective resampling criteria from Liu [76] determines when to resample:

$$N_{eff} = \frac{1}{\sum_{i=1}^{N} (\tilde{q}^{(i)})^2}, \quad \text{Resample If } N_{eff} < \frac{N}{2} \tag{23}$$

Where N is the total number of particles. The first and second moment of the posterior distribution can be then approximated as

$$\hat{x}_{t|t}^n = \sum_{i=1}^{N} \tilde{q}_t^{(i)} x_{t|t}^n \approx E_{p(x_t^n|Y_t)}\left[x_t^n\right] \tag{24a}$$

$$\hat{P}_{t|t}^n = \sum_{i=1}^{N} \tilde{q}_t^{(i)} \left(\left(x_{t|t}^{n,(i)} - \hat{x}_{t|t}^n\right)\left(x_{t|t}^{n,(i)} - \hat{x}_{t|t}^n\right)^T \right) \tag{24b}$$

$$\approx E_{p(x_t^n|Y_t)}\left[\left((x_t^n)^2 - E_{p(x_t^n|Y_t)}\left[(x_t^n)^2\right]\right)^2 \right]. \tag{24c}$$

2.2.4.7 Kalman Filter State Measurement Update.

The Kalman filter states are conditional on the nonlinear states. These linear states are updated in three parts: a measurement update using information available in y_t, a measurement update using information available in the nonlinear state distribution $\hat{x}_{t+1|t}^n$, and a time update. In the general case, the conditional probability distributions for x_t^l and x_{t+1}^l are:

$$p(x_t^l|X_t^n, Y_t) = \mathcal{N}\left(\hat{x}_{t|t}^l, P_{t|t}\right) \tag{25a}$$

$$p(x_{t+1}^l|X_{t+1}^n, Y_t) = \mathcal{N}\left(\hat{x}_{t+1|t}^l, P_{t+1|t}\right) \tag{25b}$$

where information from the measurement y_t and $\hat{x}^n_{t+1|t}$ enters the Kalman states $p(x^l_t|X^n_t, Y_t)$ through a Kalman Filter measurement update:

$$\hat{x}^l_t = \hat{x}^l_t + K_t(y_t - h_t - C_t\hat{x}^l_{t|t-1}) \tag{26a}$$

$$P^l_{t|t} = P^l_{t|t-1} - K_t M_t K^T_t \tag{26b}$$

$$M_t = C_t P^l_{t|t-1} C^T_t + R_t \tag{26c}$$

$$K = P^l_{t|t-1} C^T_t M^{-1}_t. \tag{26d}$$

2.2.4.8 Particle Filter Time Update.

Each particle's nonlinear state experiences a time update according to the system's dynamics equations. In the case of a linearized dynamics model, the particle set is drawn by discretizing the linear dynamics equation in (16) and adding state noise according to the noise model Q^n_t:

$$x^n_{t+1|t} = \mathcal{N}\left(A^n_{n,t}x^n_t + A^n_{l,t}x^l_t,\ A^n_{l,t}P^l_t(A^n_{l,t})^T + Q^n_t\right) \tag{27}$$

2.2.4.9 Kalman Filter State Time Update.

The Kalman filter time update then propagates the linear states according to

$$\hat{x}^l_{t+1|t} = \bar{A}^l_t\hat{x}^l_{t|t} + G^l_t(Q^{nl}_t)^T(G^n_t Q^n_t)^{-1} + f^l_t + L_t(z_t - A^n_t\hat{x}^l_{t|t}) \tag{28a}$$

$$P_{t+1|t} = \bar{A}^l_t P_{t|t}(\bar{A}^l_t)^T + G^l_t \bar{Q}^l_t(G^l_t)^T - L_t N_t L^T_t \tag{28b}$$

$$N = A^n_t P_{t|t}(A^n_t)^T + G^n_t Q^n_t(G^n_t)^T \tag{28c}$$

$$L = \bar{A}^l_t P_{t|t}(A^n_t)^T N^{-1}_t \tag{28d}$$

where

$$z_t = x_{t+1}^n - f_t^n \tag{29a}$$

$$\bar{A}_t^l = A_t^l - G_t^l (Q_t^{nl})^T (G_t^n Q_t^n)^{-1} A_t^n \tag{29b}$$

$$\bar{Q}_t^l = Q_t^l - (Q^n l_t)^T (Q_t^n)^{-1} Q_t^{nl}. \tag{29c}$$

When G is the identity matrix I, and the cross covariance Q_t^{nl} between noise sources w_t^n and w_t^l is zero, $\bar{A}_t^l = A_t^l$ and $\bar{Q}_t^l = Q_t^l$. Additionally, if there is no linearized relationship between the measurement and the linear states, C_t is zero. This means that the only way for information from y_t to enter the linear states is implicitly through the time update. A separate Kalman filter measurement update can still occur with the availability of a strictly linear measurement.

2.2.5   Pinson INS Error Dynamics Model.

An INS can be a source of dead-reckoning by providing short-term vehicle dynamics constraints. INSs are used to measure the relative motion between a vehicle's local body frame and an inertial reference frame. The dynamic motion of the vehicle can be determined by integrating acceleration and angular rate disturbances, correcting for Coriolis and gravitational effects, and then determining position and velocity estimates resolved in the local navigation frame. Twice-integrated accelerometer and gyroscope biases and noise inevitably lead to a navigation estimate that drifts over time. State space estimation models can use an INS solution to estimate the whole state, or the accumulating errors in the INS instead. This section introduces a fundamental nine state INS error model from [9].

2.2.5.1 Pinson Nine-State Error Model.

The state variable used in the generic nine-state Pinson error model is:

$$\mathbf{x} = \begin{bmatrix} \delta\mathbf{p} \\ \delta\mathbf{v} \\ \delta\epsilon \end{bmatrix} \tag{30}$$

where $\delta\mathbf{p}$ $\delta\mathbf{v}$, and $\delta\epsilon$ are three dimensional position, velocity, and tilt error vectors respectively. The Pinson error model states propagate according to the linear dynamics equation:

$$\dot{\mathbf{x}} = F\mathbf{x} + w, \ E[w^2] = Q, \tag{31}$$

where F is the system dynamics matrix, and w is the process noise. The model adds white Gaussian noise into the velocity and tilt states which becomes integrated as random walk errors. The white noise strength is characterized by the matrix:

$$Q = diag\left(\begin{bmatrix} \mathbf{0} & \sigma^2_{\mathbf{VRW}} & \sigma^2_{\mathbf{ARW}} \end{bmatrix} \right)_{9x9} \tag{32}$$

The F matrix can be broken up into nine sub-matrices relating position, velocity, and tilt errors to each other:

$$\begin{bmatrix} \dot{\delta\mathbf{p}} \\ \dot{\delta\mathbf{v}} \\ \dot{\delta\epsilon} \end{bmatrix} = \begin{bmatrix} F_{\mathbf{pp}} & F_{\mathbf{pv}} & F_{\mathbf{p\epsilon}} \\ F_{\mathbf{vp}} & F_{\mathbf{vv}} & F_{\mathbf{v\epsilon}} \\ F_{\epsilon\mathbf{p}} & F_{\epsilon\mathbf{v}} & F_{\epsilon\epsilon} \end{bmatrix} \begin{bmatrix} \delta\mathbf{p} \\ \delta\mathbf{v} \\ \delta\epsilon \end{bmatrix} \tag{33}$$

The following notation described in table 1 will remain consistent throughout the remainder of this section.

Titterton and Weston express North and East position errors in radians for latitude and longitude, and vertical position error as positive upward altitude error [9],

Table 1. Pinson Nomenclature

Variable	Description	Value
L	Latitude	
v_n	North velocity	
v_e	East velocity	
v_d	Down velocity	
R_e	Earth radius	6353000 m
f_n	Measured specific force (North direction)	
f_e	Measured specific force (East direction)	
f_d	Measured specific force (Down direction)	
Ω	Earth rotation rate	$7.2921151467 \times 10^{-5}\ rad/s$
g	vertical component of gravity	

resulting in the following nine F sub-matrices:

$$F_{\mathbf{pp}} = \begin{bmatrix} 0 & 0 & \dfrac{-v_n}{R_e^2} \\[2ex] \dfrac{v_e \tan L}{R_e \cos L} & 0 & \dfrac{v_e}{R_e^2 \cos L} \\[2ex] 0 & 0 & 0 \end{bmatrix} \tag{34}$$

$$F_{\mathbf{pv}} = \begin{bmatrix} \dfrac{1}{R_e} & 0 & 0 \\[2ex] 0 & \dfrac{1}{R_e \cos L} & 0 \\[2ex] 0 & 0 & -1 \end{bmatrix} \tag{35}$$

$$F_{\mathbf{p\epsilon}} = \mathbf{0}_{3x3} \tag{36}$$

$$F_{\mathbf{vp}} = \begin{bmatrix} v_e(2\Omega \cos L + \dfrac{v_e}{R_e \cos^2 L}) & 0 & \dfrac{v_e^2 \tan L - v_n v_d}{R_e^2} \\[2ex] 2\Omega(v_n \cos L - v_d \sin L) + \dfrac{v_n v_e}{R_e \cos^2 L} & 0 & \dfrac{-v_e(v_n \tan L + v_d)}{R_e^2} \\[2ex] 2\Omega v_e \sin L & 0 & \dfrac{v_n^2 + v_e^2}{R_e^2} \end{bmatrix} \tag{37}$$

$$F_{\mathbf{v\epsilon}} = \begin{bmatrix} \dfrac{v_d}{R_e} & -2(\Omega \sin L + \dfrac{v_e \tan L}{R_e}) & \dfrac{v_n}{R_e} \\[2ex] 2\Omega \sin L + \dfrac{v_e \tan L}{R_e} & \dfrac{v_n \tan L + v_d}{R_e} & 2\Omega \cos L + \dfrac{v_e}{R_e} \\[2ex] \dfrac{-2v_n}{R_e} & -2(\Omega \cos L + \dfrac{v_e}{R_e}) & 0 \end{bmatrix} \tag{38}$$

$$F_{\mathbf{v}\epsilon} = \begin{bmatrix} 0 & -f_d & f_e \\ f_d & 0 & -f_n \\ -f_e & f_n & 0 \end{bmatrix} \tag{39}$$

$$F_{\epsilon\mathbf{p}} = \begin{bmatrix} -\Omega\sin L & 0 & \dfrac{-v_e}{R_e^2} \\ 0 & 0 & \dfrac{v_n}{R_e^2} \\ -\Omega\cos L - \dfrac{v_e}{R_e\cos^2 L} & 0 & \dfrac{v_e\tan L}{R_e^2} \end{bmatrix} \tag{40}$$

$$F_{\epsilon\mathbf{v}} = \begin{bmatrix} 0 & \dfrac{1}{R_e} & 0 \\ -\dfrac{1}{R_e} & 0 & 0 \\ 0 & \dfrac{\tan L}{R_e} & 0 \end{bmatrix} \tag{41}$$

$$F_{\epsilon\epsilon} = \begin{bmatrix} 0 & -\Omega\sin L + \dfrac{v_e}{R_e\tan L} & \dfrac{v_n}{R_e} \\ \Omega\sin L + \dfrac{v_e\tan L}{R_e} & 0 & \Omega\cos L + \dfrac{v_e}{R_e} \\ \dfrac{-v_n}{R_e} & -\Omega\cos L - \dfrac{v_e}{R_e} & 0 \end{bmatrix} \tag{42}$$

2.2.6 Sparse Data Interpolation.

One of the shared challenges between MagSLAM and traditional aerial magnetic navigation is the interpolation of an expected magnetic value from a noisy map created from sparse and non-gridded measurements. This problem is considered sparse data interpolation and is represented by the $h(x_t, e_t)$ function in equation (12). There are various mathematical approaches available, but the method used in this thesis are described in this section. Solin derived a Bayesian modeling approach for interpolation and extrapolation of the magnetic field by imposing a Gaussian process prior on the potential of the magnetic field [43]. Although his method applied additional constraints with the availability of vector measurements, a Gaussian process regression method is applicable to interpolating and extrapolating the magnetic scalar field as

well. This subsection will follow a simple derivation from Ebden [77] explaining the basic use of Gaussian process regression and introduce the squared exponential kernel used in this research.

2.2.6.1 Gaussian Process Regression.

Ebden defines Gaussian Processes as extending multi-variant Gaussian distributions to infinite dimensionality; generating data located throughout some domain such that any finite subset of the range follows a multivariate Gaussian distribution [77]. A Gaussian distribution is defined completely by it's first two moments, namely mean and variance. A method only needs to determine a mean and covariance between any two points in a Gaussian distribution to characterize it entirely. Establishing an assumption that the mean of a Guassian process is zero everywhere, each observation can be related to another observation with a covariance function denoted as $k(x, x')$. The squared exponential kernel is describe the distance relationship between some x and x' elements in a covariance matrix K:

$$k(x, x') = \sigma_f^2 exp\big[\frac{-(x - x')^2}{2l^2}\big]$$
(43)

where σ_f^2 is the maximum allowable covariance between observations, and l is a length parameter which determines the relative distance at which observations become uncorrelated. This function k can be used iteratively to populate a full set of relative observation covariance terms and therefore describe a dataset as following a multivariate Gaussian distribution. As x approaches x', then $f(x)$ should be highly correlated with $f(x')$. Since each observation also contains measurement noise, the underlying function $f(x)$ we are trying to represent must account for Gaussian noise through the noise model:

$$y = f(x) + \mathcal{N}(0, \sigma_n^2)$$
(44)

Folding the noise component into the $k(x, x')$ function results in the equation:

$$k(x, x') = \sigma_f^2 exp\big[\frac{-(\mathbf{x} - \mathbf{x}')^2}{2l^2}\big] + \sigma_n^2 \delta(x, x') \tag{45}$$

where $\delta(x, x')$ is the Kronecker delta function and adds measurement noise to each observation such that the interpolation function does not have to reside exactly at each observation point. The first step of GPR is to construct three matrices:

$$\mathbf{K} = \begin{bmatrix} k(x_1, x_1) & k(x_1, x_2) & \dots & k(x_1, x_n) \\ k(x_2, x_1) & k(x_2, x_2) & \dots & k(x_2, x_n) \\ \vdots & \vdots & \ddots & \vdots \\ k(x_n, x_1) & k(x_n, x_2) & \dots & k(x_n, x_n) \end{bmatrix} \tag{46}$$

$$\mathbf{K}_* = \begin{bmatrix} k(x_*, x_1) & k(x_*, x_2) & \dots & k(x_*, x_n) \end{bmatrix} \tag{47}$$

$$\mathbf{K}_{**} = k(x_*, x_*) \tag{48}$$

The intended use of GPR is to represent a dataset as a sample from a multivariate Gaussian distribution, which can then be represented as:

$$\begin{bmatrix} \mathbf{y} \\ y_* \end{bmatrix} \sim \mathcal{N}\Big(\mathbf{0}, \begin{bmatrix} \mathbf{K} & \mathbf{K}_*^T \\ \mathbf{K}_* & \mathbf{K}_{**} \end{bmatrix}\Big) \tag{49}$$

where $\mathbf{y}$ is the previous set of observations in the data, and y_* is the expected value we are trying to predict. The conditional probability becomes:

$$p(y_*|\mathbf{y}) \sim \mathcal{N}\Big(\mathbf{K}_*\mathbf{K}^{-1}\mathbf{y}, \ \mathbf{K}_{**} - \mathbf{K}_*\mathbf{K}^{-1}\mathbf{K}_*^T\Big) \tag{50}$$

This means the estimate of the value at observation x_* has a mean of:

$$\hat{y}_* = \mathbf{K}_* \mathbf{K}^{-1} \mathbf{y} \tag{51}$$

and an uncertainty of:

$$var(y_*) = \mathbf{K}_{**} - \mathbf{K}_* \mathbf{K}^{-1} \mathbf{K}_*^T \tag{52}$$

2.2.6.2 Determining GPR Hyper-parameters.

GPR is only as valid as the hyper-parameters $\Theta = \{\sigma_f,\ \sigma_n,\ l\}$. The performance of using GPR as an expected measurement function on a scalar field is directly tied to the choice of parameters. The maximum *a posteriori* estimate of Θ is when $p(\Theta|\mathbf{x}, \mathbf{y})$ is at it's largest. An application of Bayes' theorem corresponds this to maximizing $\log p(\mathbf{y}|\mathbf{x}, \Theta)$. In the case of GPR, this can be written as:

$$\log p(\mathbf{y}|\mathbf{x}, \Theta) = -\frac{1}{2}\mathbf{y}^T\mathbf{K}^{-1}\mathbf{y} - \frac{1}{2}\log|\mathbf{K}| - \frac{n}{2}\log 2\pi \tag{53}$$

An instance of Θ can be found to characterize a sample dataset by running a multivariate optimization algorithm like conjugate gradients, Nelder-Mead simplex, etc. on equation (53).

III. Aerial Simultaneous Localization and Mapping by the Earth's Magnetic Anomaly Field

3.1 Abstract

Instances of global navigation satellite system (GNSS) spoofing and jamming have emphasized the need for alternative navigation methods. A fusion of methods is required to fill the resulting gaps from Global Positioning System (GPS)-denied circumstances. Aerial navigation by magnetic map-matching has been demonstrated as a viable GPS-alternative inertial navigation system (INS)-aiding technique, but requires an accurate magnetic map which is not always available. Magnetic map availability and resolution varies widely around the globe. Removing the dependency on prior survey maps extends the benefits of aerial magnetic navigation methods to small unmanned aerial systems (sUAS) at lower altitudes where magnetic maps are especially under-sampled or unavailable. In this paper, a common simultaneous localization and mapping (SLAM) algorithm known as FastSLAM was modified to use scalar magnetic measurements to constrain a drifting navigation-grade INS to tens of meters in a one-hundred minute flight without the use of a prior magnetic map. Aerial SLAM using Earth's magnetic anomaly field provides a GPS-alternative navigation method that is globally persistent, impervious to jamming or spoofing, stealthy, and locally accurate to tens of meters without the need for a magnetic map.

3.2 Introduction

GPS-alternative navigation technology is a high-interest area of recent commercial and military research. GPS jamming and spoofing is a threat to the use of GPS as a sole means of positioning for the world's critical systems [8, 7]. A fusion of alternative positioning methods is necessary to replace the characteristics of GPS the world has

become addicted to: global availability, passive sensing, absolute positioning, and sub-meter level accuracy. Navigation by matching magnetic measurements to a magnetic map is an advantageous GPS-denied method for INS aiding in the air [21, 19], space [22], on land [23], and underwater [24]. Aerial navigation was demonstrated on a long distance flight with 13 meters of accuracy using a magnetic anomaly map, precision scalar atomic magnetometer, barometer, and an INS [78]. Indoor ambient magnetic anomaly fields have also been used in conjunction with vector magnetometers for pedestrian and robot localization using prior magnetic maps [39, 40, 41, 42, 43, 44]. Navigation using magnetic field anomalies is an attractive GPS-alternative positioning method, but requires prior surveyed magnetic maps. Indoor robotic and pedestrian magnetic navigation methods have utilized SLAM techniques to remove the dependency on a prior magnetic map [58, 55, 59].

3.2.1   Magnetic Maps.

The Earth's outer core produces a magnetic field which is then perturbed by magnetically susceptible materials in the Earth's crust. The resulting deviation from a core field reference model is a world-wide magnetic anomaly field which is stable over time and can be used as a navigation signal. Earth's magnetic anomaly field varies both horizontally and vertically. The spatial variation of the anomaly field increases as altitude decreases, and therefore cannot be mapped from space. High-resolution maps are therefore created with aircraft, where the expense scales with the length of the survey flight. There are two sources of magnetic maps. Individual surveys cover small areas at a single altitude. Compilation products fuse many individual surveys into larger map products. The North American Magnetic Anomaly Database (NAMAD) is built by fusing thousands of individual surveys of varying quality and incorporating satellite and ground observations to resolve long magnetic field wavelengths.

41

3.2.1.1 Map Sampling.

A fully sampled magnetic map satisfies the Nyquist criteria to capture all frequency components of the magnetic field's spatial variation with the proper spacing of magnetic measurements. Survey grid lines must be closer at lower altitudes in order to fully sample the magnetic field, which makes survey flights longer and more expensive. In general, the spacing of survey grid lines must be at most the survey height [79]. Figure 4 illustrates two individual surveys on the left. Survey (B) is fully sampled at 100 meters altitude with 100 meter line spacing. Survey (A) is under-sampled at 300 meters altitude with 500 meter spacing.

3.2.1.2 Map Continuation.

Potential fields can be modeled as a function of distance through a mathematical transformation called continuation. Assuming magnetic sources are below a survey map of infinite size, a magnetic anomaly map can be upward-continued to higher altitudes, but cannot be accurately downward-continued very far. This prevents magnetic navigation at altitudes lower than the survey map. In the maps to the left of figure 4, (A) can be modeled as the upward continuation of (B), but (B) cannot be sufficiently modeled as the downward continuation from (A), even if (A) was fully sampled [79].

3.2.1.3 Map Unavailability.

The World Digital Magnetic Anomaly Map (WDMAM) [80] on the right of figure 4 highlights a few of the many un-surveyed regions of the world as uncolored sections of the map. The colored sections of the WDMAM still contain errors from fusing under-sampled individual maps.
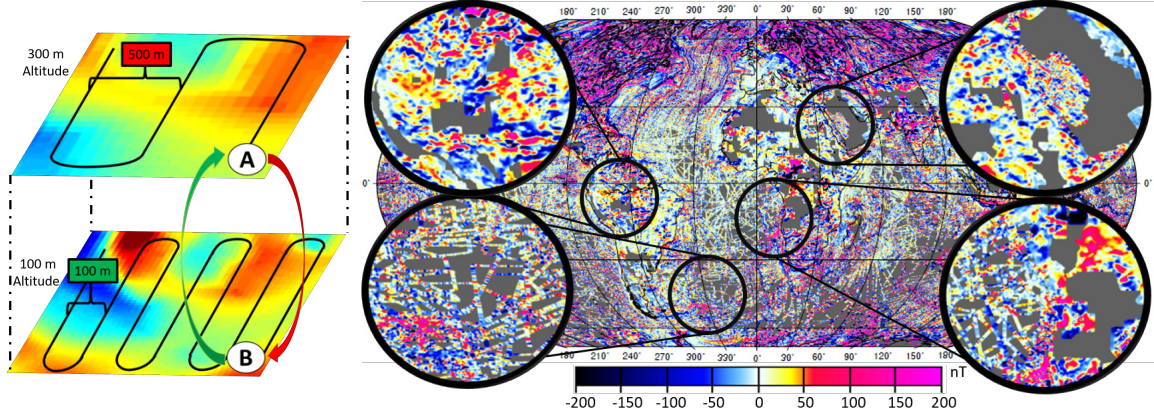
Figure 4. Two individual surveys are illustrated on the left: (B) fully sampled at 100 meters altitude and (A) under-sampled at 300 meters altitude. (B) Can be upward-continued to (A), but (A) cannot be downward-continued to (B). The World Digital Magnetic Anomaly Map on the right highlights a few of the many vast un-surveyed regions of the world [80].

Un-surveyed regions, under-sampled surveys, and downward continuation instability are major obstructions to a world-wide magnetic anomaly map for navigation [25]. This paper applied SLAM techniques from robotics literature to aerial magnetic navigation to remove the dependency on magnetic maps. This paper presents the methodology, flight test results, and a discussion of future areas of improvement.

3.3   Methodology

We modified the common FastSLAM algorithm to estimate INS errors and use them to correct an aircraft state estimate as illustrated in figure 5.
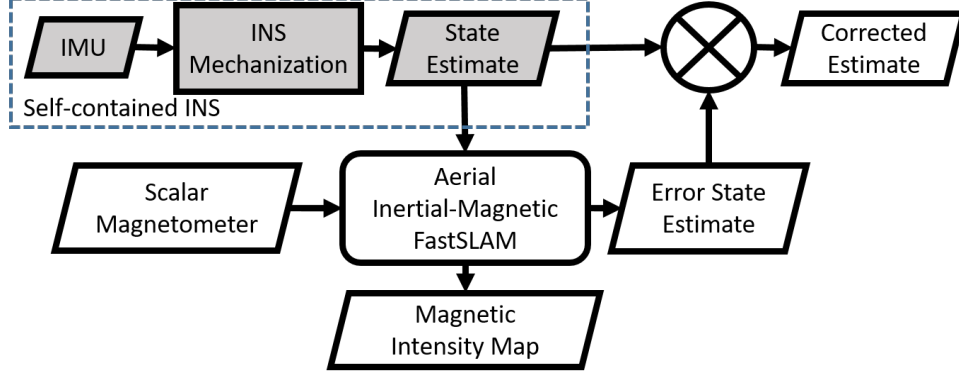
Figure 5. The system loosely coupled an INS solution to magnetic intensity measurements to correct for state errors.

SLAM estimates a path and map concurrently. While the concept of SLAM has been around since 1986 [72], FastSLAM was first introduced by Montemerlo in 2003 as a factored solution to SLAM with unknown data association [73]. Murphy [74] first presented the factorization of the full SLAM posterior into a product of N+1 recursive estimators: one estimator over robot paths, and N independent estimators over landmark positions, each conditioned on the path estimate:

$$p(x_{1:t}, \theta_{1:n}|z_{1:t}, u_{1:t}, n_{1:t}) = \underbrace{p(x_{1:t}|z_{1:t}, u_{1:t}, n_{1:t})}_{\text{trajectory posterior}} \underbrace{\Pi_{n=1}^{N} p(\theta_n|x_{1:t}, z_{1:t}, u_{1:t}, n_{1:t})}_{\text{landmark estimators}}. \quad (54)$$

This factorization can be efficiently approximated with a Rao-Blackwellized particle filter (RBPF) where each sample path of the vehicle is a particle. Each particle maintains it's own hypothesized map and determines when it revisits a portion of it's path. We present an extension of the FastSLAM algorithm used by [58], shown in algorithm 2 to the flight test dataset used by [21] for aerial magnetic navigation.

We will now describe each step of algorithm 2 for a single time-step. On line 2, the i-th of N particles uses it's previous state $x_{t-1}^{[i]}$ and control input u_t to propagate to it's current state $x_t^{[i]}$ according to the nine state Pinson INS error dynamics and noise model further described in the appendix. On line 3, a particle compares

it's current state $x_t^{[i]}$ and measurement z_t to it's map model $m_{t-1}^{[i]}$ and returns an updated weight $q_t^{[i]}$ and list of currently revisiting particles *ActiveList*. On line 4, a particle updates it's individual map $m_{t-1}^{[i]}$ with the latest measurement $x_t^{[i]}$ and trajectory estimate z_t. The weights of the particles that did not hypothesize a revisit are multiplied by the mean of particle weights on the *ActiveList* as shown in line 5. Line 7 states that if the number of effective particles falls below half of the total number of particles, systematic resampling occurs to replace poorly weighted particles with duplicates of highly weighted particles. The process concludes one iteration with an updated set of particles X_t approximating the current state estimate.

Algorithm 2: Aerial Inertial-Magnetic FastSLAM

Input: X_{t-1}, u_t, z_t

Output: X_t

1 **for** $i = 1$ *to* N **do**

2 $\quad$ $x_t^{[i]} = INS\_motion\_model(u_t, x_{t-1}^{[i]})$

3 $\quad$ $[ActiveList, q_t^{[i]}] = update\_particle\_weight(z_t, x_t^{[i]}, m_{t-1}^{[i]}, q_{t-1}^{[i]}, ActiveList)$

4 $\quad$ $m_t^{[i]} = update\_particle\_map(z_t, x_t^{[i]}, m_{t-1}^{[i]})$

5 $q_t^{[\sim ActiveList]} = mean(q_t^{[ActiveList]}) \cdot q_t^{[\sim ActiveList]}$

6 **if** $\frac{1}{\sum_{i=1}^{N}(q_t^{[i]})^2} < \frac{N}{2}$ **then**

7 $\quad$ Resample particles that have revisited since the last resample

8 **return** X_t

Our contributions primarily involve the particle weighting function in line 3 of algorithm 2, and resampling in line 7. The *update_particle_weight*($\cdot$) function is further expanded with a flow chart in figure 6.
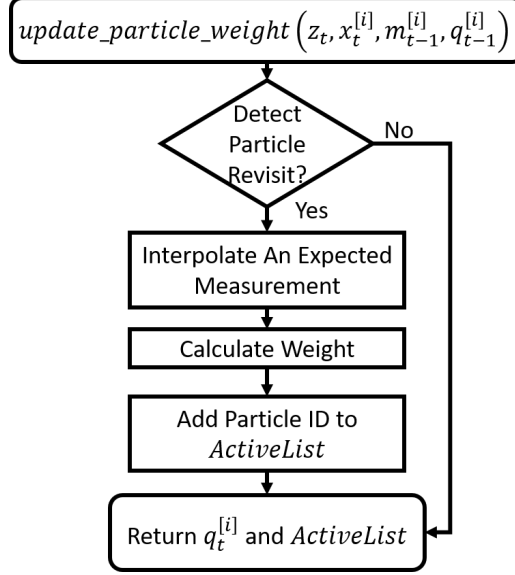
Figure 6. Updating each particle weight depends on if it hypothesizes a revisit or not

We will now step through each part of the process outlined in figure 6.

3.3.1 Detect Particle Revisit.

A particle detected a path crossing when there was more than two points from it's previous trajectory called trigger points within a trigger radius. This is illustrated by figure 7a where colored dots represent the magnetic intensity measurements along a particle's trajectory, squares represent trigger points as tracked points in a particle's trajectory, and asterisks indicate recent points to be ignored. A trigger radius of 18 meters was determined experimentally such that a particle would neither miss nor apply two particle weight updates to the same revisit.

3.3.2 Interpolate An Expected Measurement.

Instead of maintaining an entire map, each particle used a subset of point indices s of it's position history and measurements as inputs into an expected measurement function $\hat{z}^{[i]} = h(x_s^{[i]}, z_s)$. The interpolation points were selected from within a threshold distance as shown in figure 7b. $[t - \tau : t]$ represents a sequence of recent values

46

that were ignored as to prevent recent measurements from affecting the result of interpolation [58].
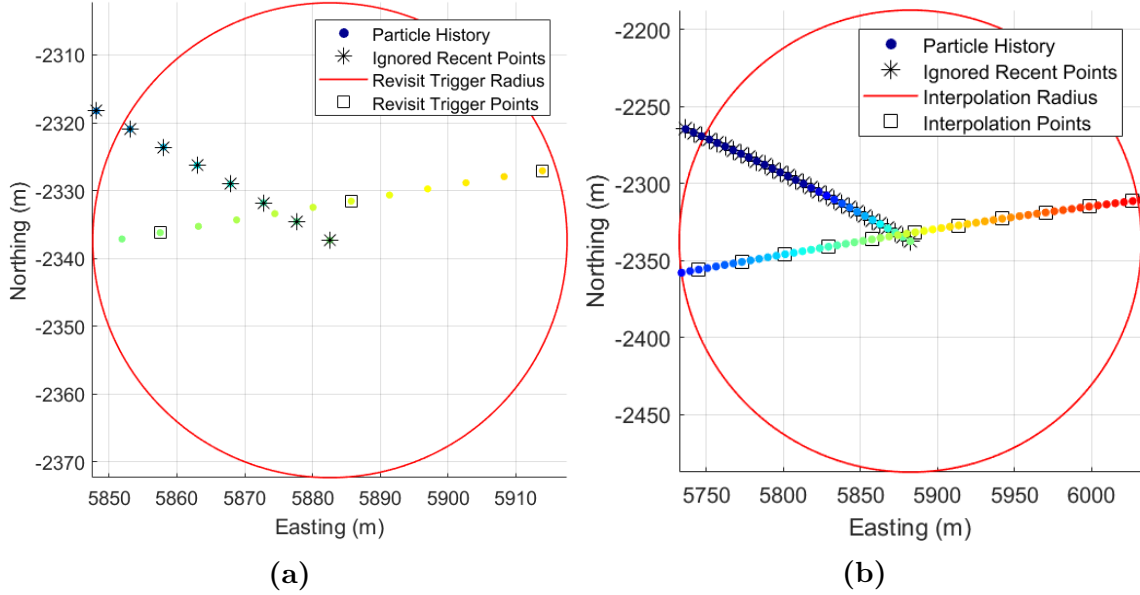
Figure 7. Particles individually detect revisits and select interpolation points conditioned on their own path histories. (a) Detecting a line revisit when # of trigger points withing a threshold radius >2. (b) Data selection for interpolation used a larger radius.

The expected measurement function $\hat{z}^{[i]} = h(x_s^{[i]}, z_s)$ interpolated an expected magnetic intensity measurement from a subset of the non-gridded particle history and magnetic measurements. Two methods were evaluated to interpolate the data. The first method was called ScatteredInterpolant (SI) which determined if the query point was inside the interpolation points. If the query point was inside, a natural-neighbor interpolation was used [81]. Otherwise, a nearest-neighbor interpolation was used to prevent the extrapolation of noisy data. This method is illustrated in figures 8a and 8b.

47
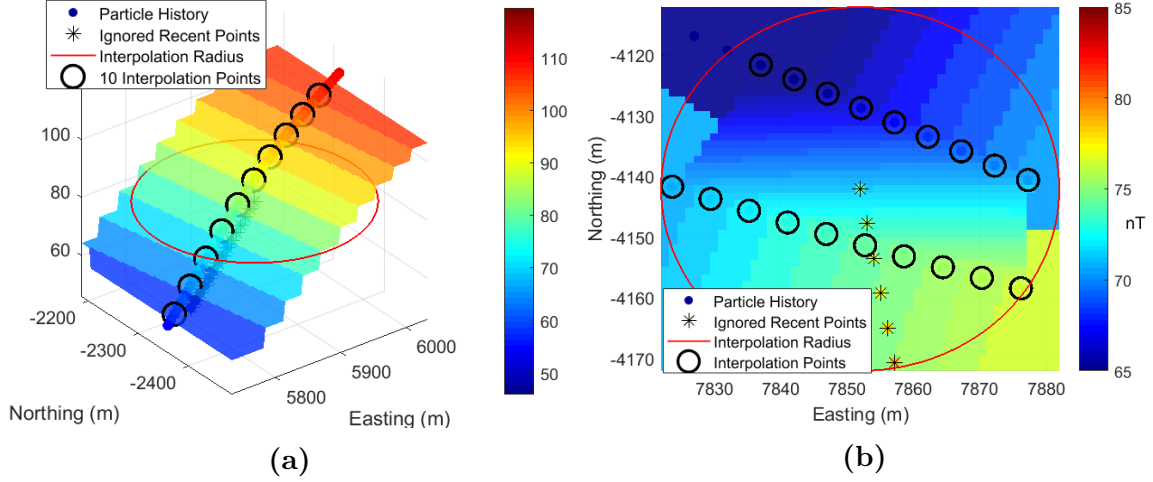
Figure 8. Scattered Interpolant (SI) function estimating a grid given some circled input points. (a) Nearest neighbor around a line of points. (b) Natural or nearest neighbor data interpolation

The second interpolation method used was Gaussian process regression (GPR). GPR evaluated the input coordinates and their associated magnetic measurements as a realization of a zero-mean multivariate Gaussian process according to parameters which characterize the magnetic field. This created a regressive fit function which returned an expected value and covariance for a query point [77]. This method is illustrated in figures 9a and 9b.
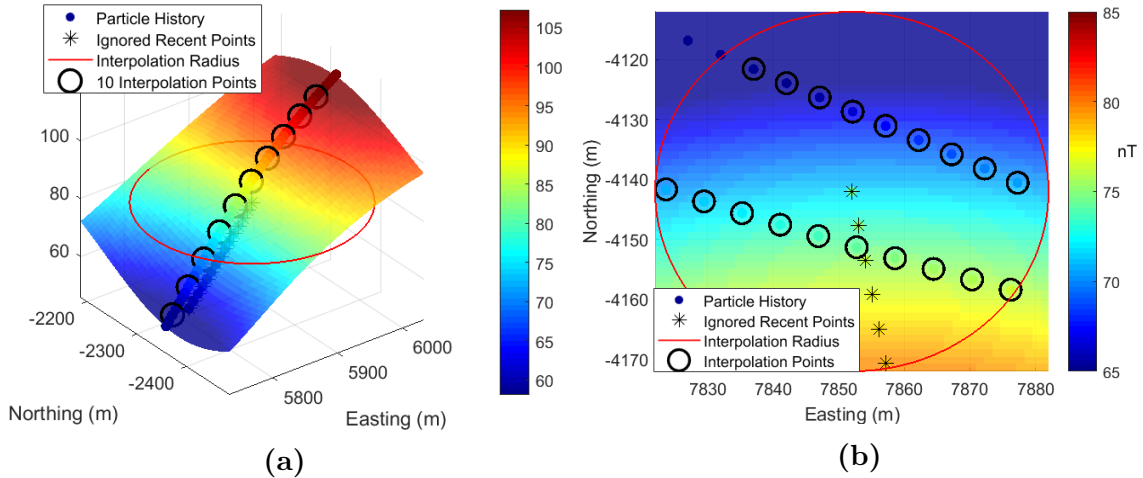
Figure 9. Gaussian process regression estimating a grid of points given some circled input points. (a) GPR prediction around a line of points. (b) GPR prediction around a set of scattered points

48

Magnetic intensity scalar fields are guaranteed to be continuous. GPR had the benefit of modeling the field as a smoothed best fit of measurements, whereas natural and nearest neighbor interpolation only guaranteed piece-wise continuity at the training points. However, as the filter interpolation area gets smaller, both methods were approximately modeling a linear plane as visualized in figures 8 and 9.

3.3.3 Calculate Weight.

Gaussian residual weighting evaluated the quality of a particle's hypothesis by contrasting the expected magnetic intensity with the actual measurement:

$$q_t^{[i]} = q_{t-1}^{[i]} exp\Big(- \frac{(z_t - \hat{z}_t^{[i]})^2}{2R} \Big), \tag{55}$$

where $q_t^{[i]}$ was an active particle's weight at the current time t, $q_{t-1}^{[i]}$ was the particle's previous weight, z_t was the current measurement, $\hat{z}_t^{[i]}$ was the particle's expected magnetic intensity from the measurement function $h(\cdot)$, and R was the filter measurement covariance term experimentally tuned to 100 nano-Teslas. The weighting of particles posed challenges when not all particles hypothesized revisiting at the same time. Haverinen and Vallivaara [58] addressed this by weighting the non-visiting particles by the average weight of the visiting particles. We expanded on this by only resampling from particles which appeared on the *ActiveList* since the previous resampling step. Since information only enters the system during line revisits, this technique prevented the disproportionate favoring of particles which hypothesized many revisits over equally valid particles which were not revisiting as often.

3.3.4 Resampling.

The standard particle filter criteria from Liu[76] was used to determine when to resample:

$$N_{eff} = \frac{1}{\sum_{i=1}^{N}(q^{(i)})^2}, \quad \text{Resample If } N_{eff} < \frac{N}{2} \tag{56}$$

Where N is the total number of particles. Only particles which appeared on the *ActiveList* since the previous resampling step were resampled.

3.4 Flight Test

A Cessna 208B like the one shown in figure 10 collected magnetic intensity measurements, barometric altitude measurements, an un-aided INS solution, and a GNSS-aided INS truth trajectory. This dataset was collected by Sander Geophysics Limited under United States Air Force contract in July of 2015.

Figure 10. Sander Geophysics Limited (SGL) Cessna 208B [2]

Two flight patterns were flown over a 9 km by 12 km area, 150 meters above ground level (AGL) in Louisa Virginia as shown in figure 11a. The first was a gridded survey to map the magnetic intensity field. The second was a looping flight pattern. These flights originally demonstrated map-based aerial magnetic navigation in [4] achieving accuracies of 13 meters distance root mean squared (DRMS) over a one-hour flight. The second flight's many loops and path crossings made it a viable dataset to apply

SLAM techniques. Figure 11b illustrates the magnetic anomaly intensity varying horizontally over the flight area.
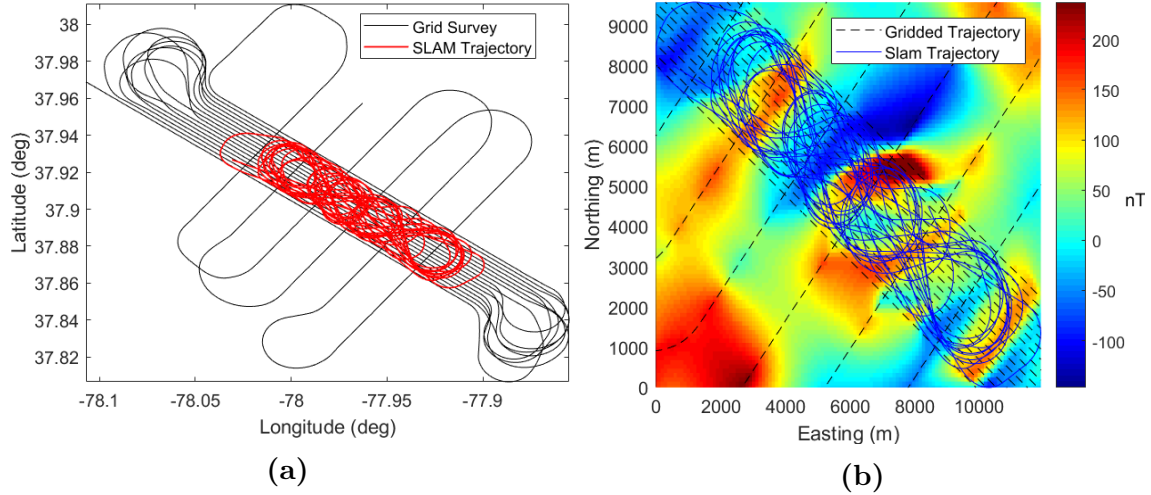
Figure 11. Gridded and SLAM flight patterns. (a) Flight patterns in latitude and longitude. (b) Flight paths in relative horizontal distance over an interpolated magnetic anomaly field intensity.

3.4.1 Isolating Earth's Magnetic Anomaly Field.

The navigation signal used in this filter was created by perturbations in the Earth's core magnetic intensity field from ferrous crustal formations. Magnetic intensity measurements primarily include the Earth's core field, the crustal anomaly signal, aircraft disturbances, and temporally varying space-weather affects known as diurnal magnetic variations.

$$B_{measured} = B_{Core} + B_{Diurnal} + B_{Aircraft} + B_{Anomaly} \tag{57}$$

The anomaly signal was approximated by removing the World Magnetic Model (WMM) core model, diurnal variations, and aircraft affects from the magnetic measurements. The WMM is sponsored by the U.S. National Geospatial-Intelligence Agency (NGA) and the U.K. Defense Geographic Centre (DGC), and is produced by the U.S. Na-

tional Oceanic and Atmospheric Administrations National Geophysical Data Center (NOAA/NGDC) and the British Geological Survey (BGS). It is the standard model used by the U.S. Department of Defense (DoD), the U.K. Ministry of Defence, the North Atlantic Treaty Organization (NATO) and the International Hydrographic Organization (IHO), for navigation, attitude and heading referencing systems using the geomagnetic field. It is also used widely in civilian navigation and heading systems [1]. The Earth's core magnetic intensity field was planar over the flight areas as the WMM shows in figure 12a. Diurnal measurements observed at a separate ground station were recorded during the SLAM flight as shown in figure 12b. Aircraft disturbance affects were determined through prior aircraft characterization by the geo-surveying company and are shown in figure 12c. The crustal anomaly field provides most of the variation of the magnetic intensity field as shown by contrasting the WMM in figure 12a, with figure 12d.
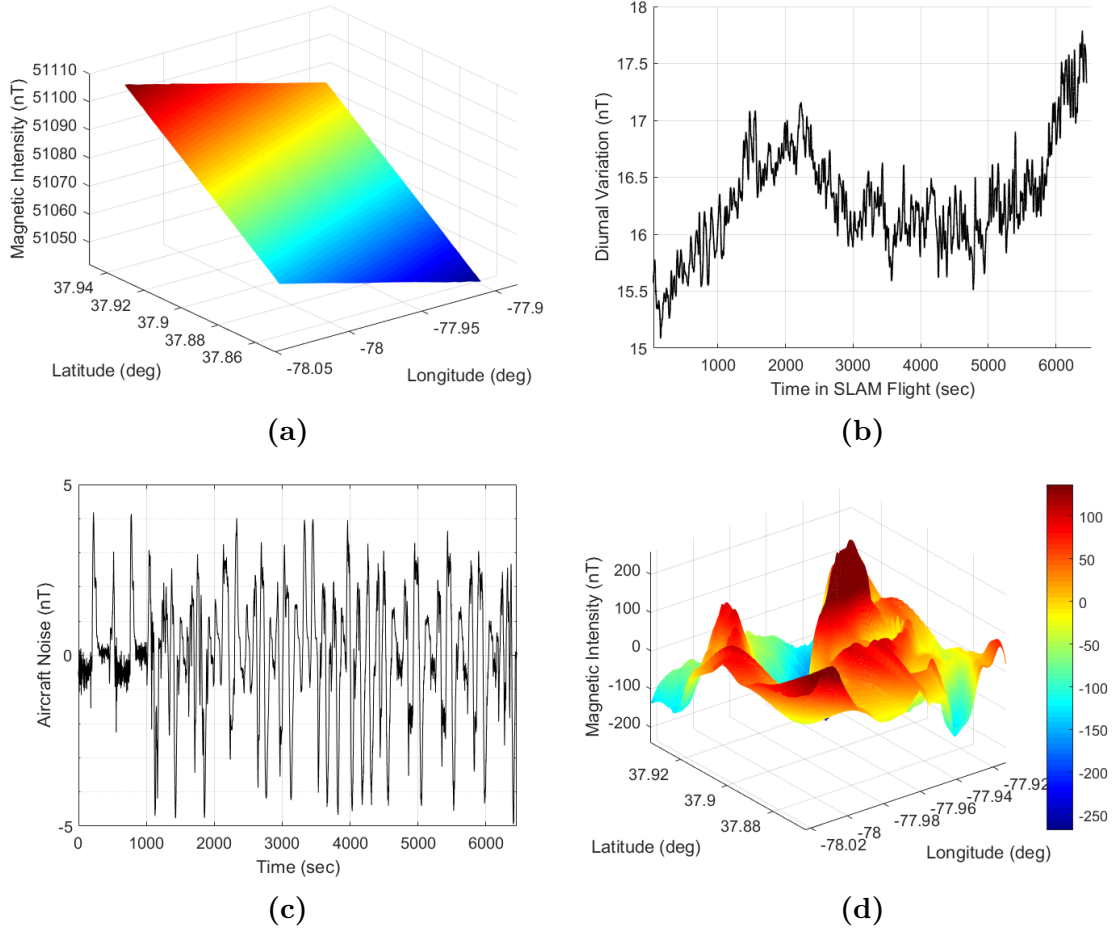
Figure 12. Components of the magnetic intensity measurements. (a) 2015 WMM model over survey area. (b) Diurnal variations during SLAM flight. (c) Aircraft disturbance effects. (d) Isolated magnetic anomaly field.

3.4.2 Drifting INS State Estimate.

INSs measure the relative motion between the local vehicle body frame and the inertial reference frame. Vehicle dynamics are estimated by integrating measured acceleration and angular rate disturbances in the body frame and then transforming them to the local navigation frame to determine position and velocity estimates. Multiple integrations of measurement noise in the INS inevitably leads to a drifting navigation solution. State estimation uses linearized models to estimate the accumulating error states in the INS. The Pinson INS error model from Titterton and

Weston [9] was used to shape additive Gaussian white noise into angular and velocity random walk errors, which are coupled to form drifting horizontal and vertical position estimates. A navigation grade INS provided a real time navigation solution. The drifting horizontal position errors in northing and easting components are shown in figure 13.
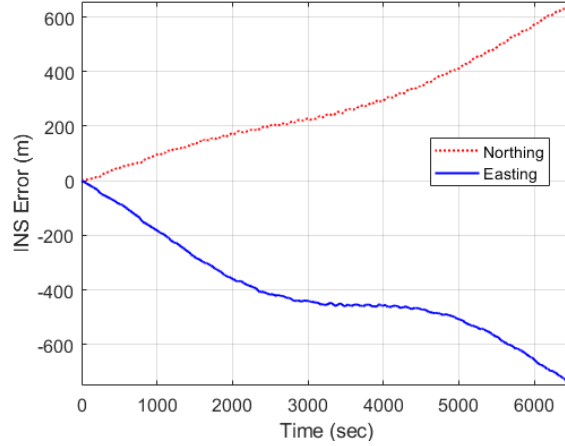
Figure 13. Northing and easting drift of actual INS

3.5   Results

SLAM estimates a vehicle path and map concurrently. The filter performance can be illustrated in its ability to correct the magnetic map. The INS, filter, and truth trajectories are plotted in figure 14. The colors correspond to the same set of magnetic intensity measurements with the mean removed. Comparing the INS estimate, SLAM solution, and GPS truth trajectories overlaid with the same set of zero-mean magnetic intensity measurements illustrates the how position errors lead to measurement inconsistencies at path intersections.
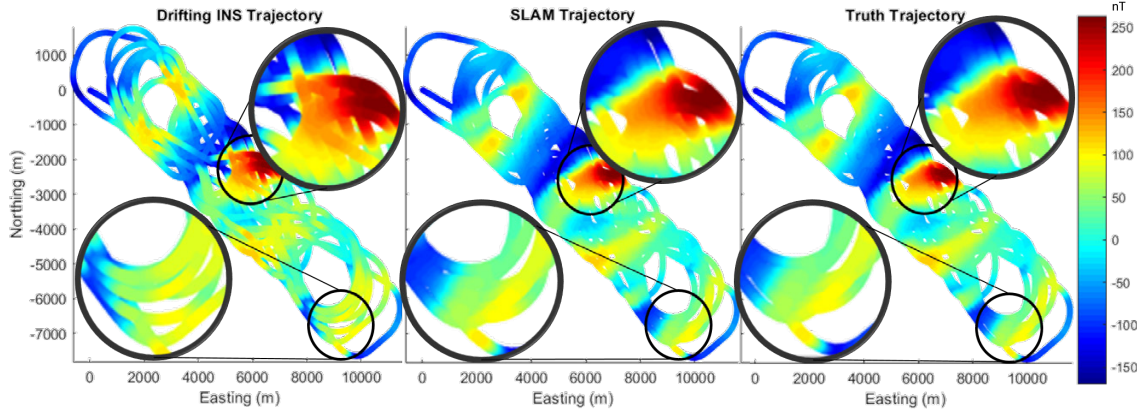
Figure 14. Comparing the INS estimate, SLAM estimate, and GPS truth trajectories overlaid with the same set of zero-mean magnetic intensity measurements emphasizes the correlation between position errors and measurement inconsistencies.

Although SLAM provides both a map and path estimate, this research focused on it's navigation potential. The filter converged to a relative position solution with a self-consistency of less than twenty meters as seen in table 2 and figure 15. Table 2 compares original error of the INS to the performance of the filter using the two different interpolation methods. In this instance, GPR slightly outperformed SI in both root mean square (RMS) error and the standard deviation of the error which indicates the self-consistency of the filter. Interestingly, the filter performed around only 15% worse when using raw instead of compensated measurements. This can be partly attributed to small heading errors and relatively minor aircraft disturbances in the magnetic measurements. Additionally, the short time between revisiting trajectories relative to the time varying components of diurnal variation and WMM fluctuation kept the actual magnetic field time-invariant for this flight. In other words, the spatial variation in the magnetic anomaly field dominated the time variant components of space-weather effects over a short time-span.

Table 2. Filter performance after convergence

Method	N_{part}	North RMS $/\sigma$(m)	East RMS/σ(m)	DRMS/σ (m)
INS	$\sim$	320.6/170.2	438.8/176.5	543.5/239.3
GPR	1000	9.4/9.4	14.2/14.1	17.0/9.1
SI	1000	18.46 /11.35	24.11/17.97	30.36/10.46
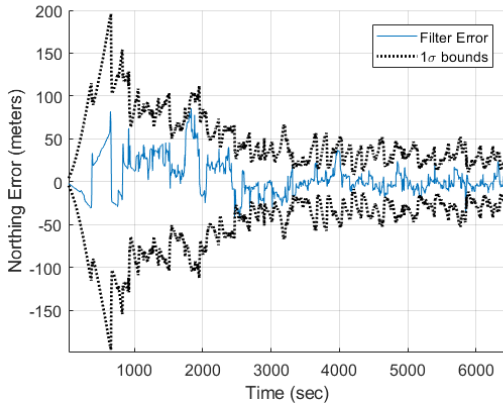
(a)
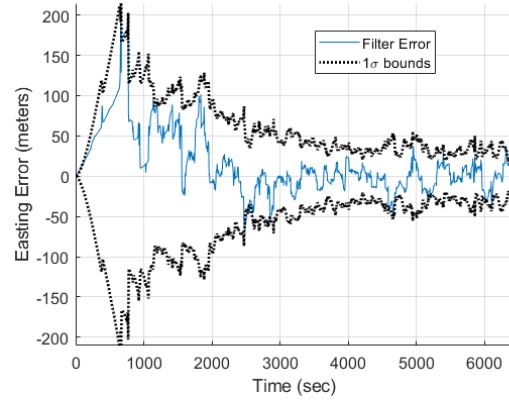
(b)
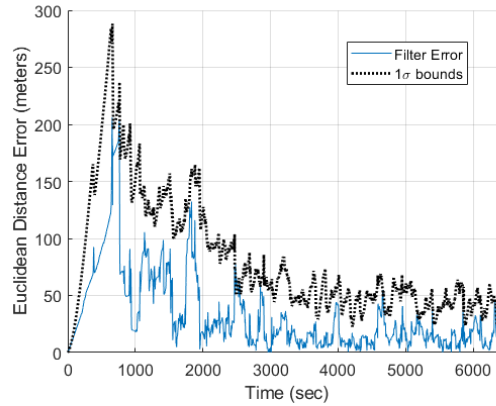
(c)

Figure 15. Filter errors and 1σ bounds using 1000 particles and R=100. (a) Northing position error. (b) Easting postion error. (c) Euclidean distance error.

The filter converged on self-consistent solutions using both methods with errors and standard deviations in the tens of meters. Although this research does not present an in-depth trade-space analysis of using one version of interpolation over the other,

56

some trade-offs between interpolation models were apparent. GPR had the potential to more realistically model a scalar magnetic field since it produced a smoothly varying value estimate from noisy measurements, but required some knowledge about the magnetic intensity correlation over distance. The nearest and natural neighbor interpolation methods did not require any previous knowledge about magnetic correlations, but were more sensitive to measurement noise since the method was an interpolation and not a regressive best-fit model. A more obvious opportunity for improvement would be to incorporate a more realistic INS error model which includes accelerometer and gyroscope bias terms which are a significant source of INS drift. A better INS error model would provide a better proposal distribution and provide a more accurate filter. There is significant potential for computational improvements as this research did not leverage the binary tree particle history structure of FastSLAM. It is worth exploring graph-based methods, which have had promising results in WiFi SLAM in [65].

3.6   Conclusion

There are many research efforts to provide viable GPS-alternative navigation methods. Magnetic navigation shows promise as one such method, but is limited by the requirement for globally available and accurate magnetic maps. These maps greatly vary in quality and altitude. Low altitude magnetic maps are the most uncommon and innacurate which presents a barrier to using magnetic navigation on low-flying unmanned aerial vehicles (UAVs). SLAM uses previous measurements and a revisiting trajectory to create a map and use it to navigate at the same time. This removes the dependency on a prior magnetic map for aerial magnetic navigation, especially for low-flying UAVs or in areas without magnetic maps. This paper introduced a RBPF that loosely coupled magnetic intensity measurements with an INS

solution to constrain drifting errors to a relative position solution of tens of meters. This research has shown that the map dependency in aerial navigation can be removed by leveraging magnetic SLAM techniques in robotics. Aerial magnetic SLAM is a globally-available, passively sensed, and unjammable GPS-alternative navigation method that does not require a prior-magnetic map.

IV. Flight Test Results for an Unmanned Aerial Magnetic Surveying Vehicle

4.1 Abstract

Recent advances in manufacturing technologies have reduced the size and power requirements of atomic magnetometers by orders of magnitude while maintaining measurement precision. The size, weight, and power requirements of magnetic surveying vehicles can now also be reduced. Typical magnetic surveying aircraft utilize long mounting booms or stingers to extend the sensors away from the aircraft to reduce vehicle magnetic disturbances. Special calibration considerations are needed to configure a miniaturized survey vehicle without booms where aircraft disturbances become a dominant source of error. This research had two objectives. The first was to design a low-cost magnetic surveying unmanned aerial vehicle (UAV) from commercial off-the-shelf (COTS) components. The second was to collect spatially consistent magnetic measurements from low-altitude survey flights. A COTS fixed-wing UAV magnetic surveying configuration produced six consistent maps at various altitudes over a 2 kilometer area. Two orthogonally-mounted and co-located Geometrics micro-fabricated atomic magnetometer™ (MFAM) sensor modules guaranteed a dead-zone-free magnetic intensity measurement regardless of aircraft position, altitude, or orientation. Measurements from an uncalibrated micro electro-mechanical systems (MEMS) compass and precision scalar magnetometer from low-altitude calibration flights in the presence of a spatially-varying magnetic field were used to create a magnetic disturbance model for the UAV. The disturbance model corrected proceeding flights for significant heading-correlated errors to produce spatially consistent maps within 1 nano-Tesla. A low-cost, unmanned magnetic surveying aircraft configuration is a precursor to aerial magnetic navigation for UAVs at low-altitude as a

59

Global Positioning System (GPS)-alternative navigation method.

4.2 Introduction

Recent advances in manufacturing technologies have reduced the size and power requirements of atomic magnetometers by orders of magnitude while maintaining measurement precision. The comparison of two Geometrics atomic magnetometers in table 3 shows the reduction in size weight and power (SWAP) between an optically pumped cesium scalar magnetometer (G-823A), and self-oscillating MFAM. The MFAM requires significantly less SWAP without suffering in precision. Although the miniaturized sensors only have one dead zone, heading errors and dead-zone size are significantly larger than the G-823-A. To combat this trade-off, combining measurements from two sensor heads can either reduce heading errors or eliminate dead-zones, depending on the sensor configuration. Figure 16 illustrates the recent reduction in scalar magnetometer manufacturing [3].

Figure 16. Geometrics MFAM [3]

Table 3. Magnetometer Comparison

Magnetometer	G-823A	MFAM
Size	41259 cc	15 cc
Weight	450 g	30 g
Power	12-16 W	2 W
Sensitivity	$4\ pT/\sqrt{Hz}$	$1\ pT/\sqrt{Hz}$
Heading Error	$\pm 0.15\ nT$	$\pm 30\ nT$
Dead Zones	(2) Equilateral, Polar, 10 °	(1) Polar, 35 °

Geomagnetic surveying aircraft use scalar magnetometers and gridded survey patterns to create maps of the Earth's magnetic anomaly field for geological analysis of the Earth's crust. These maps can be used for mineral and petroleum exploration, locating orphaned oil wells [82], and characterizing fault zones [83]. Magnetic anomaly maps have also been used for aerial and marine navigation [4, 24, 32].

4.2.1   Magnetic Surveying Aircraft Configuration.

Long mounting booms or suspended platforms are traditionally used to reduce vehicle magnetic disturbances by extending the sensors as far away from the aircraft as possible. Figure 17 shows a professional magnetic surveying aircraft configuration with magnetometers mounted with stingers and wing outboard extensions. Remaining heading-correlated magnetometer errors can be characterized with calibration flights and an aircraft disturbance coefficient model for removal during postprocessing. Incorporating miniaturized magnetometers into magnetic surveying reduces the SWAP requirements of survey aircraft.

Figure 17. Sander Geophysics Limited (SGL) Cessna 208B [2]

4.2.2 Unmanned Aeromagnetic Systems.

There are obvious benefits to using UAVs in place of full-sized aircraft for magnetic surveying. Surveys using UAVs could be automated, flown by several aircraft simultaneously at differing altitudes at lower safety risk, require less access to airports, and become significantly more profitable. As a result, Geosurveying companies have begun to incorporate UAVs into their magnetic surveys [84, 85, 86, 87, 88].

4.2.2.1 UAV Configuration.

The configuration of magnetically susceptible aircraft components in proximity to a magnetometer determines the severity of the resulting aircraft noise in the measurements. The use of booms and stingers on light-weight fixed-wing UAV can be impractical due to the additional structural weight and detriment to aircraft control. Special considerations are needed to configure a miniaturized survey aircraft without booms or tow-lines where aircraft disturbances become a dominant source of error.

Huq conducted an extensive analysis of a servo actuator's magnetic disturbance in a UAV [89]. Zhiwen introduced a better power-supply design specifically to reduce the magnetic disturbance of unmanned aeromagnetic system (UAMS) electronic components on magnetic measurements [90]. Cherkasov, Kapshtan and Sterligov attempted to make aircraft magnetic effects negligible through aircraft configuration only, with-

out the need for a vector magnetometer identified the challenges of minimizing UAV magnetic footprints with the motors and servos being the primary source of aircraft magnetic field disturbances [91, 92]. They used a combustion engine, placed magnetic sensors at the wing-tips, and positioned servo actuators in the central body of the aircraft to reduce the aircraft's magnetic disturbance to less than 2 nano-Teslas. Although their UAV did not fly successfully, their analysis concluded that designing an UAMS requires deliberate consideration on UAV configuration and magnetometer placement to minimize the magnetic influence of the aircraft and its components on the magnetic measurements.

4.2.2.2   UAV Calibration.

Tolles and Lawson modeled an aircraft's magnetic disturbance as a function of aircraft orientation relative to the surrounding magnetic field [69]. UAVs can use this aircraft model with tri-axis vector magnetometer measurements to remove aircraft effects from scalar magnetic intensity measurements [93, 70]. A high-altitude flight with various aircraft maneuvers excites a full range of aircraft orientations in an area of assumed zero magnetic gradient. It is assumed that any changes in the scalar measurement are from aircraft maneuvers. Direction cosine terms from a vector magnetometer can be correlated with a set of characterization coefficients to what is assumed to be a scalar measurement of the aircraft disturbance field. This set of aircraft coefficients describes the relationship between the orientation of the aircraft and the aircraft disturbance. These coefficients are valid for modeling the aircraft disturbance field during following flights as long as the aircraft configuration does not change.

4.2.3 Configuring a UAV for Magnetic Navigation.

Magnetic surveys conducted with UAVs for the purpose of generating magnetic maps include extensive data processing after the flight [79, 86]. Aircraft disturbances are first minimized by placing magnetic sensors far from magnetically susceptible vehicle components, and then removed from survey data using post-processing methods. Magnetic disturbances must be estimated and removed from magnetic measurements during flight in order to conduct aerial magnetic navigation with a UAV.

This paper presents a magnetic surveying UAV configuration, calibration methodology, flight test results, and discusses future applications of calibrated UAVs with magnetic sensors.

4.3 Methodology

This experiment built, calibrated, and flew a low-cost UAV to near industry magnetic surveying standards with commercially available components. This section presents the aircraft disturbance characterization model, how to use an aircraft characterization to compensate measurements from subsequent flights, and the UAV configuration.

4.3.1 Aircraft Disturbance Model.

A modified Tolles-Lawson model closely following [70] was used to incorporate the spatial gradient of the magnetic field at low-altitude and account for some of the difference in precision between the three-axis magnetometer and atomic scalar magnetometer. The method implemented to solve for a set of calibration coefficients is detailed here.

4.3.1.1 Modified Tolles Lawson Model.

A vector magnetometer produced three magnetic intensity measurements along it's Cartesian axes, B_x, B_y, and B_z. They were normalized by the total intensity $B_m = \sqrt{B_x^2 + B_y^2 + B_z^2}$ to produce the vector u of direction cosine terms:

$$\cos(x) = \frac{B_x}{B_m}, \quad \cos(y) = \frac{B_y}{B_m}, \quad \cos(z) = \frac{B_z}{B_m}, \quad u = \begin{bmatrix} \cos(x) \\ \cos(y) \\ \cos(z). \end{bmatrix} \tag{58}$$

An atomic magnetometer produced a measurement of the total magnetic intensity B_s. The difference in precision between the tri-axis and scalar magnetometers produces different magnetic intensity measurements: $B_m \neq B_s$. This imbalance was captured by the term:

$$\lambda = \frac{B_m}{B_s}. \tag{59}$$

The aircraft magnetic disturbance field is modeled in [70] as:

$$B_{dist} = \delta\theta + \tau_s, \tag{60}$$

where

$$\delta = \begin{bmatrix} \lambda\bar{u}_i, & \lambda\bar{u}_i\bar{u}_j, & \lambda\dot{\bar{u}}_i\bar{u}_j \end{bmatrix}_{t\times 21}^{\{i,j=1,2,3\}}. \tag{61}$$

θ denotes of the column vector consisting of 21 coefficient terms, and τ_s represents the compass's Gaussian wide-band noise and null-shift error. τ_s is ignored in this application but scale-factor, non-orthogonality, and misalignment compass errors with respect to the aircraft axes were captured in θ cross terms.

4.3.1.2 Accounting for the Spatial Gradient.

The assumption of a non-varying earth magnetic field for a calibration flight at low altitudes is invalid. When a calibration flight is flown over a relatively small area, the variation of the magnetic anomaly field can be approximated as linearly sloped, and accounted for in the coefficient model. Horizontal position measurements were appended to θ to account for the effects of a planar spatial gradient model from a dataset at a constant altitude.

$$\eta = \begin{bmatrix} \theta \\ e_1 \\ e_2 \end{bmatrix}_{23 \times 1} \tag{62}$$

The additional terms e_1 and e_2 correspond to easting and northing position in meters appended to the end of δ.

$$\triangle = \begin{bmatrix} \delta & Easting & Northing \end{bmatrix}_{t \times 23} \tag{63}$$

4.3.1.3 Accounting for Space-Weather Effects.

The interaction between the magnetosphere and solar wind creates small variations in Earth's magnetic field and are present in a survey vehicle's magnetic measurements. These magnetic temporal variations can be observed using a base-station magnetometer on the ground and later removed from the measurements.

4.3.1.4 Correcting Magnetic Measurements.

The process for correcting UAV magnetic measurements can be summarized as follows:

1. Solving For Aircraft Characterization Coefficients

(a) Use a calibration dataset to generate a $t \times 23$ matrix $\triangle$ according to [70] to include horizontal position measurements.

(b) Use a non-linear least squares solver to solve for the 23 coefficients: $\underset{\eta}{argmin}(\triangle\eta - (B_s - mean(B_s)))$.

(c) The first 21 coefficients θ characterize the aircraft configuration's disturbance field.

2. Compensating Real Measurements On Separate Flights

(a) A row-vector δ from compass direction cosines, their derivatives, and the magnitude ratio between the compass and the scalar magnetometer λ was constructed at each time step.

(b) The row vector δ was multiplied by the calibration coefficients to produce the aircraft disturbance signal.

(c) The aircraft disturbance signal was subtracted from the raw measurements.

(d) The corrected raw measurements were passed through a 1Hz low-pass filter $f_{LP}(B_s - \delta\theta)$

4.3.2 Aircraft Configuration.

An Aeroworks 40% scale Carbon-Cub kit was used as the base air-frame and outfitted with a 120cc, two-cylinder, two-stroke engine in addition to an open-sourced Pixhawk autopilot for autonomous surveying capabilities.

Figure 18. 40% scale Aeroworks Carbon-Cub survey aircraft

Table 4. Example Surveying Aircraft Comparison

Integrator	Thompson Aviation		AFIT
Airframe	Cessna 210	UAM II	40% Carbon Cub
Endurance	5 Hrs	90 min	45 min
Survey Velocity	100 m/s	20 m/s	22 m/s
Wingspan	11.2 m	2.4 m	4.3 m
Minimum Safe Alt	100 m AGL	30 m AGL	30 m AGL
Coverage (Flat Terrain)	1300 Line km	110 Line km	60 Line km

4.3.2.1   Sensor Payload.

A sensor payload was assembled and flown by Air Force Institute of Technology (AFIT)'s Autonomy and Navigation Technology (ANT) center. These components were chosen with special consideration to commercial availability and interoperability. The sensor payload consisted of:

1. Geometrics MFAM™ development kit

    (a) Scalar atomic oscillating magnetometer x2

(b) MEMS gyroscope and accelerometer: BMI160

(c) MEMS vector magnetometer: HMC5983

(d) GPS module: Adafruit Shield

2. Cameras

(a) Proscilica HD camera

(b) DAVIS event-based vision sensor

3. Navigation solutions

(a) Piksi global navigation satellite system (GNSS) navigation unit

(b) VectorNav unaided inertial navigation system (INS)

(c) PixHawk 2 GPS-aided autopilot - flight controller

(d) PixHawk 2 GPS-independent - standalone autopilot

4. HMR2300 vector magnetometer

The Piksi GNSS navigation unit provided a differential-GPS solution accurate to tens of centimeters through post-processing methods. Two Pixhawk autopilots were included: one active GPS-aided flight controller, and one GPS-disabled standalone autopilot. The active autopilot was used to conduct the flight test autonomously from a mission profile of GPS waypoints at a desired altitude. The passive autopilot, VectorNav inertial measurement unit (IMU), cameras, and HMR vector magnetometer were included for future navigation-related research. The sensor payload board was placed in the main cockpit aligned with the aircraft's body axes. An on-board Linux computer and precision time protocol (PTP) server provided time-synchronized data collection from all components except for the MFAM development kit which was independently clock-disciplined from the Adafruit GPS module.

4.3.2.2 Micro-Fabricated Atomic Magnetometer[TM].

Until recently, traditional atomic magnetometers like the ones used in geomagnetic surveying or submarine detection aircraft have been too heavy, expensive, and impractical for small UAVs. This experiment chose to use the MFAM from Geometrics because it was small, lightweight, efficient, eliminated measurement dead-zones with two sensors, and offered interoperability conveniences with it's development kit. The MFAM specifications and data analysis is presented in this section.

MFAM Specifications. The Geometrics MFAM development kit included two scalar magnetometers, MEMS compass, MEMS accelerometer, MEMS gyroscope, and GPS time-synchronization to 400 nanoseconds. The kit was configured to record time-stamped measurements to an on-board micro-sd card. Figure 19 shows a top view diagram of the sensor electronic box and one of the two sensor heads attached by a 20 inch ribbon cable. The specifications for the major components in the development kit [94] are listed in table 5.
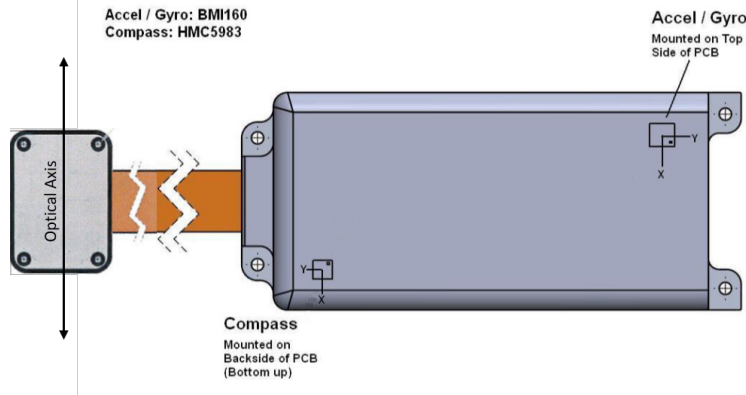
Figure 19. MFAM sensor head, 20 inch ribbon, and electronics box [94]

Table 5. MFAM Dev Kit Specifications

MFAM module	Accuracy	Range	Sensitivity	BW	F_s
Scalar Magnetometers	5 pT/$\sqrt{Hz}$	17-100 μT	0.05 pT	400 Hz	1 kHz
Compass: HMC5983	1-2 °	±0.88 Gauss	73 nT	∼	100 Hz
Accelerometer: BMI160	1.5 mg	±2 g	∼	80 Hz	200 Hz
Gyroscope: BMI160	0.7°/s	±2000°/sec	0.06°/s	74.6 Hz	200 Hz
Adafruit GPS module	3m	∼	165 dBm	∼	1 Hz

MFAM Analysis. The first step to minimize the UAV magnetic disturbance was by characterizing the aircraft components' proximity effects on the magnetic measurements. This section provides familiarity with the MFAM data and the qualitative analysis conducted in order to determine the placement of the sensors on the aircraft.

MFAM Diurnal Data Collection. The MFAM and a full-sized GEM optically-pumped scalar magnetometer co-collected measurements for an 18 hour duration on the 15th of September 2018. The sensor setup is shown in figure 20 with both sensors co-located in a suburban environment. Although intermittently disturbed by local rural disturbances, measurements covering most of a daytime cycle are compared in figure 21a. This collection illustrated the slowly-varying components of the space-weather affects as well as a performance comparison between the MFAM and traditional full size scalar magnetometers. A close look at commonly observed micro-pulsations is shown in figure 21b. It was observed that common large spikes in the magnetic measurements corresponded to vehicle traffic approximately 30 meters away. It was also observed that the opening of a refrigerator door approximately 15 meters away corresponded with a 2 nano-Tesla change in the measurements. This data collection validated the performance comparison between a traditional optically-

pumped atomic magnetometer and the MFAM with significantly smaller size, weight, and power.
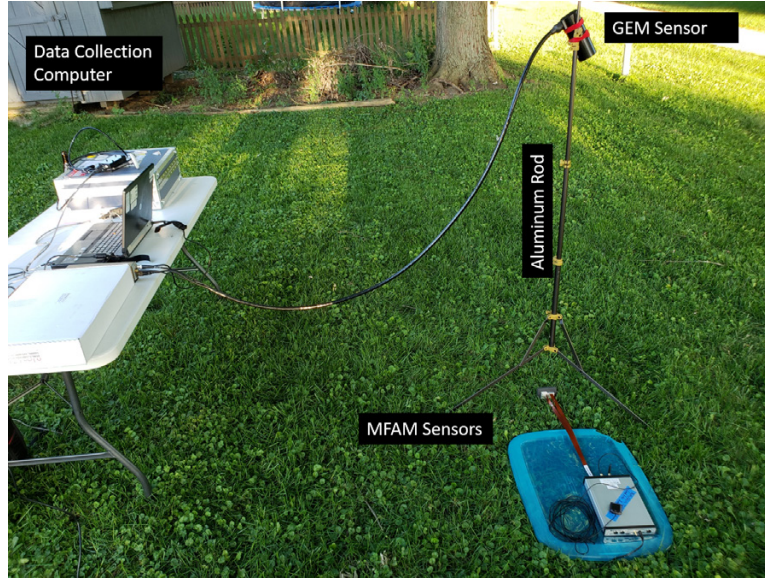
Figure 20. GEM Systems GSMP-35 and Geometrics MFAM magnetometer setup

(a)　　　　　　　　　　　　　(b)
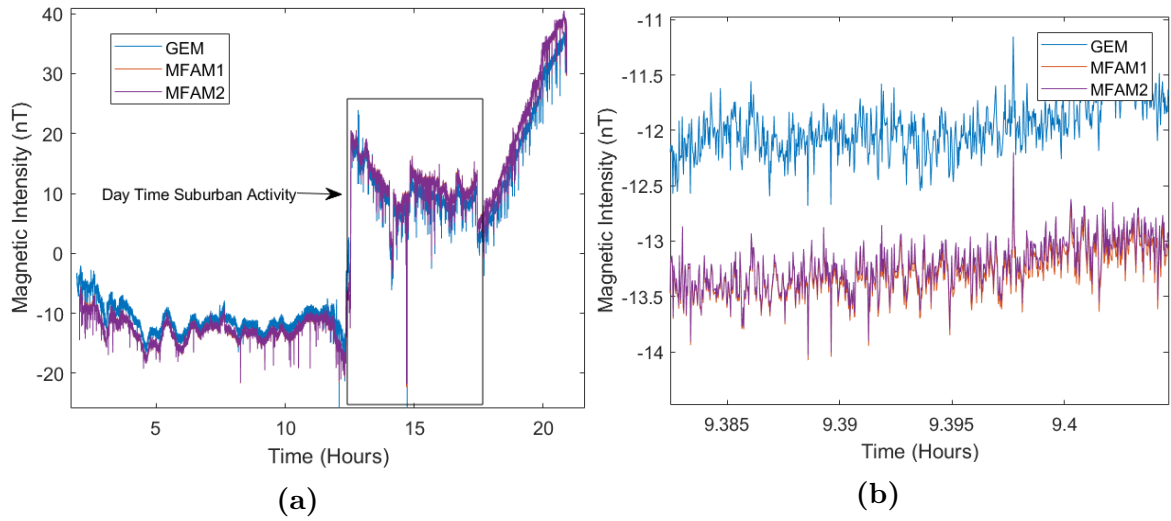
Figure 21. 18 hours of stationary zero-mean measurements with a full-size and MEMS sized scalar magnetometer. (a) The full 18-Hour collection of 1 GEM ground magnetometer and 2 MFAM sensors show the long term consistency. (b) A 10 minute period shows the consistency between all three magnetometers.

MFAM Raw Data Collection. The MFAM magnetic measurements on the ground exhibit diverse frequency content. The power grid in the United States

operates at 60Hz, inducing magnetic noise at 60, 120, 180, 240, 300, and 360 Hz in proximity of electrical power infrastructure. These power components were not as prevalent when flying at 450m above ground level (AGL), but still needed to be filtered out. The sample rate of the MFAM was 1 kHz, but the practical bandwidth was 400 Hz based on sensor specifications [95]. A series of notch filters were designed to remove the 60 Hz saw-tooth-like noise which was drowning out meaningful signal from the tests. A 50 Hz low-pass filter was also implemented to isolate the lower bandwidth of interest.
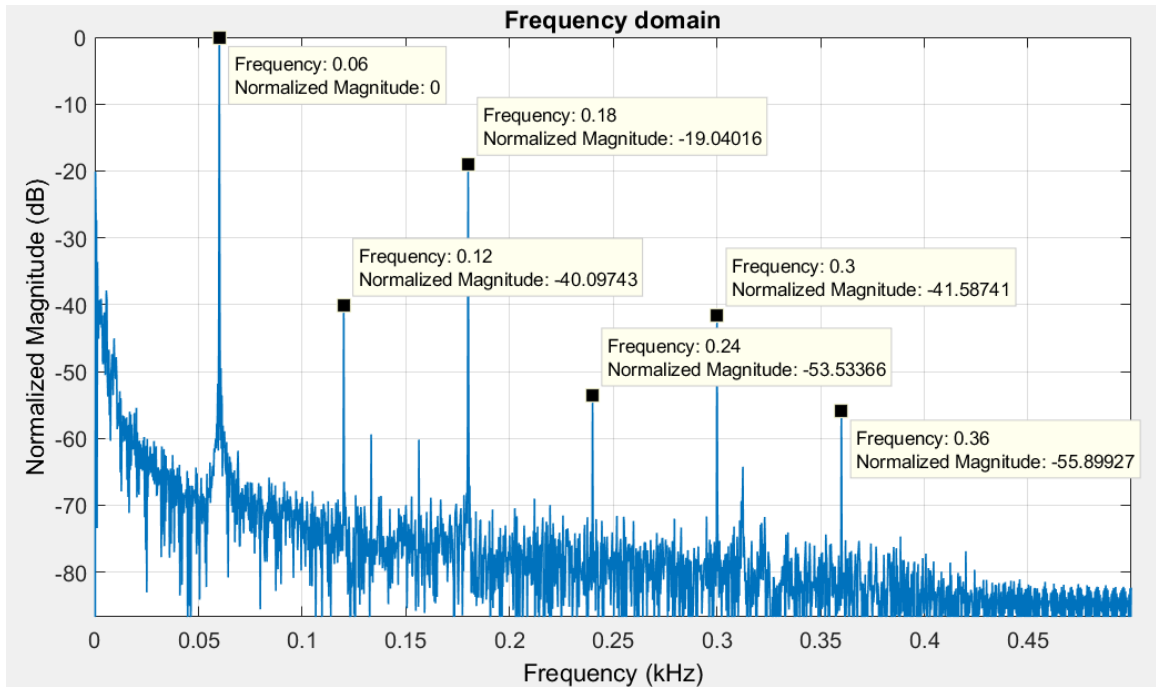
Figure 22. Raw MFAM data frequency content on the ground

MFAM Engine Effect Analysis. An engine proximity analysis was conducted in order to qualitatively determine the best placement of the MFAM on the aircraft. The MFAM was secured in place on the ground under the aircraft with the two sensor heads side by side. The engine was run through a typical throttle profile for a flight in three different positions. The general sequence was: startup, idle, 25 percent throttle taxi, full-throttle takeoff, half-throttle level flight, idle-throttle

73

landing, 25 percent throttle taxi, and finally engine shutoff. The magnetic intensity measurements from sensor 2 were subtracted from sensor 1 to form a gradient measurement. Figure 23 illustrates relative engine proximity next to corresponding time and frequency domain plots of the gradient measurement. A significant magnetic gradient was observed in all three positions, especially at full acceleration. The difference between the two sensors varied by around 10 nT near the tail section, and but varied by almost 70 nT near the front. significant engine disturbance at maximum throttle in all three positions, with most of the power around 300 to 310 Hz. Although placing the sensor heads farther away from the engine should have reduced the interference, there remained throttle-related magnetic disturbances from the engine. Being farther away from the varying magnetic disturbances near the front of the aircraft would allow the engine effects to be captured by the calibration coefficients, or filtered out with a low-pass filter.
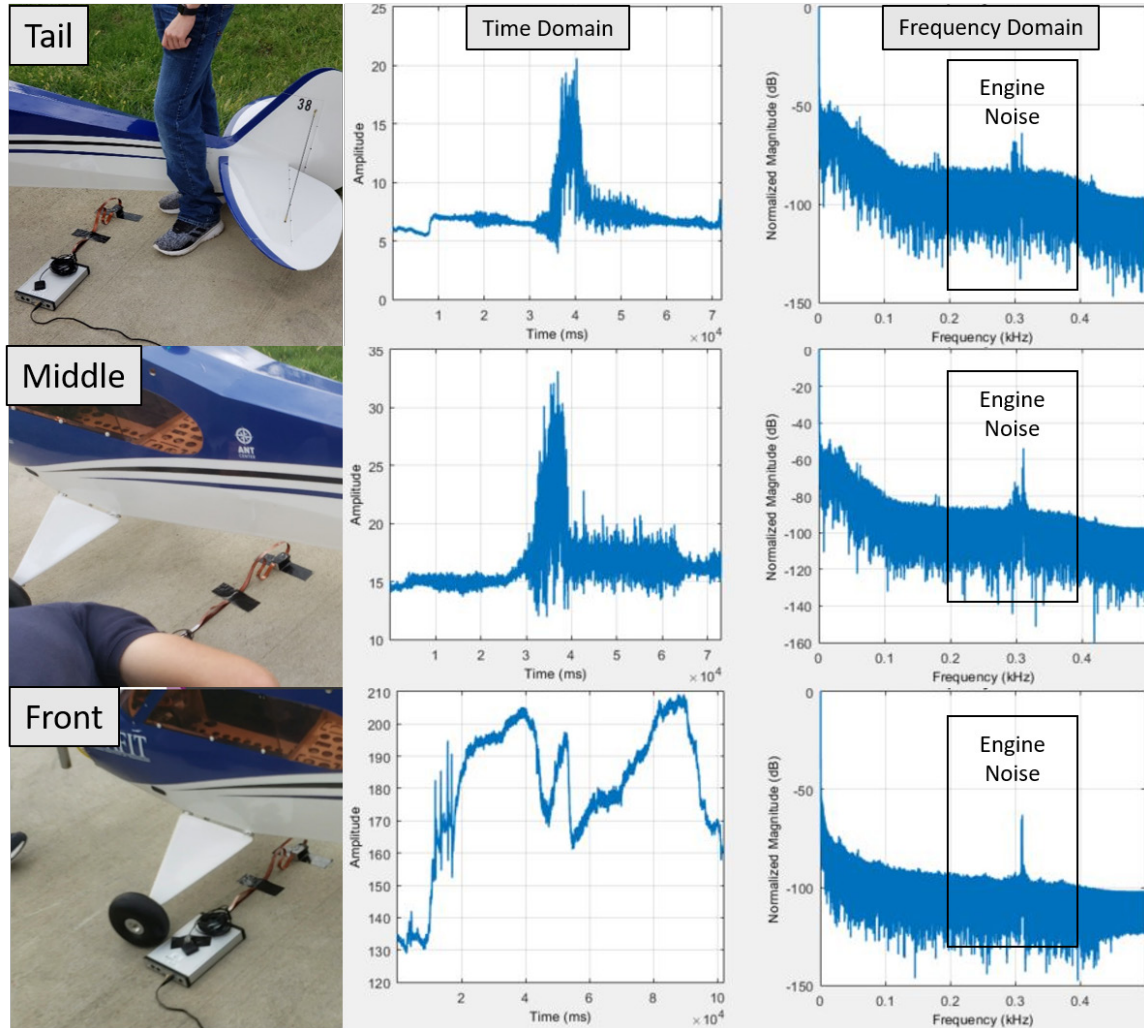
Figure 23. From left to right: Three aircraft positions relative to the two sensor heads. Time and frequency domain of mag1-mag2. The engine proximity analysis identified a significant engine disturbance at maximum throttle in all three positions, with most of the power around 300 Hz.

MFAM Camera Effect Analysis. The MFAM kit was set stationary on a plastic cart. The effects of moving the activated cameras closer to the magnetometers were evaluated. The magnetic measurements and video of the experiment indicated that the human movement caused more of a disturbance than the payload at relevant distances. It was determined that a human body moving in close proximity can measurably perturb the magnetic field and the cameras did not noticeably cause high frequency noise in the magnetic measurements.
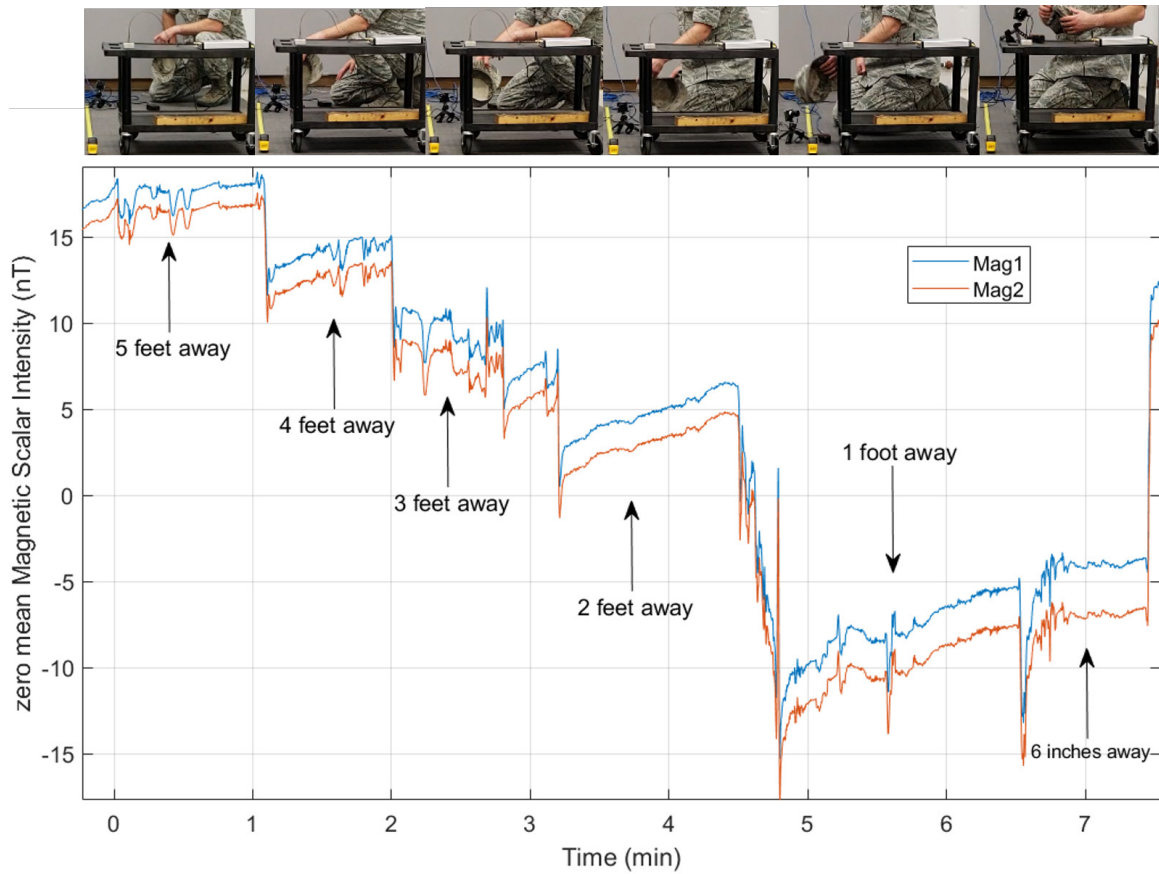
Figure 24. The camera proximity test shows that the person waving a hat in front of the camera caused more magnetic disturbance than the camera shutter.

MFAM Battery and Servo Effect Analysis. The MFAM kit was set stationary to analyze the disturbance from varying the proximity of: two types of batteries (with and without a current-drawing load), a functioning flight control servo, and twisted pair servo wire under load. The battery proximity test determined that the Lithium-Ferrite battery introduced a significantly larger magnetic disturbance than a Lithium-Polymer battery at the same distances 25.
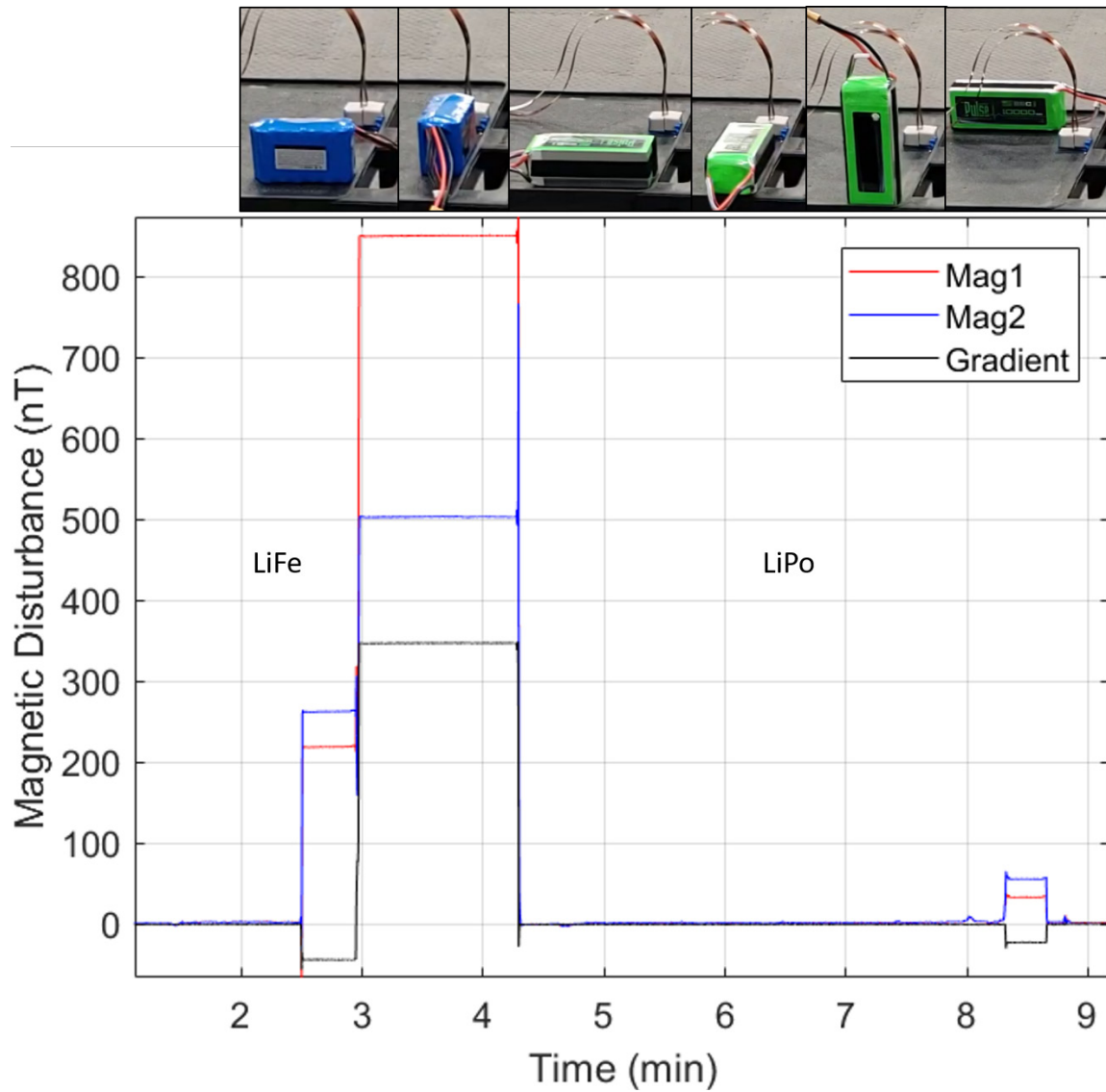
Figure 25. Li-Fe versus Li-Po battery disturbances

The servo proximity test determined that a passive flight servo was disruptive to the magnetometer readings when placed within six inches of the sensor head or ribbon cable as shown in figure 26.
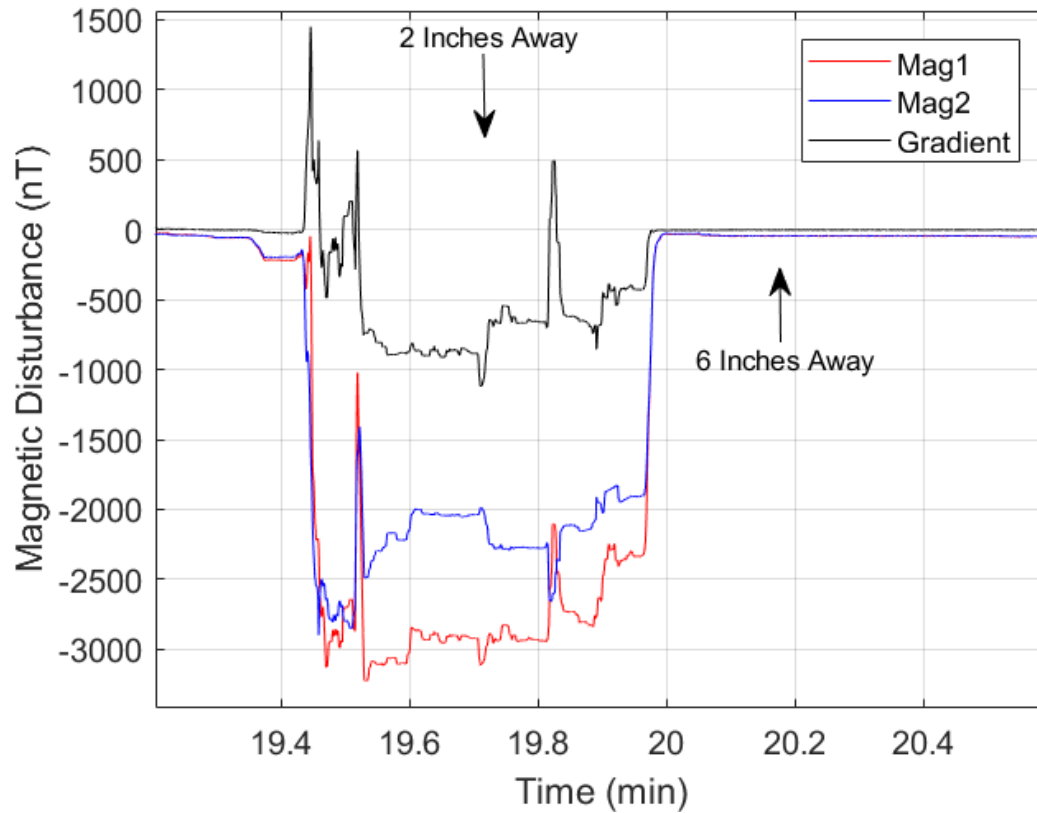
Figure 26. Powered digital servo disturbance comparison at 2 and 6 inches

Actuating the digital servo six inches away from the sensor head produced a measurable digital component to the magnetic field such that changes in the servo were especially notable in the magnetic gradient in figure 27. This test showed how a digital servo could become a significant source of error when actuated or when under load.

78
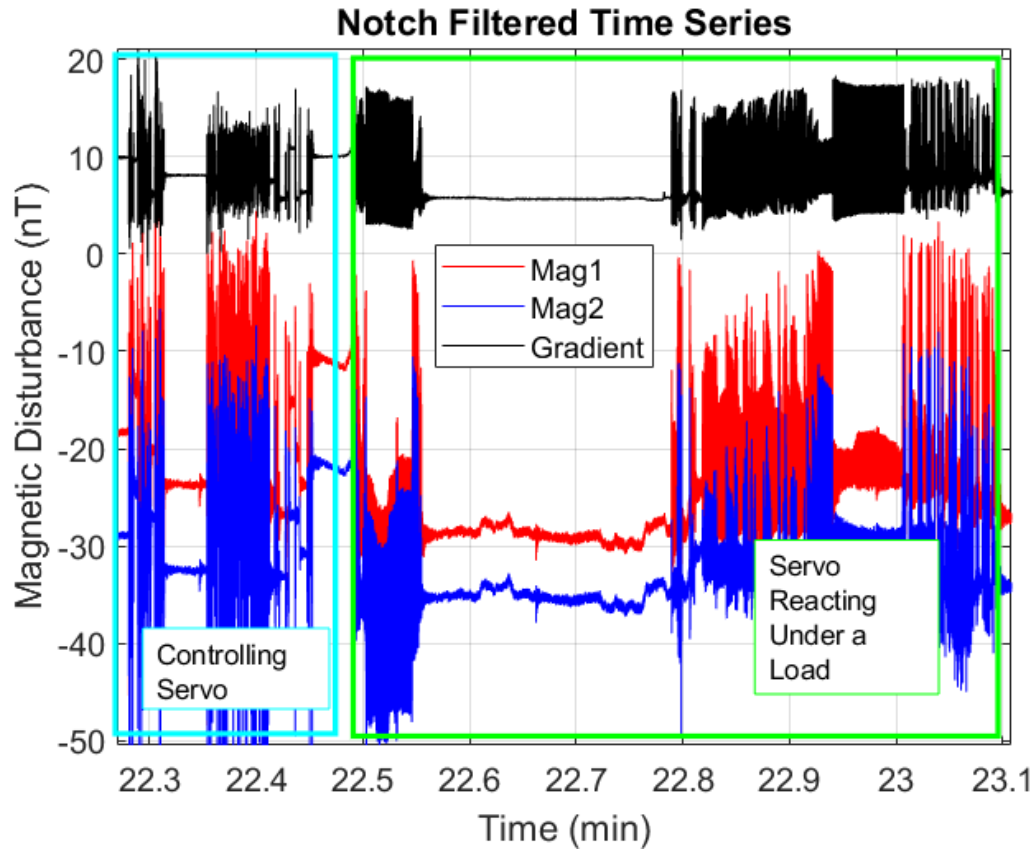
Figure 27. Commanding control versus placing a load on a servo at 6 inches separation

Moving a segment of three twisted servo wires within two inches of the ribbon cable and sensor head caused a minor fluctuation in the magnetic gradient as shown in figure 28. It was determined that servo-wires should be secured away from the sensors, but the disturbance was negligible.
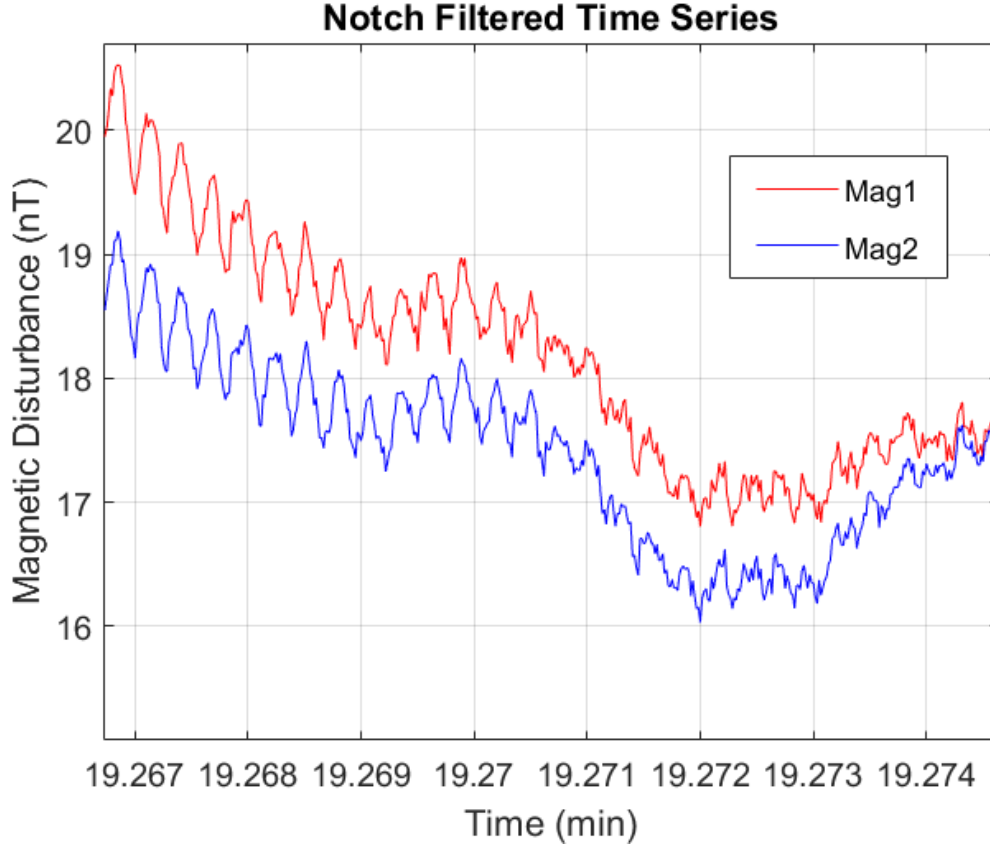
Figure 28. Twisted Servo Wire Disturbance

Dead Zones and Heading Errors. One of the largest challenges in producing high-grade magnetometers is reducing heading-correlated errors. The MFAM scalar magnetometers experience a range of ± 30 nano-Teslas of error outside of their dead zones. The two scalar magnetometers could cancel out heading errors by mounting them opposite each other and averaging the measurements. However, this project intended to correct for heading errors using compass measurements and an aircraft compensation method, and therefore focused on a collection configuration impervious to dead-zones. The one polar dead-zone of each MFAM sensor is approximated as any orientation of the optical axis within $\pm 35°$ of the local magnetic field vector. The two sensor heads were mounted such that their optical axes were perpendicular to each other to ensure that at least one sensor would be out of the dead zone at all

80

times. In this case, the local magnetic field was primarily oriented with the Earth's core field. Using the World Magnetic Model (WMM) to determine the local Earth magnetic field vector, an approximation of the dead zones can be resolved in the local navigation frame as illustrated by figure 29. Future research could use a compass to determine when each magnetometer is oriented in a dead-zone.

(a) (b)
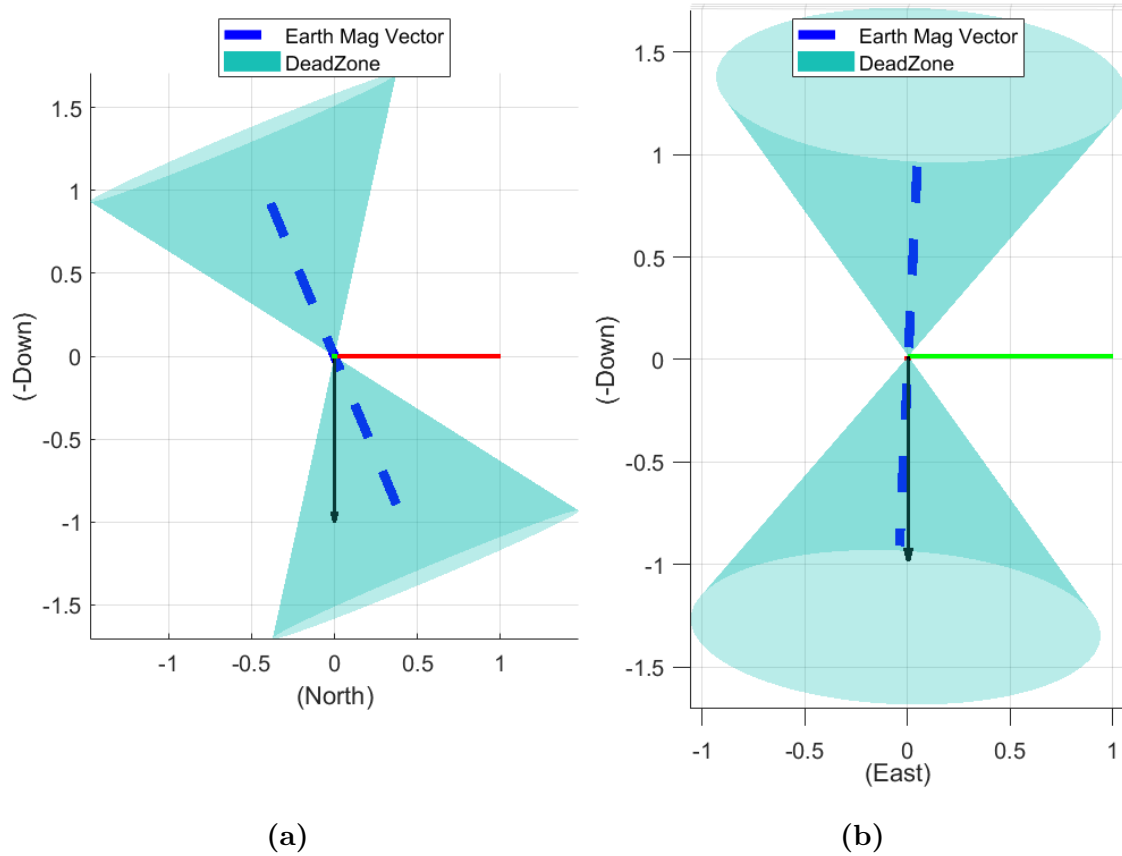
Figure 29. Normalized MFAM polar dead zone for an example earth magnetic vector: red, green, and black arrows correspond to north, east, and down unit vectors. (a) East view, (b) South view

4.3.2.3 Final UAV Configuration.

It was determined from the MFAM proximity analysis that the sensor heads needed to be distanced from any disruptive components on-board the aircraft such as the engine, batteries, wires, servos, and other sensors as summarized in table 6.

The aircraft's frame was primarily made of balsa wood, with a polymer skin which did not interfere with the magnetometer. The MFAM sensor heads were mounted on vibration-dampening foam pads on a wooden mounting plate at an 8 degree pitch such that the optical axes were aligned with the longitudinal and lateral body axes as shown in figure 30. During level flight, the optical axes were parallel to the ground and pointing out the nose/tail and wings. This configuration ensured that at least one sensor's optical axis would be out of a dead-zone at all times and the sensors' optical axes would align with the compass's Cartesian frame.

Table 6. MFAM Proximity Analysis Summary

Error Source	Observation	Lessons Learned
Diurnal Variation	Minimal short-term variation	Ground observation station
Power Grid	Power at 60 Hz harmonics	Notch or low pass filter
Engine	Worst near front	Place sensors far away
Cameras	Camera effects were minimal	Place sensors far away
Batteries	LiFe are worse than LiPos	Prefer LiPo
Servos	Servos are worse under load	Place sensors far away
Twisted Wires	Current carrying wires are bad	Secure wires far away
Dead Zones	Invalid data at some orientations	Mount sensors orthogonally
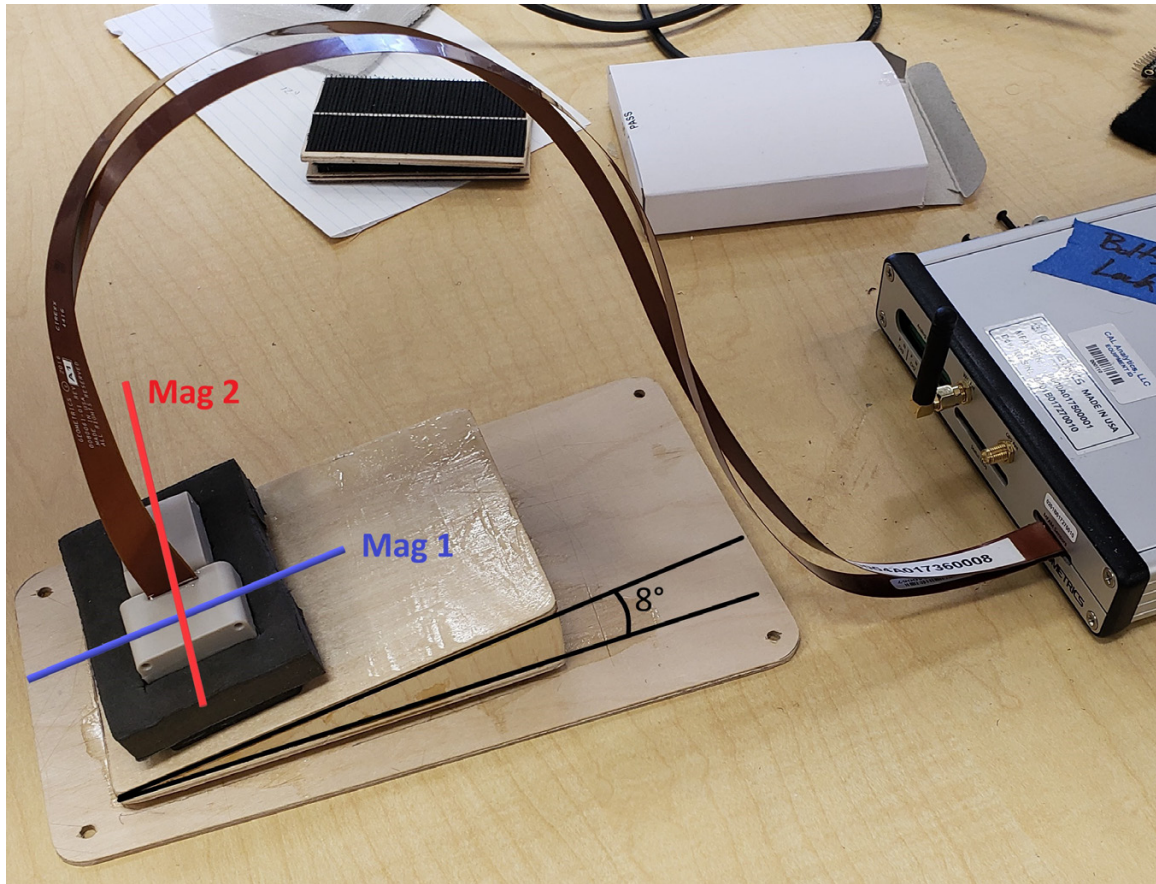
Figure 30. The MFAM sensors aligned with the aircraft body axes

Figure 31 shows the MFAM development kit mounted in the rear of the cockpit, with the ribbon cables extending to the sensor heads fixed on the belly plate. The development kit's aluminum casing was removed to save weight.
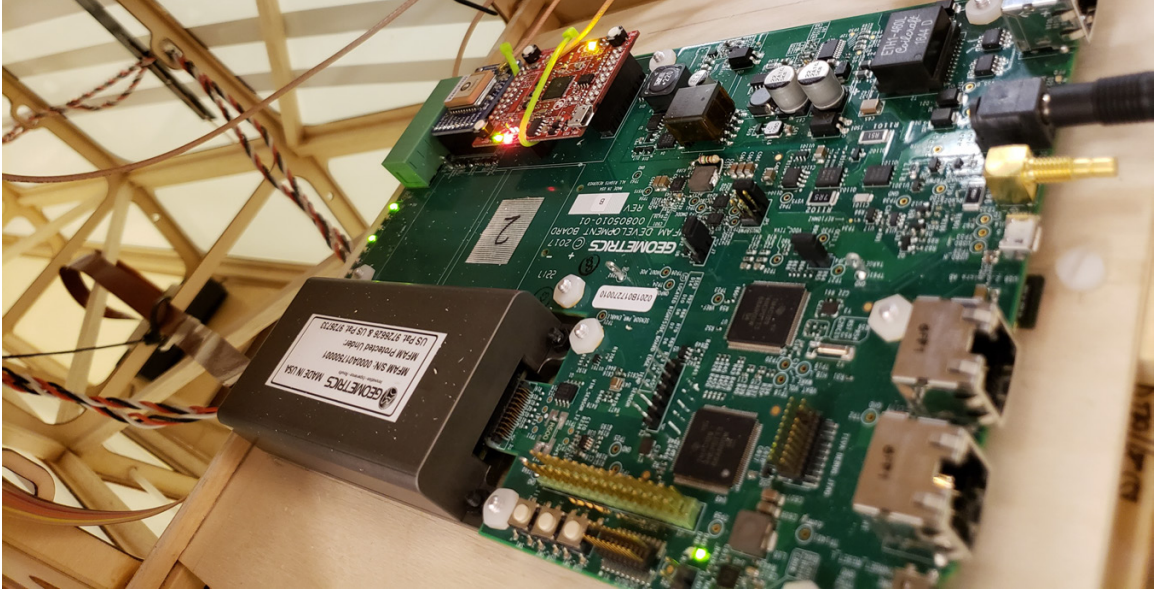
Figure 31. MFAM development kit mounted with the aluminum case removed. The ribbon cables leading to the sensor heads mounted to the belly plate are also visible.

A final subsystem layout is shown in figure 32.
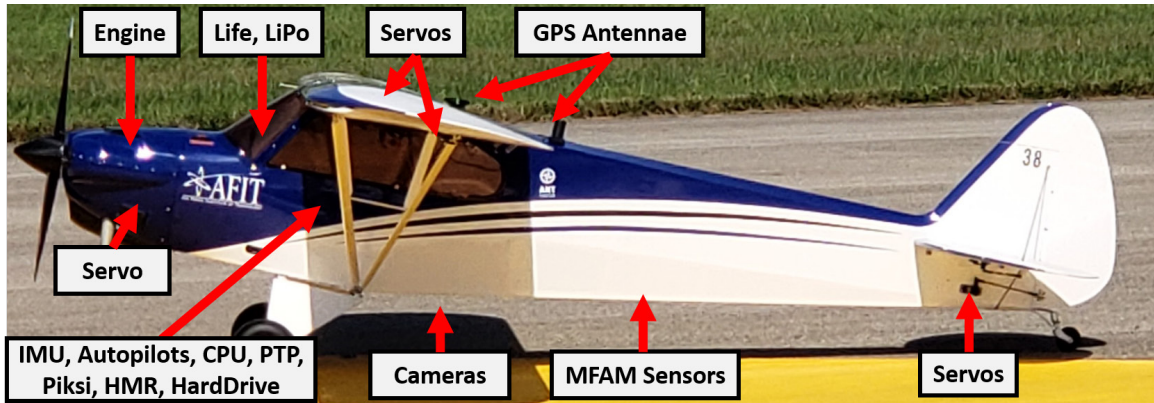
Figure 32. The MFAM sensor heads were separated from sources of magnetic disturbance

4.4 Results

This section presents the approximation of space-weather effects, determining a set of calibration coefficients from raw data, map consistency between subsequent survey flights, and quantifying measurement consistency using a figure of merit calculation.

4.4.1 Approximating Space-Weather Effects.

Attempts to measure locally varying diurnal affects with a base-station magnetometer were unsuccessful. The placement of the ground station magnetometer was likely corrupted by nearby man-made magnetic sources. Instead, magnetic intensity measurements from three observatories for the day of the flight were downloaded from the INTERMAGNET website. The diurnal variations for the day of the flights at Camp Atterbury were approximated by averaging measurements from observatories at similar latitudes in Boulder Colorado (BOU) and Fredricksburg Virgina (FRD). Since the flight durations were tens of minutes, the low frequency diurnal variation was only 1 nano-Tesla as shown in figure 33a. The raw measurements for only the gridded 100 meter flight were adjusted according to the diurnal trend at the corresponding time of day for to better isolate and solve for the aircraft disturbance field parameters.
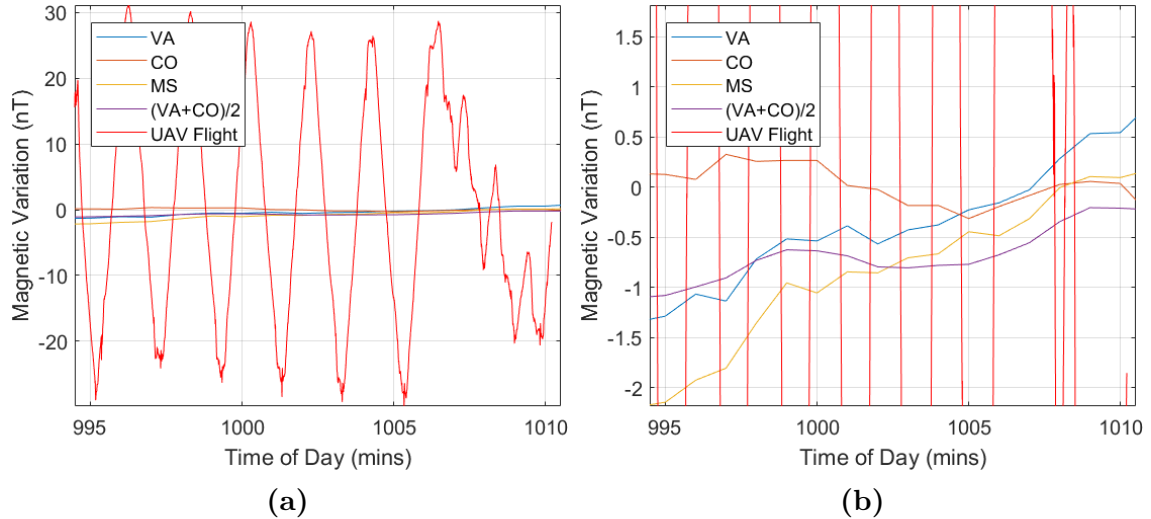
Figure 33. A ground observation magnetometer required the use of national observatory data. (a) Measurements from INTERMAGNET magnetic observatories in Boulder Colorado (BOU) and Fredricksburg Virginia (FRD) were averaged to give a rough diurnal trend for the gridded flight used to determine the aircraft characterization coefficients. (b) A zoomed-in view of the observatory data shows the diurnal variation of around 1 nT over the whole flight

85

4.4.2 Determining Coefficients With Real Data.

A calibration dataset was collected using a gridded trajectory at 100 meters AGL with approximately 50 meter vertical line spacing and 160 meter horizontal tie-line midsection spacing as seen in figure 34a. The colors in figure 34a reflect the zero-mean uncompensated magnetic intensity measurements. The gridded trajectory was used to characterize a set of aircraft coefficients θ by solving

$$\underset{\eta}{argmin}(\triangle \eta - (\mathbf{B_s} - mean(\mathbf{B_s}))) \tag{64}$$

and then dropping e_1 and e_2 from the vector η. The disturbance field model components are shown in figure 53b. The planar disturbance field was probably more significant than the eddy currents since the aircraft construction was primarily balsa-wood and plastic.

(a) Raw Measurements (zero mean)

(b) Disturbance Components

(c) Disturbance Model

(d) MTLL-Calibrated (zero-mean)
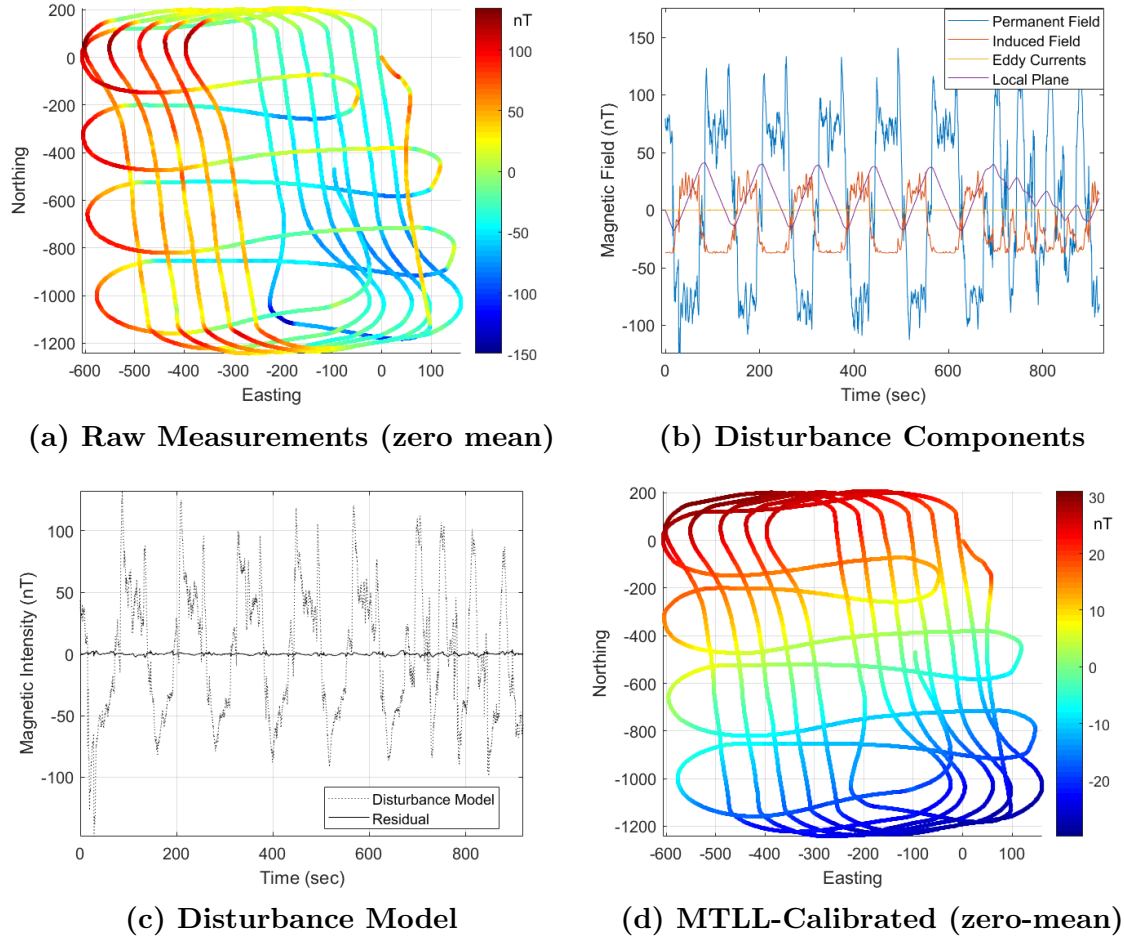
Figure 34. Using the gridded trajectory measurements provided self-consistent calibration coefficients. (a) Gridded survey trajectory at 100m AGL with 50 and 160 meter horizontal and vertical line spacing. (b) The disturbance model components. (c) Predicted magnetic field and 1Hz low-passed residual from actual measurements. (d) Magnetic measurements with aircraft effects removed

4.4.2.1   Evaluating the Disturbance Field Model.

The total disturbance field model including the spatial variation and diurnal variation was removed from the raw measurements $B_s - \triangle\eta$ to form a residual. The distribution of this residual is well modeled as a Gaussian distribution $\mathcal{N}(0, 3\ nT)$. This appears characteristic of white Gaussian noise. Frequency analysis of the residual illuminated distinctive high-frequency components as seen in figure 35c. These were likely from sensor noise, or locally-propagating magnetic fields from nearby elec-

tronics. A 60 Hz saw-tooth component of the raw magnetic signal explained the multiples of 60 Hz in the power spectral band. These periodic noise terms lay outside the magnetic anomaly field bandwidth, suggesting they could be filtered out using a low-pass filter.

4.4.2.2 Applying a 1 Hz Low Pass Filter.

The spatial frequency content of Earth's crustal anomaly field is very low. According to aerial magnetic surveying practices [79], the shortest expected wavelength of the crustal magnetic anomaly field in the measurements can be approximated as the following relationship between aircraft height AGL and velocity

$$F_{time}^{max} < \frac{1}{h}V_{ac}, \tag{65}$$

where F_{time}^{max} is the highest time-frequency content of the anomaly field within magnetic measurements taken from a vehicle moving at a velocity of V_{ac} at a height h above the ground. This UAV flew at a maximum velocity of around 23 meters per second, which means the highest frequency content would be 0.23 Hz. The corrected magnetic measurements were passed through a 1 Hz low-pass Butterworth filter to isolate the Earth's magnetic field from high frequency aircraft and sensor noises. The filtered magnetic measurements are shown in figure 34d. The remaining residual after filtering is within the expected errors from the approximation of short-term space weather effects. Any remaining heading error is likely limited by the resolution of the vector magnetometer, or un-modeled aircraft effects like servo actuation or low-frequency engine disturbances.
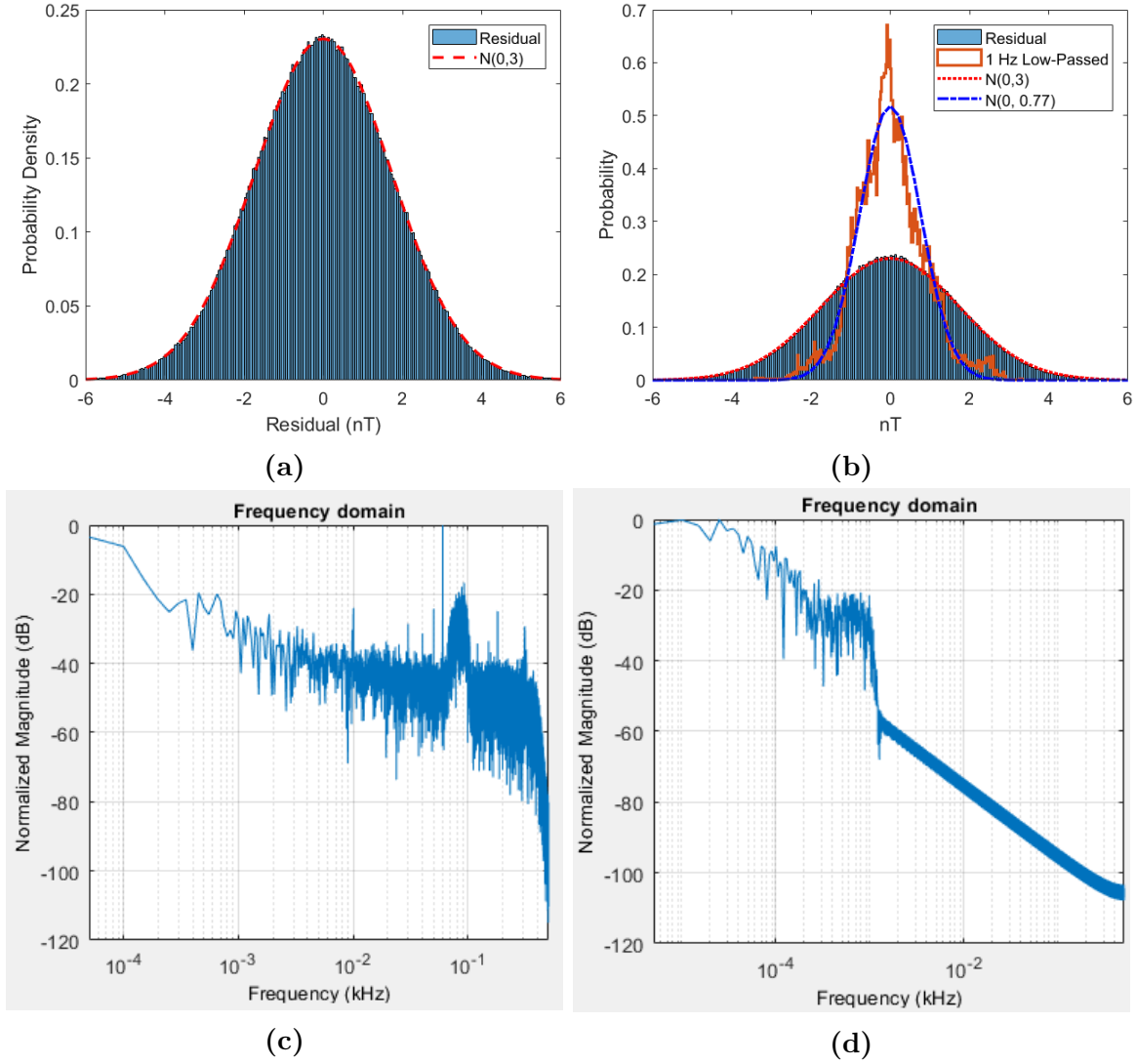
Figure 35. The residual difference between the disturbance model and raw measurements is dominated by white gaussian noise at high frequencies. (a) Residual histogram suggests white Gaussian noise with a variance of 3 nano-Tesla. (b) 1Hz Low-passed compensation residual removed high frequency contributions which appear Gaussian. (c) Frequency domain of unfiltered residual shows distinctive structured noises outside the expected bandwidth of the anomaly field. (d) Frequency response of 1 Hz low-passed data demonstrated the resulting residual is of the magnitude of space-weather effects.

4.4.3 UAV Magnetic Surveying Flights.

We performed a single calibration flight and used its calibration coefficients to correct a series of subsequent flights. Below we show the magnetic maps for all

flights. We would expect the corrected measurements to be spatially consistent. Each pattern in figure 36 overlays the same satellite image of Himsel Army Airfield (HAAF). The colors of the trajectories are the magnetic intensity measurements corrected for aircraft affects with relative biases removed to better illustrate the local magnetic field. Indeed, the values of the measurements are similar between line crossings, regardless of the aircraft direction as shown in figure 36.

Diurnal measurements from the GEM sensor ground station were unusable due to a local industrial magnetic disturbance drowning out the space-weather affects. Although this leaves a slowly varying offset between flights conducted at different times, each flight was short enough to provide relatively time-invariant magnetic measurements.

The first flight, shown in 36a, was an attempt at a high altitude calibration flight. The aircraft was recovered before the flight profile was complete due to high winds in excess of a safety threshold which were causing the aircraft to drift north. Nonetheless, valid magnetic intensity measurements were collected and presented.

The second flight resulted in a successful calibration flight pattern at 450 meters altitude 36b. The aircraft then surveyed the area at 400 meters AGL 36c. A necessary aircraft configuration change after this flight made the coefficients only valid for the preceding flights.

The third flight was a gridded survey at an altitude of 100 meters AGL with an approximate horizontal line spacing of 50 meters with a tie line spacing of roughly 150 meters. Future gridded surveys would benefit from longer overshoot and lead-in grid line distances, as well as alternating tie-line approaches like how the main grid lines were flown instead of a sequential tie-line flight pattern. The aircraft could not turn sharp enough to fly parallel tie lines as seen in the trajectory in figure 36d.

The fourth flight began with a gridded survey at 250 meters AGL as shown in

36f. This was immediately followed by a drifting figure-eight style flight pattern at 100 meters AGL to simulate an un-aided loitering UAV attempting an altitude hold pattern 36e.

It is observable that the gradient of the magnetic field was the same between the common areas of 36d and 36e. Notably, some anomalies were observable at 100 meters AGL which related to the location of structures East of the runway. These anomalies were only observable at low altitudes as the higher frequency components were lost in the upward continuation of the anomaly field. These anomalies were also consistent between the gridded and figure-eight trajectories. Otherwise, the main variation in the field was planar towards magnetic north with a slope of around 1 nano-Tesla per 22 meters.
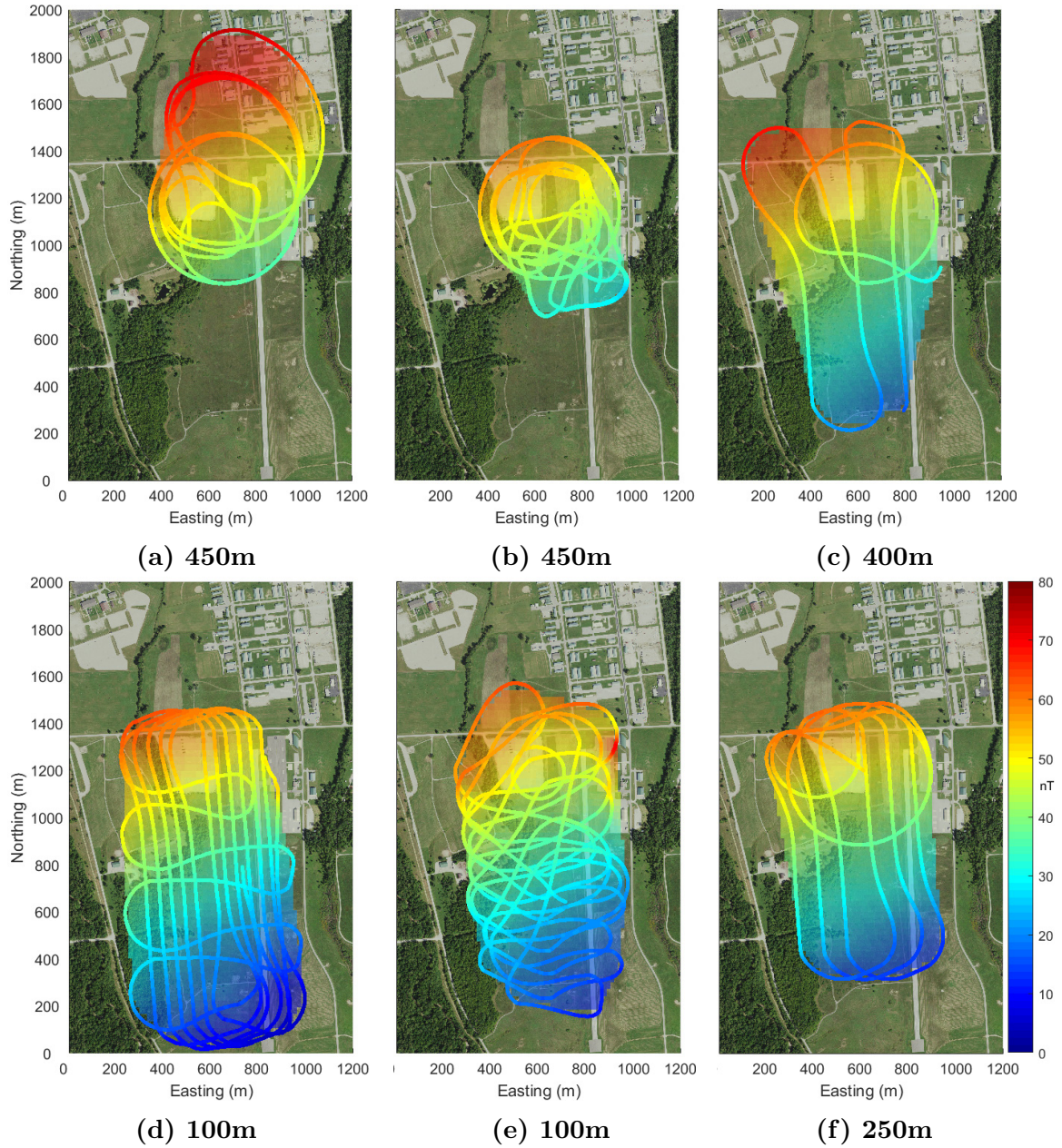
Figure 36. UAV flights and relative magnetic intensity maps corrected for aircraft effects and biases. (a) First calibration flight attempt in strong winds at 450m AGL. (b) Successful calibration flight at 450m AGL: two squares in opposing directions, and a cloverleaf. (c) Gridded flight at 400m AGL. (d) Gridded flight at 100m AGL. (e) SLAM flight pattern at 100m AGL. (f) Gridded flight at 250m AGL.

4.4.4 Self-Consistent Magnetic Intensity Measurement Analysis.

A figure of merit (FOM) is a metric to evaluate the self-consistency of scalar magnetic measurements at path intersections. We define FOM for this analysis in units of nano-Teslas as

$$FOM = \sqrt{\frac{\sum_{\{x,x^*\}}^{N} (z - z^*)^2}{N}} \tag{66}$$

where x and x^* are any two points in the flight within 1 meter of each other, disregarding points within 1 second. z and z^* are the corresponding magnetic intensity measurements to points x and x^*, and N is the number of point pairs. Figures 37 and 38 illustrate the calibration corrections made for each flight pattern and determining the FOM. Pairs of black circles indicate non-sequential measurement pairs within 1 meter of each other: x and x^*. Black lines indicate the difference between paired measurements $z - z^*$.
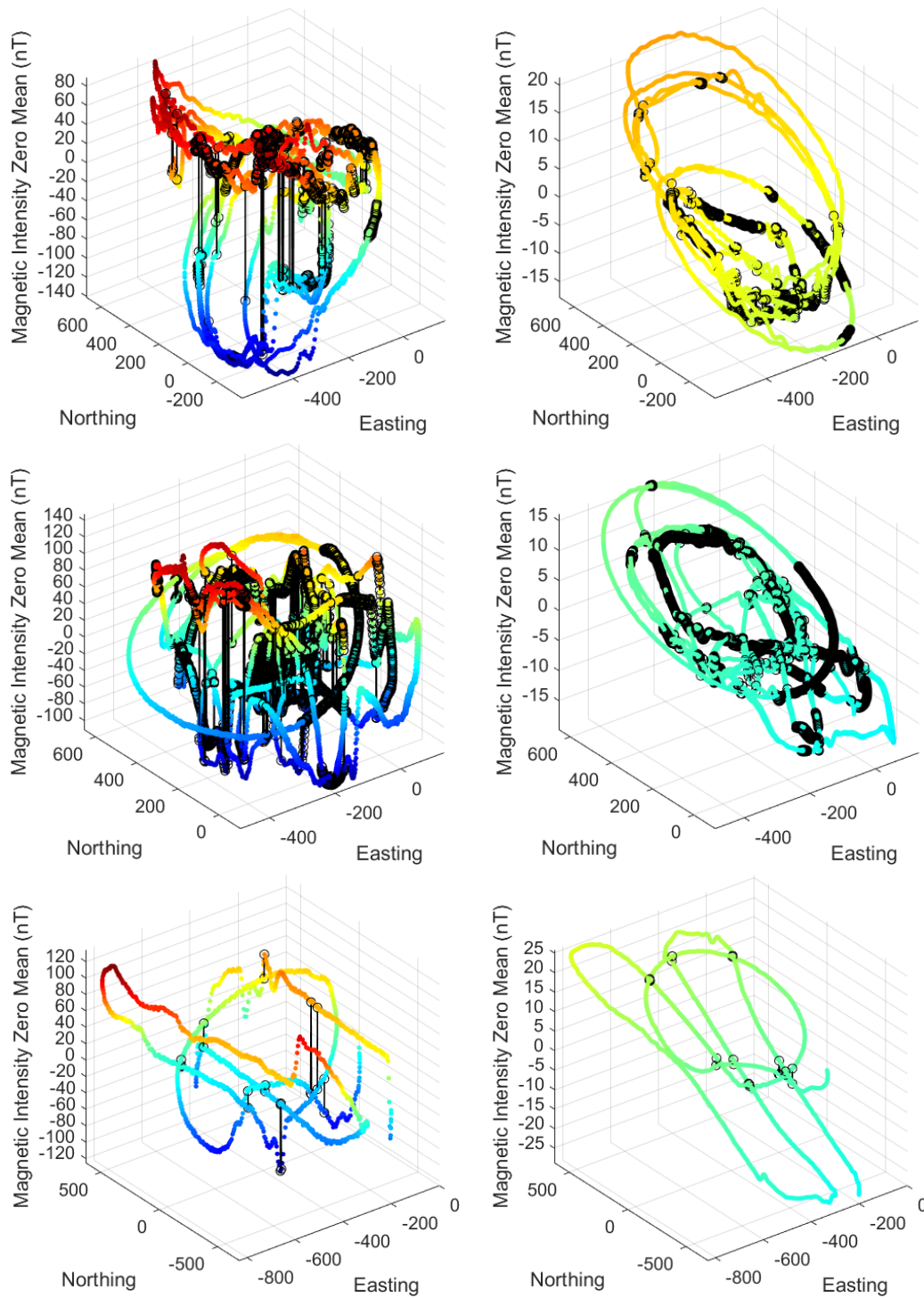
Figure 37. Determining figure of merit before (left) and after (right) aircraft compensation. Pairs of black circles indicate non-sequential measurement pairs within 1 meter of each other, black lines indicate the difference between paired measurements. (Top) First 450m AGL calibration flight attempt in strong winds. (Middle) Successful 450m AGL calibration flight: two squares in opposing directions, and a cloverleaf. (Bottom) 400m AGL grid.

94
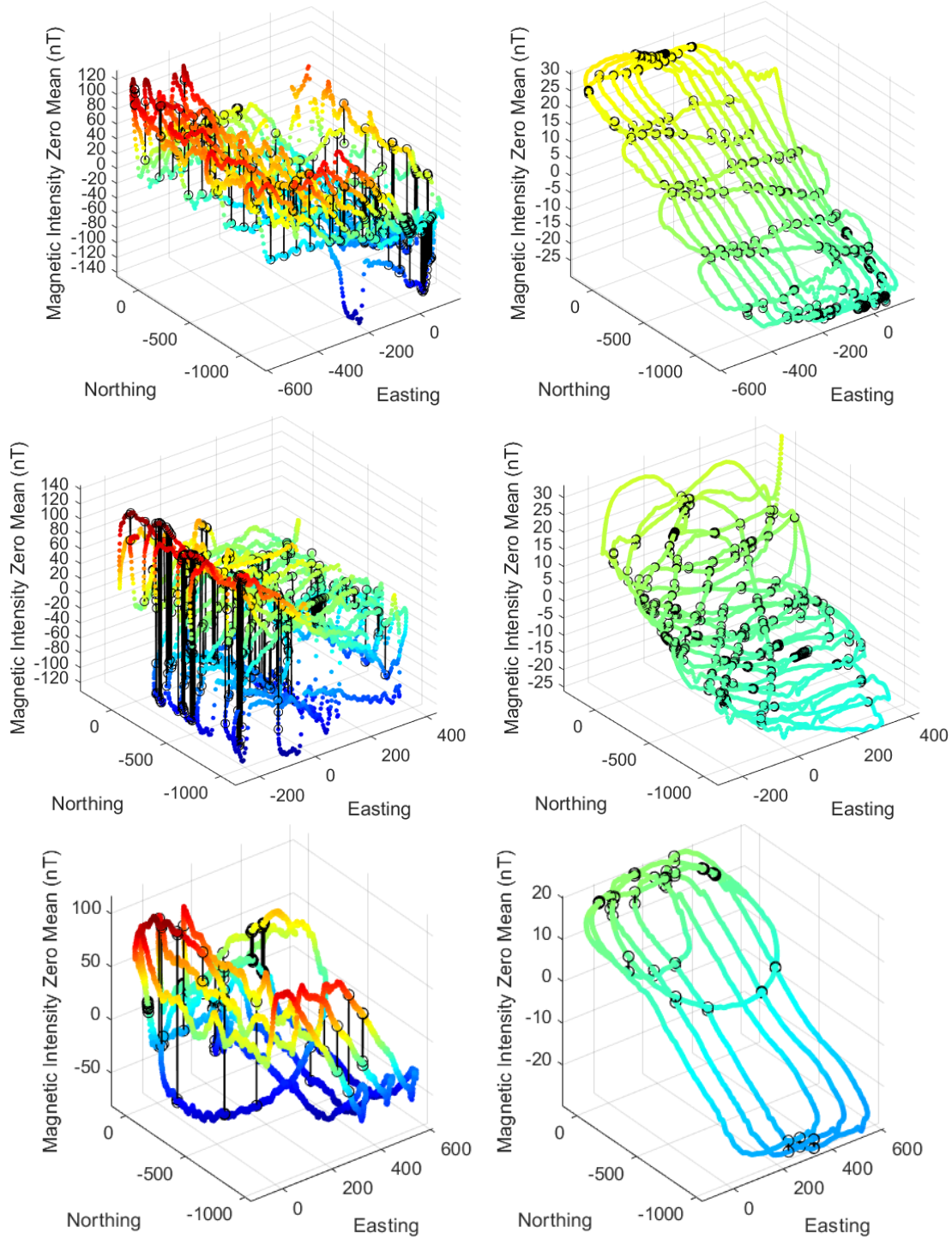
Figure 38. Determining figure of merit before (left) and after (right) aircraft compensation. Pairs of black circles indicate non-sequential measurement pairs within 1 meter of each other, black lines indicate the difference between paired measurements. (Top) 100m grid. (Middle) 100m SLAM flight. (Bottom) 250m grid.

Table 7 shows the reduction in FOM from uncompensated measurements to measurements with just at the aircraft disturbance model removed. The table also indicates the source of each flights calibration coefficients. Of note is how two different aircraft configurations were characterized on two flights with different sets of coefficients, which were used to remove aircraft effects on four other flights with a FOM of less than 2 nano-Teslas.

Table 7. Aircraft Coefficients Reducing Measurement Inconsistency

Flight	Raw FOM (nT)	Calibrated FOM (nT)	N	Cal Flight
(a)	31.52	1.26	533	(b)
(b)	33.97	0.56	3272	(b)
(c)	67.23	1.9	13	(b)
(d)	63.44	0.92	297	(d)
(e)	93.65	1.08	376	(d)
(f)	60.52	1.42	50	(d)

4.5 Conclusion

This research sought to build and fly a low-cost magnetic surveying UAV from COTS components to magnetic navigation standards. A 40% scale Carbon Cub model aircraft was deliberately configured with an autopilot, magnetometer, and combustion for magnetic surveying. Calibration flights characterized the aircraft disturbance field within 2 nano-Teslas. The model was used to provide spatially consistent measurements on separate flights. This platform demonstrated the viability of collecting precise magnetic intensity measurements on a UAV, which enabled further research into small unmanned aerial systems (sUAS) navigation using magnetic measurements.

4.6 Acknowledgments

V. Flight Test Results for a Magnetic Anomaly SLAM System

5.1 Abstract

Earth's magnetic anomaly field has been used for aerial navigation. The miniaturization of atomic magnetometers enables the extension of magnetic navigation to small UAVs. Map-based magnetic navigation methods are impractical with small UAVs due to the lack of high-resolution magnetic maps at low-altitudes. Aerial magnetic Simultaneous localization and mapping (SLAM) techniques have been used to remove the dependency on map quality and availability. This paper presents an implementation of a magnetic SLAM filter to constrain three different grades of simulated INS solutions to tens of meters over a 14-minute UAV flight using real magnetic intensity measurements without a prior magnetic map. The combination of low-cost miniaturized atomic magnetometers and SLAM methods enabled magnetic navigation on small UAVs without a map as a globally available and stealthy GPS-denied navigation method.

5.2 Introduction

Recent advances in manufacturing technology has reduced the size and power requirement of atomic magnetometers by orders of magnitude while maintaining measurement precision. This reduction in sensor footprint, cost, and power requirements reduces the size requirements of magnetic surveying vehicles as well as broadens the commercial uses of atomic magnetometers. The comparison of two Geometrics atomic magnetometers in table 8 shows the reduction in SWAP between an optically pumped cesium scalar magnetometer (G-823A), and self-oscillating MFAM. The MFAM requires significantly less SWAP without suffering in precision. Although the

98

miniaturized sensors only have one dead zone, heading errors and dead-zone size are significantly larger than the G-823-A. To combat this trade-off, combining measurements from two sensor heads can either reduce heading errors or eliminate dead-zones, depending on the sensor configuration. Figure 39 illustrates the recent reduction in scalar magnetometer manufacturing [3].

Figure 39. Geometrics MFAM [3]

Table 8. Magnetometer Comparison

Magnetometer	G-823A	MFAM
Size	41259 cc	15 cc
Weight	450 g	30 g
Power	12-16 W	2 W
Sensitivity	$4\ pT/\sqrt{Hz}$	$1\ pT/\sqrt{Hz}$
Heading Error	$\pm 0.15\ nT$	$\pm 30\ nT$
Dead Zones	(2) Equilateral, Polar, 10 °	(1) Polar, 35 °

5.2.1 Magnetic Maps.

The Earth's outer core produces a magnetic field which is then perturbed by magnetically susceptible materials in the Earth's crust. The resulting deviation from a core field reference model is a world-wide magnetic anomaly field which is stable over time and can be used as a navigation signal. Earth's magnetic anomaly field varies both horizontally and vertically. The spatial variation of the anomaly field increases as altitude decreases, and therefore cannot be mapped from space. High-resolution maps are therefore created with aircraft, where the expense scales with the length of the survey flight. Geomagnetic surveying aircraft use scalar magnetometers and gridded survey patterns to create maps of the Earth's magnetic anomaly field for geological analysis of the Earth's crust. These maps can be used for mineral and petroleum exploration, locating orphaned oil wells [82], and characterizing fault zones [83]. Magnetic anomaly maps have also been used for aerial and marine navigation [4, 24, 32]. There are two sources of magnetic maps. Individual surveys cover small areas at a single altitude. Compilation products fuse many individual surveys into larger map products. The North American Magnetic Anomaly Database (NAMAD) is built by fusing thousands of individual surveys of varying quality and incorporating satellite and ground observations to resolve long magnetic field wavelengths.

5.2.1.1 Map Sampling.

A fully sampled magnetic map satisfies the Nyquist criteria to capture all frequency components of the magnetic field's spatial variation with the proper spacing of magnetic measurements. Survey grid lines must be closer at lower altitudes in order to fully sample the magnetic field, which makes survey flights longer and more expensive. In general, the spacing of survey grid lines must be at most the survey height [79]. Figure 40 illustrates two individual surveys on the left. Survey (B) is

fully sampled at 100 meters altitude with 100 meter line spacing. Survey (A) is under-sampled at 300 meters altitude with 500 meter spacing.

5.2.1.2 Map Continuation.

Potential fields can be modeled as a function of distance through a mathematical transformation called continuation. Assuming magnetic sources are below a survey map of infinite size, a magnetic anomaly map can be upward-continued to higher altitudes, but cannot be accurately downward-continued very far. This prevents magnetic navigation at altitudes lower than the survey map. In the maps to the left of figure 40, (A) can be modeled as the upward continuation of (B), but (B) cannot be sufficiently modeled as the downward continuation from (A), even if (A) was fully sampled [79].

5.2.1.3 Map Unavailability.

The World Digital Magnetic Anomaly Map (WDMAM) [80] on the right of figure 40 highlights a few of the many un-surveyed regions of the world as uncolored sections of the map. The colored sections of the WDMAM still contain errors from fusing under-sampled individual maps.
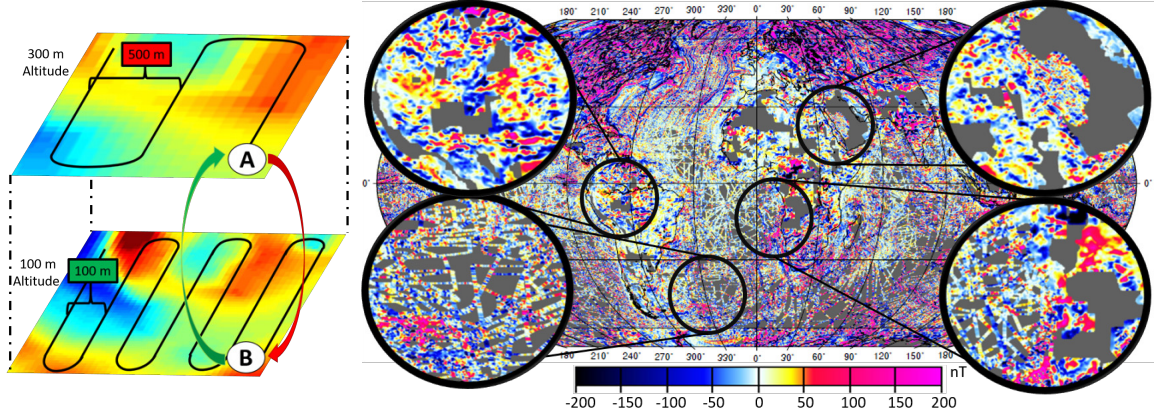
Figure 40. Two individual surveys are illustrated on the left: (B) fully sampled at 100 meters altitude and (A) undersampled at 300 meters altitude. (B) Can be upward-continued to (A), but (A) cannot be downward-continued to (B). The World Digital Magnetic Anomaly Map on the right highlights a few of the many vast un-surveyed regions of the world [80].

5.2.2 Map-Based Aerial Magnetic Navigation.

Aerial magnetic navigation matches sequences of magnetic intensity measurements to prior-surveyed magnetic anomaly maps as a globally-available gps-alternative to INS aiding [4]. More spatial variation in the magnetic anomaly fields at lower altitudes increases the navigation potential in magnetic navigation. However, navigation-quality maps are often unavailable at the desired resolution or height for low-altitude aerial magnetic navigation. Un-surveyed regions, under-sampled surveys, and downward continuation instability are major obstructions to a world-wide magnetic anomaly map for navigation [25].

5.2.3 Magnetic Simultaneous Localization and Mapping.

Magnetic SLAM approaches have been used in robotics and smart-phones with vector magnetometers and man-made magnetic anomalies without maps of the magnetic environment [58, 55, 59]. This method requires a trajectory that is guaranteed to overlap over time and revisit areas with a stable but spatially variant magnetic

anomaly field. Lee and Canciani [96] first extended magnetic SLAM to a full-sized aircraft using an atomic scalar magnetometer and navigation-grade INS. Figure 41a illustrates an INS trajectory estimate with position errors (left) and a SLAM correction (right) which share the same set of magnetic intensity measurements (colors). Contrasting the trajectories illustrates how incorrect path estimates result in inconsistent magnetic intensity measurements at path intersections. Magnetic SLAM can correct INS drifting position errors by minimizing magnetic measurement inconsistencies at line crossings.

5.2.4   Configuring a UAV for Magnetic Navigation.

Magnetic surveys conducted with UAVs for the purpose of generating magnetic maps include extensive data processing after the flight [79]. Aircraft disturbances are first minimized by placing magnetic sensors far from magnetically susceptible vehicle components, and then removed from survey data using post-processing methods. Magnetic disturbances must be estimated and removed from magnetic measurements during flight in order to conduct aerial magnetic navigation with a UAV. We previously configured, calibrated, and flew a UAV capable of compensating magnetic intensity measurements during flight within 2 nano-Teslas [97]. This aircraft flew a wandering figure-eight style pattern to represent a UAV in an altitude holding pattern with a drifting position estimate. Figure 41b shows the flight pattern of the UAV whose color corresponds to the compensated zero-mean magnetic intensity measurements.

(a) INS trajectory → SLAM solution

(b) Real UAV trajectory and magnetic intensity measurements
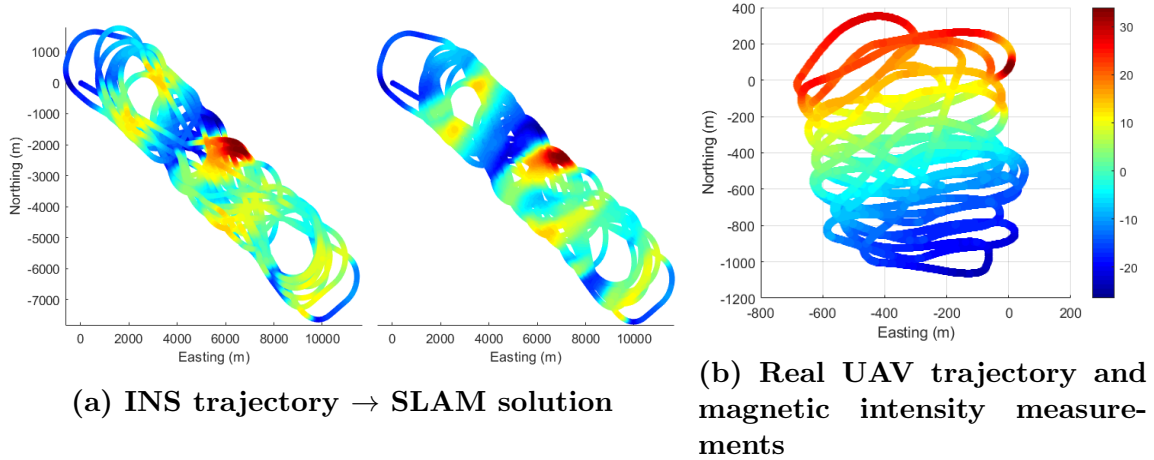
Figure 41. **Extending previous work to UAV MagSLAM. (a) The demonstration of magnetic SLAM on a loitering aircraft illustrates how correcting measurement inconsistencies also correct position errors. (b) The collection of spatially consistent magnetic measurements from a UAV motivated an evaluation of MagSLAM on a UAV**

The combination of a magnetic navigation method which does not require prior maps and a viable UAV magnetic intensity dataset sets the stage for low-altitude UAV magnetic SLAM. This paper demonstrates SLAM on a sUAS scale with roughly one-tenth the flight area of the previous full-scale survey aircraft [96]. Three INSs grades were simulated to demonstrate the capabilities of magnetic SLAM on a UAV with real magnetic intensity measurements and a practically-sized INS. The contributions of this research include discriminatory resampling of subsets of revisiting particle paths *and* weights, in addition to incorporating covariance information from Gaussian process regression (GPR) into a Gaussian residual weighting function.

5.3   Methodology

In this section we present the real UAV measurements and trajectory, generation of realistic INS errors, and the aerial-inertial magnetic SLAM algorithm.

5.3.0.1 Magnetic Intensity Measurements.

An Aeroworks 40% scale Carbon-Cub UAV made of wood, plastic, carbon fiber, aluminum was used as the main air-frame. A Geometrics MFAM collected magnetic intensity measurements and compass measurements used for calibration. Magnetic intensity measurements were spatially consistent within two nano-Teslas after compensating for aircraft effects. The process to isolate and remove aircraft magnetic disturbances was covered in [97].

5.3.0.2 Truth Trajectory.

A true UAV location was provided by a post-processed differential-GPS solution from a Piksi GNSS with a reference receiver on the ground. The Piksi truth data was corrupted with simulated INS errors, and the ability of the SLAM system to identify and correct the INS errors determined the system's performance.

5.3.1 Inertial Navigation System Error Simulation.

Inertial navigation systems combine sensed acceleration and angular rates of change to determine specific forces in a navigation frame of reference. These corrected forces are integrated to produce position updates over time. All un-aided inertial systems have long term drifting position errors as a result of the repetitive integration of tiny accelerometer and gyroscope noises over time. The classification of INS grades is subjective to the application of their intended use. For guidance purposes, they can be generally classified into five grades: space, marine, navigation, tactical, and commercial. Honeywell's HG9900 and HG1700 inertial systems are examples navigation and tactical grade INSs respectively. These are common grades used in aircraft navigation because of their quality with respect to size and an aircraft's typical flight duration. Commercial grade IMUs are often used for attitude and heading refer-

ence system (AHRS) references but are typically too noisy to determine position over time. This section describes the effective differences between navigation, tactical, and commercial grade INSs by comparing their noise terms and resulting drift rates.

5.3.1.1 Characterizing Different Grades of INSs.

Simulated trajectory estimates from navigation, tactical, and commercial grade INS systems were generated to analyze the ability of magnetic SLAM to correct for INS errors. A 15 state Pinson error model from Titterton and Weston [9] was used to generate realizations of realistic INS errors by using real INS noise terms seen in table 9. The contrasting noise strengths come from grades of manufacturing and calibration. The difference is orders of magnitude in position drift.

Table 9. INS Simulation Terms

Terms	Navigation HG9900	Tactical HG1700	Commercial
Vel Rand Walk σ_{VRW} $(m/s^{\frac{3}{2}})$	1e-12	0.003302	0.0043
Accel Bias σ_A (m/s^2)	2.4525e-04	9.81e-3	0.1960
Accel Bias τ_A (s)	3600	3600	3600
Ang Rand Walk σ_{ARW} $(m/s^{\frac{3}{2}})$	5.8178e-07	3.6361e-05	6.5e-04
Gyro Bias σ_G (m/s^2)	1.4544e-08	4.8481e-06	0.0087
Gyro Bias τ_G (s)	3600	3600	3600

5.3.1.2 15 State Pinson INS Error Model.

The 15 state Pinson INS error model's states are:

$$\mathbf{x}_{15\times1} = \begin{bmatrix} \delta\mathbf{p} & \delta\mathbf{v} & \delta\epsilon & \mathbf{b_a} & \mathbf{b_g} \end{bmatrix}^T \tag{67}$$

which correspond to position, velocity, tilt, accelerometer, and gyroscope errors respectively in three-dimensional space. The model also generates a linearized dynamics matrix $\mathbf{F}$ from an approximate latitude, three-dimensional velocities, specific forces in the navigation frame, and direction cosine matrix which defines the coordinate frame transformation from the body frame to the navigation frame (68). See [9] for further details about generating a linearized error dynamics matrix.

$$\mathbf{F}_{15\times15} = f_{Pinson15}(lat, v_n, v_e, v_d, f_n, f_e, f_d, \mathbf{C}_{nb}) \tag{68}$$

A realization of INS errors can be obtained by propagating the state model according to:

$$\dot{x} = \mathbf{F}x + Gw, \quad E[w^2] = \mathbf{Q} \tag{69}$$

where $w_{15\times1}$ is a vector of white noise, and $\mathbf{Q}$ is the diagonal matrix of shaping filter terms according to the INS grade.

$$\mathbf{Q} = diag\left(\begin{bmatrix} \mathbf{0} & \sigma^2_{VRW} & \sigma^2_{ARW} & \frac{2*\sigma^2_{AccelBias}}{\tau_{Accel}} & \frac{2*\sigma^2_{GyroBias}}{\tau_{Gyro}} \end{bmatrix} \right)_{15\times15} \tag{70}$$

5.3.1.3 Generating Simulated INS Errors.

Initial errors were randomly generated with a mean of zero and an uncertainty determined by the grade of INS:

$$\hat{x}_0 = \mathbf{0}, \ P_0 = diag\left(\begin{bmatrix} \sigma^2_{\mathbf{p}} & \sigma^2_h & \sigma^2_{\mathbf{v}} & \sigma^2_\alpha & \sigma^2_{AccelBias} & \sigma^2_{GyroBias} \end{bmatrix} \right)_{15x15} \tag{71}$$

The uncertainties were set as described in table 10 to reflect more uncertainty with poorer quality INSs.

Table 10. Simulation Initial Conditions

Position $\sigma_{\mathbf{p}}$	Height σ_h	Velocity σ_v	Tilt σ_α	Acc Bias	Gyro Bias
0 (m)	5 (m)	$\sigma_{AccelBias}$	$\sigma_{GyroBias}$	$\sigma_{AccelBias}$	$\sigma_{GyroBias}$

Discrete realizations were generated using:

$$x_{t+1} = \mathbf{\Phi}x_t + w_t, \tag{72}$$

where $\mathbf{\Phi}$ was the transition matrix obtained by taking the matrix exponential of the linearized dynamics model $\mathbf{\Phi}_{15\times15} = e^{\mathbf{F}*dt}$, and w_t was a sample drawn from an additive-white-Gaussian source of strength Q. 100 realizations were generated for each grade, and the realization with the tenth largest distance root mean squared (DRMS) position error was selected as a representative INS sample for each grade. Figures 42 and 42b show the 3σ bounds and the chosen realizations of the various grades over a flight time of 14 minutes.

(a) (b)
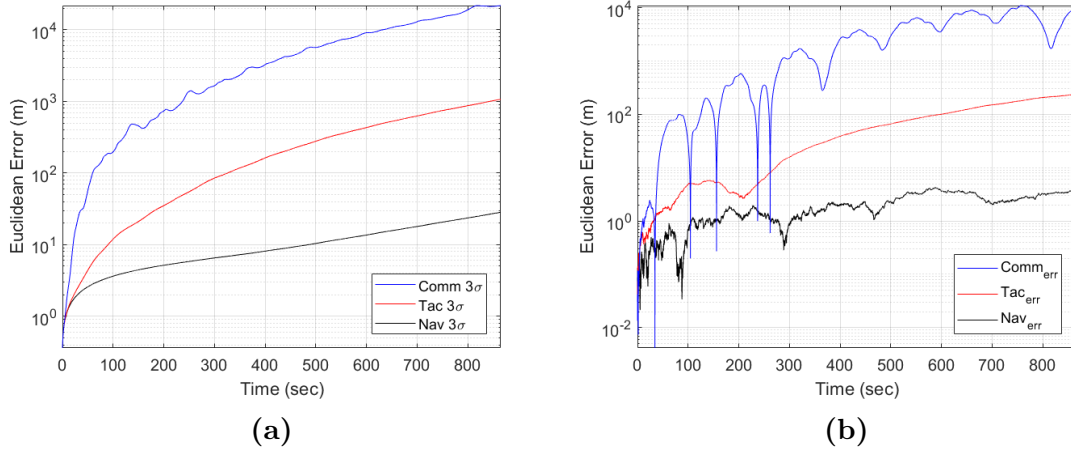
Figure 42. Different grades of manufacturing and calibration precision leads to orders of magnitude differences between drifting INS errors. The HG9900 is considered navigation grade, the HG1700 is considered tactical grade, and commercial grade refers to common MEMS IMUs. (a) 3σ bounds of possible errors for each INS grade. (b) One sampled realization of each INS grade

5.3.2 Aerial Inertial-Magnetic FastSLAM.

This navigation filter was an extension of the aerial magnetic SLAM filter demonstrated with a full-size magnetic surveying aircraft in [96]. We loosely coupled a FastSLAM filter to estimate and correct INS errors for an improved aircraft state estimate as outlined in figure 43. The major changes included an improved state space model to more realistically model INS errors, the use of GPR's covariance information in updating particle weights, and only resampling subsets of particle paths *and* their weights.
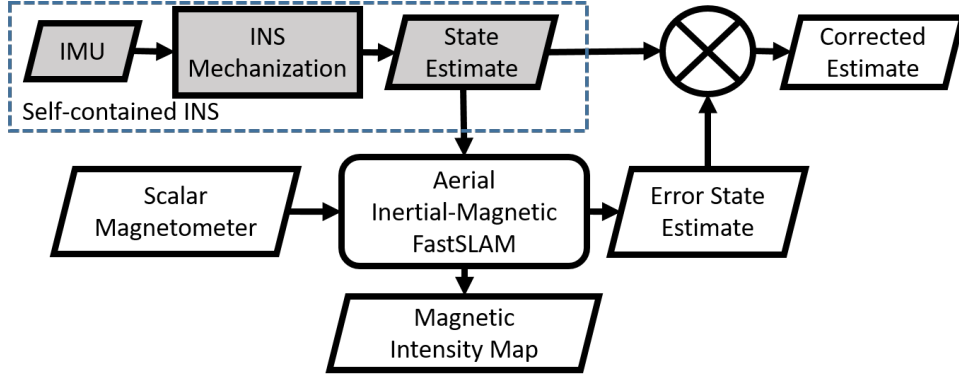
Figure 43. The system loosely coupled an INS solution to magnetic intensity measurements to correct for state errors.

SLAM estimates a path and map concurrently. While the concept of SLAM has been around since 1986 [72], FastSLAM was first introduced by Montemerlo in 2003 as a factored solution to SLAM with unknown data association [73]. Murphy [74] first presented the factorization of the full SLAM posterior into a product of N+1 recursive estimators: one estimator over robot paths, and N independent estimators over landmark positions, each conditioned on the path estimate:

$$p(x_{1:t}, \theta_{1:n}|z_{1:t}, u_{1:t}, n_{1:t}) = \underbrace{p(x_{1:t}|z_{1:t}, u_{1:t}, n_{1:t})}_{\text{trajectory posterior}} \underbrace{\Pi_{n=1}^{N} p(\theta_n|x_{1:t}, z_{1:t}, u_{1:t}, n_{1:t})}_{\text{landmark estimators}}. \qquad (73)$$

This factorization can be efficiently approximated with a Rao-Blackwellized particle

filter (RBPF) where each sample path of the vehicle is a particle. Each particle maintains it's own hypothesized map and determines when it revisits a portion of it's path. We present an extension of the FastSLAM algorithm used by [58], shown in algorithm 3 to the flight test dataset used by [21] for aerial magnetic navigation.

We will now describe each step of algorithm 3 for a single time-step. On line 2, the i-th of N particles uses it's previous state $x_{t-1}^{[i]}$ and control input u_t to propagate to it's current state $x_t^{[i]}$ according to the nine state Pinson INS error dynamics and noise model further described in the appendix. On line 3, a particle compares it's current state $x_t^{[i]}$ and measurement z_t to it's map model $m_{t-1}^{[i]}$ and returns an updated weight $q_t^{[i]}$ and list of currently revisiting particles $ActiveList$. On line 4, a particle updates it's individual map $m_{t-1}^{[i]}$ with the latest measurement $x_t^{[i]}$ and trajectory estimate z_t. The weights of the particles that did not hypothesize a revisit are multiplied by the mean of particle weights on the $ActiveList$ as shown in line 5. Line 7 states that if the number of effective particles falls below half of the total number of particles, systematic resampling occurs to replace poorly weighted particles with duplicates of highly weighted particles. The process concludes one iteration with an updated set of particles X_t approximating the current state estimate.

Algorithm 3: Aerial Inertial-Magnetic FastSLAM

    Input: X_{t-1}, u_t, z_t

    Output: X_t

1 **for** $i = 1$ *to* N **do**

2 $x_t^{[i]} = INS\_motion\_model(u_t, x_{t-1}^{[i]})$

3 $[ActiveList, q_t^{[i]}] = update\_particle\_weight(z_t, x_t^{[i]}, m_{t-1}^{[i]}, q_{t-1}^{[i]}, ActiveList)$

4 $m_t^{[i]} = update\_particle\_map(z_t, x_t^{[i]}, m_{t-1}^{[i]})$

5 $q_t^{[\sim ActiveList]} = mean(q_t^{[ActiveList]}) \cdot q_t^{[\sim ActiveList]}$

6 **if** $\frac{1}{\sum_{i=1}^{N}(q_t^{[i]})^2} < \frac{N}{2}$ **then**

7   Resample particles' states and weights that were on the *ActiveList* since

       the last resampling.

8 **return** X_t

Our contributions primarily involve the particle weighting function in line 3 of algorithm 3, and resampling in line 7. The *update_particle_weight*($\cdot$) function is further expanded with a flow chart in figure 44.
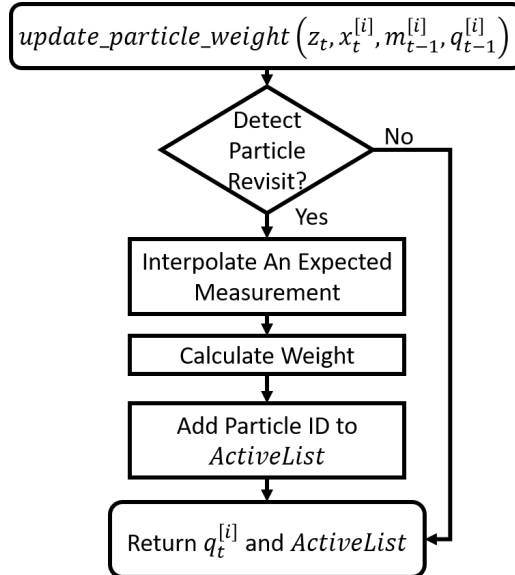
Figure 44. Updating each particle weight depends on if it hypothesizes a revisit or not

We will now step through each part of the process outlined in figure 44.

111

5.3.2.1 Detect Particle Revisit.

A particle detected a path crossing when there was more than two points from it's previous trajectory called trigger points within a trigger radius. This is illustrated by figure 45a where colored dots represent the magnetic intensity measurements along a particle's trajectory, squares represent trigger points as tracked points in a particle's trajectory, and asterisks indicate recent points to be ignored. A trigger radius of 18 meters was determined experimentally such that a particle would neither miss nor apply two particle weight updates to the same revisit.

5.3.2.2 Interpolate An Expected Measurement.

Instead of maintaining an entire map, each particle used a subset of point indices s of it's position history and measurements as inputs into an expected measurement function $\hat{z}^{[i]} = h(x_s^{[i]}, z_s)$. The interpolation points were selected from within a threshold distance as shown in figure 45b. $[t - \tau : t]$ represents a sequence of recent values that were ignored as to prevent recent measurements from affecting the result of interpolation [58].
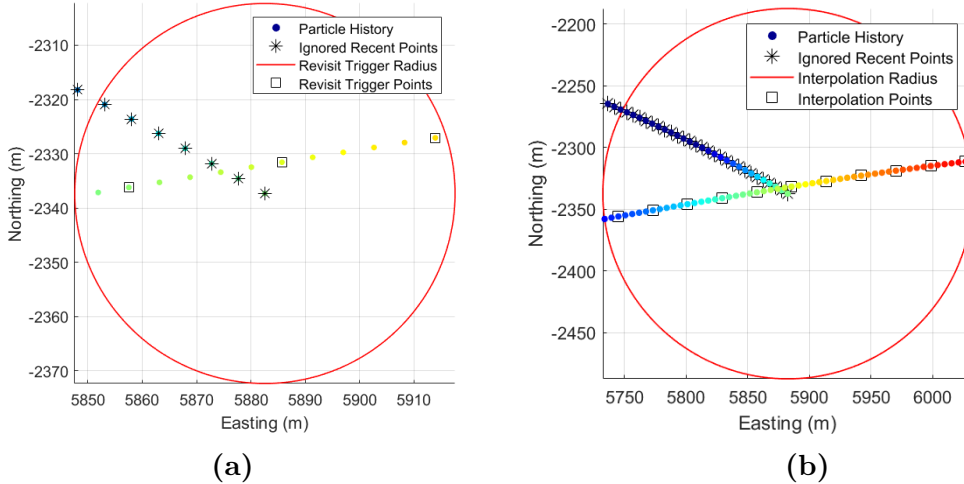
Figure 45. Particles individually detect revisits and select interpolation points conditioned on their own path histories. (a) Detecting a line revisit when # of trigger points withing a threshold radius >2. (b) Data selection for interpolation used a larger radius.

The expected measurement function $\hat{z}^{[i]} = h(x_s^{[i]}, z_s)$ interpolated an expected magnetic intensity measurement from a subset of the non-gridded particle history and magnetic measurements. GPR evaluated the input coordinates and their associated magnetic measurements as a realization of a zero-mean multivariate Gaussian process according to $\sigma_{se} = 5$, $\sigma_n = 5$, and $l = 100$ hyper-parameters which characterize correlation the magnetic field through the squared exponential function. The correlation between individual measurements at some points x_1 and x_2 is:

$$k(x_1, x_2) = \sigma_{se}^2 exp(\frac{(x_1 - x_2)(x_1 - x_2)^T}{2l^2}) + \sigma_n^2 \delta(x_1, x_2) \tag{74}$$

This created a regressive fit function which returned an expected value and covariance for a query point

$$[\hat{z}^{[i]}, R_t^{[i]}] = h(x_s^{[i]}, z_s, \sigma_{se}, \sigma_n, l). \tag{75}$$

This method is illustrated in figures 46a and 46b.
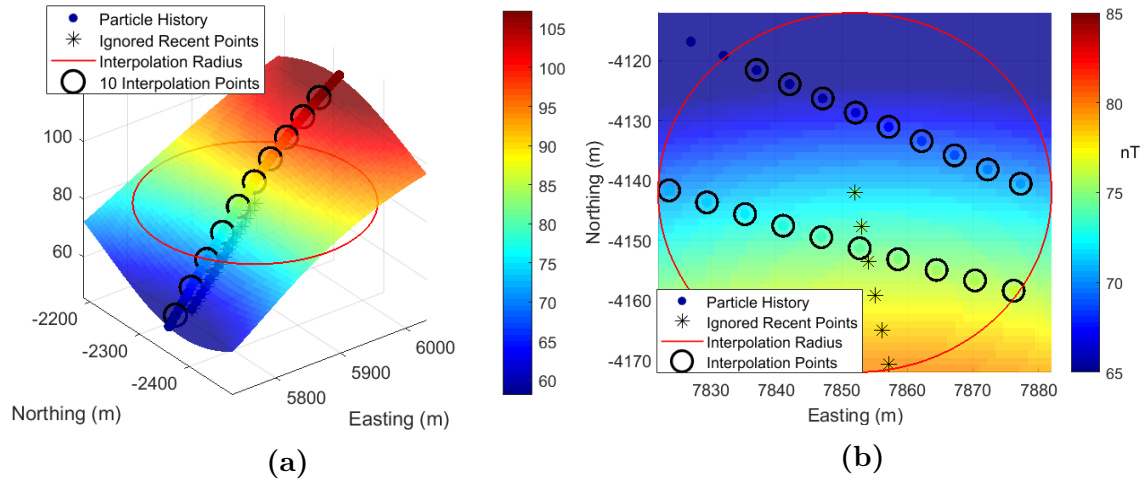
Figure 46. **Gaussian process regression estimating a grid of points given some circled input points. (a) GPR prediction around a line of points. (b) GPR prediction around a set of scattered points**

Magnetic intensity scalar fields are guaranteed to be continuous. GPR had the benefit of modeling the field as a smoothed best fit of measurements, and produced

an uncertainty value.

5.3.2.3 Calculate Weight.

Gaussian residual weighting evaluated the quality of a particle's hypothesis by contrasting the expected magnetic intensity with the actual measurement:

$$q_t^{[i]} = q_{t-1}^{[i]} exp\Big(- \frac{(z_t - \hat{z}_t^{[i]})^2}{2R_t^{[i]}} \Big), \tag{76}$$

where $q_t^{[i]}$ was an active particle's weight at the current time t, $q_{t-1}^{[i]}$ was the particle's previous weight, z_t was the current measurement, $\hat{z}_t^{[i]}$ was the particle's expected magnetic intensity from the measurement function $h(\cdot)$, and $R_s^{[i]}$ was the covariance output of GPR. The weighting of particles posed challenges when not all particles hypothesized revisiting at the same time. Haverinen and Vallivaara [58] addressed this by weighting the non-visiting particles by the average weight of the visiting particles. We expanded on this by only resampling from particles which appeared on the *ActiveList* since the previous resampling step. Additionally, subsets of particles that underwent resampling together also resampled their weights. Since information only enters the system during line revisits, this technique prevented the disproportionate favoring of particles which hypothesized many revisits over equally valid particles which were not revisiting as often.

5.3.2.4 Resampling.

The standard particle filter criteria from Liu [76] was used to determine when to resample:

$$N_{eff} = \frac{1}{\sum_{i=1}^{N} (\tilde{q}^{(i)})^2}, \quad \text{Resample If } N_{eff} < \frac{N}{2} \tag{77}$$

114

Where N is the total number of particles. Only particles which appeared on the *ActiveList* since the previous resampling step had their states and weights resampled and then the entire set of particles' weights were normalized according to $\tilde{\mathbf{q}}_t = \frac{\mathbf{q}}{\sum \mathbf{q}}$.

5.4 Results

A filter's SLAM performance should be measured by it's measurement and trajectory errors, as it's path and map estimates are relative to each other. A SLAM filter that accumulates a bias error in it's solution but is bounded over time is still considered a successful SLAM filter. This means that standard deviations in the error provide a measure of effectiveness along with root-mean-squared errors. The UAV canvassed a relatively small flight area. As a result, the spatial variation of the magnetic measurements was highly-planar. The resulting navigation information laid primarily along the slope of the plane in the northwest direction. However, there was some anomalous magnetic variation in the northeast corner of the flight area as seen in 41b. The filter estimate converged faster when the aircraft traveled near this anomaly. This might suggest that an actively exploring SLAM algorithm should attempt to revisit areas with identifiable magnetic variance for better convergence. Even with a limited amount of magnetic spatial variance, the filter still maintained valid position estimates below one hundred meters over a 1km by 1km area for all simulated INS grades. Table 11 shows the simulated INS errors according to grade, as well as errors after the SLAM filter was applied. The filter was unable to significantly improve the simulated navigation grade INS. The INS errors did not drift quickly enough for there to be diversity in the particles' maps for the short flight duration. The filter successfully constrained the simulated tactical grade INS to tens of meters. This is the same level of performance as previous work on a professional geomagnetic surveying aircraft over ten times the area [96]. The filter also constrained the

115

simulated commercial grade INS to around one-hundred meters DRMS error. Some tuning adjustments made the filter more robust to the erratic errors of a commercial grade INS. The earlier assumption which based the revisit trigger radius on an average translational velocity and sample rate was invalid with rapidly changing velocity errors. This was causing particles to miss or double-count revisits. The trigger radius shown in figure 45a was increased to 50 meters and the l hyper-parameter in equation (75) increased to 300 meters in order to include more measurements in hypothesized loop closures. This change was intended to prevent poor revisits from being missed, as this caused some particles to never hypothesize loop closures, and subsequently never experience resampling. Additionally, the number of particles was increased form 1000 to 3000 to better sample the proposal distribution before convergence.

Table 11. MagSLAM with real measurements and simulated INS grades

INS Grade	North Error (m)		East Error (m)		Radius Error (m)	
	RMS	σ	RMS	σ	DRMS	σ
Navigation (HG9900)	12.29	8.63	1.24	0.75	12.35	8.51
Navigation+SLAM	4.74	4.43	10.35	7.76	11.38	8.22
Tactical (HG1700)	434.27	257.39	41.37	41.02	436.24	287.69
Tactical+SLAM	24.74	17.98	31.12	24.10	39.76	24.54
Commercial	8792.26	6072.78	5279.09	3752.11	10255.37	7094.89
Commercial+SLAM	77.34	62.24	114.71	108.52	138.35	68.24

The ability of the filter to estimate and correct the INS position errors can be seen by contrasting the error plots in figure 47. The left column shows the drifting INS northing and easting position errors. All three grades of INSs along the left column show drifting errors. The right column shows the SLAM position estimate errors and the three-sigma bounds, which most noticeably constrained the tactical

116

and commercial grade INSs. Sudden decreases in the three-sigma bounds in the right column correspond to particle resampling where particles with inconsistent magnetic measurements were reassigned the paths and weights of particles with more self-consistent measurements.
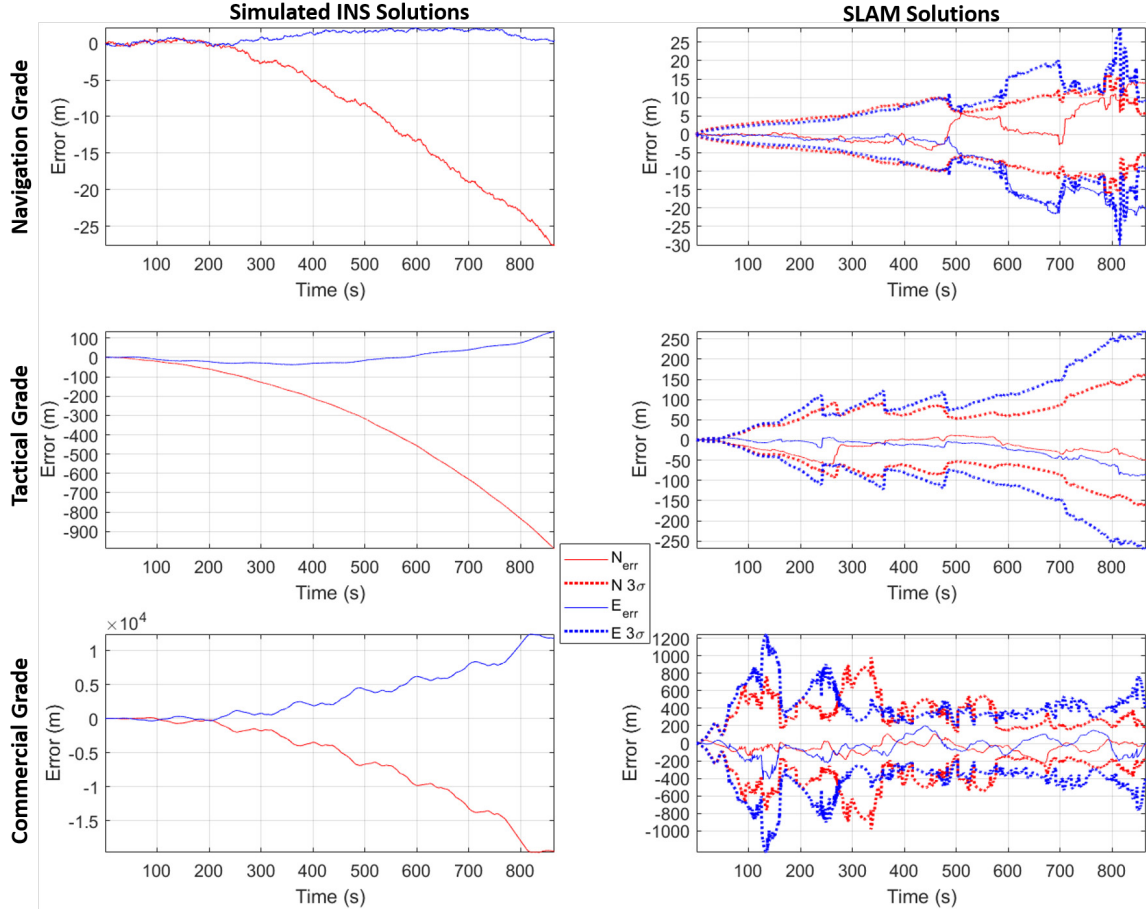
Figure 47. Contrasting INS errors (left) and SLAM errors (right) illustrates the filter's ability to constrain drifting position errors.The left column shows simulated navigation, tactical, and commercial INS errors. The right column shows the corresponding SLAM filters' errors being contrained.

The improvement in the filter's trajectory estimate can be seen in the map comparisons between the three INS grades in the left column, and the average trajectories of the surviving particles in the right column of figure 48. The truth trajectory should look like the one in figure 41b. The top row shows that measurements, illustrated as colors, are similar at path crossings in both the INS and SLAM path estimate.

117

This is because the simulated navigation grade INS did not accumulate a significant position drift in 14 minute flight. In the middle row, we can start to notice color inconsistencies at path intersections in only the tactical grade INS estimate to the left. There is significant northing position drift in the left column, but the SLAM path on the right is still similar to the true path. The most drastic illustration of filter performance is in the bottom row, where the commercial grade INS path estimate on the left drifted over 30 km away, and the SLAM path estimate on the bottom-right still shows resemblance to the flight path in figure 41b.
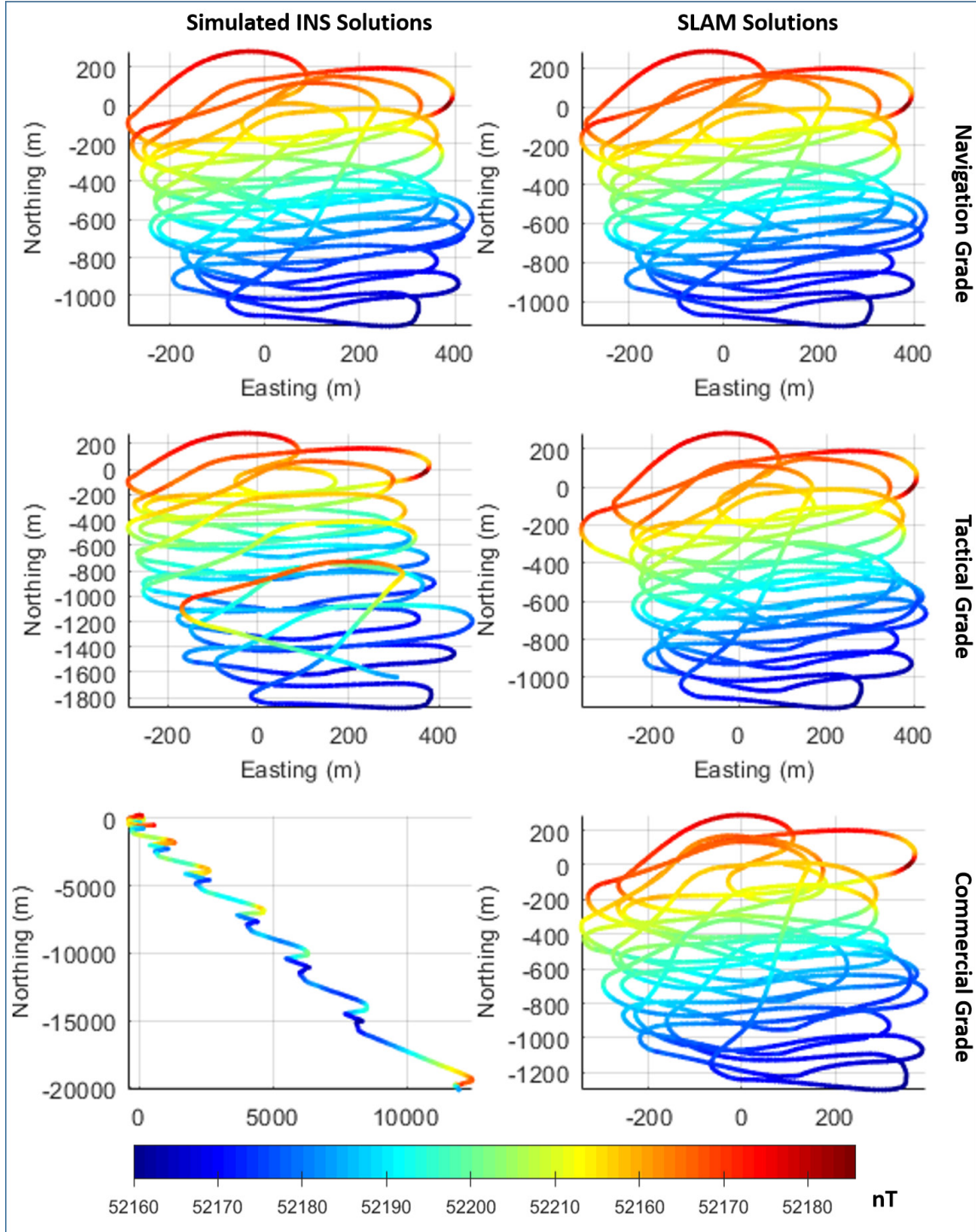
Figure 48. The average surviving particles show a smooth self-consistent map after SLAM. The left column shows simulated navigation, tactical, and commercial INS trajectories with magnetic intensity measurements. The right column shows the corresponding SLAM trajectories with self-consistent measurements at path intersections. The colors of the flight lines represent the UAV magnetic intensity measurements.

119

A FOM is a metric to evaluate the self-consistency of scalar magnetic measurements at path intersections. We define FOM for this analysis in units of nano-Teslas as:

$$FOM = \sqrt{\frac{\sum_{\{x,x^*\}}^{N} (z - z^*)^2}{N}}, \tag{78}$$

where x and x^* are any two non-sequential points in the flight within 1 meter of each other. z and z^* are the magnetic intensity measurements corresponding to point pair x and x^*, and N is the number of point pairs. Figure 49 illustrates the tactical grade INS trajectory (left) and corresponding SLAM corrected trajectory (right) with the same magnetic intensity measurements producing different FOM. Pairs of black circles indicate non-sequential measurement pairs at line crossings: x and x^*. Black lines connecting black circles indicate the difference between paired measurements $z - z^*$.
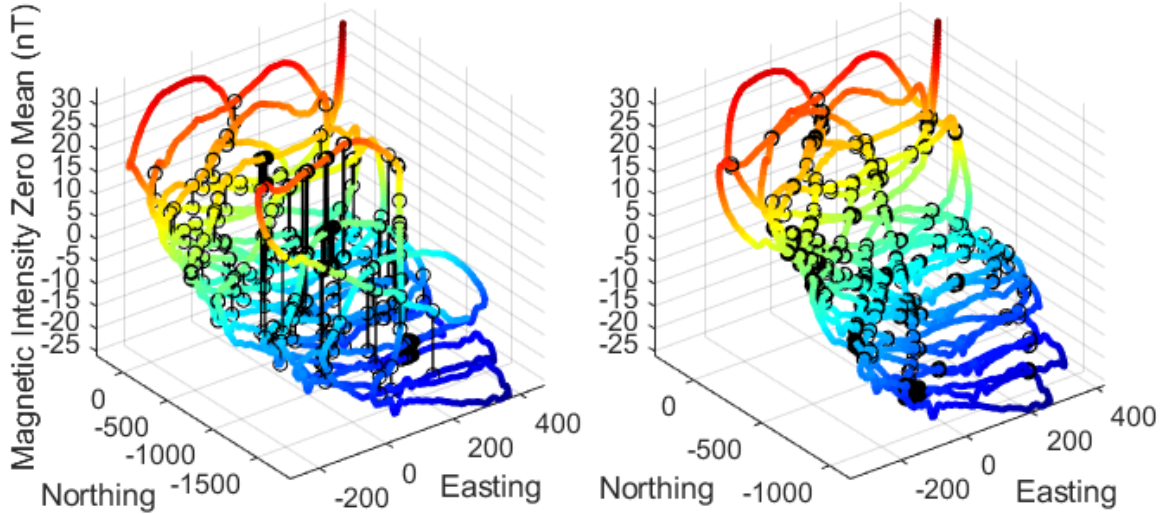
Figure 49. Calculating figure of merit for different path estimates sharing the same magnetic intensity measurements. (Left) Tactical grade INS trajectory $FOM = 10.15$ nT. (Right) Corresponding SLAM estimated trajectory $FOM = 1.52$ nT

It is expected that measurements with an incorrect INS path estimate would produce a larger FOM, and a SLAM correction which decreases position errors should subsequently show a reduction in the FOM. Table 12 tabulates the FOMs for the truth

trajectory, each INS grade trajectory, and each corresponding SLAM filter sequential output $\hat{x}_t$. Interestingly, SLAM reduced the FOM more than the truth trajectory for the navigation-grade INS since the truth trajectory did not have perfectly consistent measurements.

Table 12. Trajectory Measurement Inconsistency

Trajectory Estimate	Map FOM (nT)		
Grade	Navigation	Tactical	Commercial
Truth	1.079	1.079	1.079
INS	1.40	10.15	7.90
$\hat{x}_t$	1.073	1.52	2.46

5.5   Conclusion

A aerial magnetic SLAM filter shown to work on a single-engine manned aircraft over a large area was applied to a UAV flight one-tenth of the size and duration. Three grades of inertial systems were simulated to determine the feasibility of using real magnetic intensity measurements to constrain a practically-sized INS on a UAV. The simulated navigation grade INS did not drift enough during the short flight to produce inconsistent magnetic measurements. The simulated tactical and commercial grade INS solutions were constrained to tens of meters and one-hundred meters respectively. Overall, the filter maintained trajectories with self-consistent magnetic measurements. A primarily planar magnetic intensity field showed how the filter better constrained position errors in the direction of magnetic variation. Flying lower or over a larger area should capture more magnetic variation and improve filter performance for lower quality INSs.

121

VI. Thesis Conclusions

This research presented three contributions. First, aerial magnetic navigation's dependency on the availability and accuracy of prior-surveyed magnetic maps was removed. Secondly, a UAV capable of to collecting precise and spatially-consistent magnetic intensity measurements during flight was designed and flown. Lastly, low-altitude magnetic navigation was demonstrated on a UAV without a prior magnetic map.

A FastSLAM filter was shown to remove the requirement for a prior-surveyed magnetic map by constraining INS errors with magnetic intensity measurements during flights that repeatedly overlapped their own trajectories. A real dataset on a Cessna 208 magnetic surveying aircraft was shown to constrain an actual navigation-grade INS solution to tens of meters on a 100 minute flight. A COTS UAV was configured and a magnetic disturbance model was determined within two nano-Teslas using a calibration flight. The aircraft disturbance model was used on six subsequent flights to produce spatially consistent magnetic intensity measurements. A SLAM filter was applied to real UAV magnetic intensity measurements with various simulated INS grades and constrained the UAV drift to tens of meters; demonstrating the feasibility of UAV magnetic SLAM with practical INS grades. The methods demonstrated in this research provide aircraft with a new globally-available and passively-sensed GPS-alternative navigation capability which does not require prior map data. The most beneficial application of these methods would be on aircraft loitering over large areas, at low altitude, or both.

6.1 Future Work

Challenges remain to implementing aerial magnetic SLAM on a UAV in real-time. This section presents current challenges as opportunities for future research.

6.1.1 Flight Patterns.

Aerial magnetic navigation's dependency on prior magnetic map data can be alleviated on the condition that the aircraft covers a wide area and revisits previously traversed areas frequently. The dependency on a magnetic map can be removed at the expense of requiring a large but loitering flight pattern. This raises questions about an autonomous schema to identify and actively balance mission priorities with navigation accuracy. It may be possible to identify magnetic anomalies as landmarks and actively seek them out to improve filter performance, as well as systematically exploring new areas to build a map and travel longer distances with it. Improving the GPR covariance kernel to better incorporate correlations from magnetic field physics, altitude, and time into generating expected measurements could extend this method to longer flights in three dimensions.

6.1.2 Time-Varying Magnetic Fields.

The methods in this filter have minimized time-varying components of the magnetic field through short flight times or by correcting the measurements for diurnal variations beforehand. Although the techniques still work with diurnal variations present in the specific data-sets collected here, this will not always be the case in real-world applications. A method to account for time-varying magnetic measurements still needs to be addressed. Such research could incorporate a time-correlation component to GPR's correlation function, or passively receive diurnal data transmission updates from local observatories in real time.

6.1.3   Filter Stability.

Particle filters can be unstable without significant attention to somewhat ad hoc tuning practices. Modern SLAM techniques have largely evolved past the use of causal particle filters and could be the subject of future research. This filter could greatly benefit from graph-based methods or from incorporating a maximum likelihood algorithm into the proposal distribution using current magnetic measurements.

Appendices

Appendix A. MagSLAM Implementation Details

This appendix presents implementation details pertaining to the filter design, GPR prior mean correction, and sensor description.

A.1   Filter Design

This RBPF implemented a linearized dynamics model and non-linear measurement equation from [75] algorithm I: model 4. Only the modified portions of this filter for SLAM are discussed in this paper for brevity. The filter began with a known global position as assumed to be the case in the loss of GPS availability. Particles were drawn as potential aircraft paths based on the nine-state Pinson INS error model from [9]. Particle propagation provided a proposal distribution of INS errors. When particles hypothesized loop closures, they interpolated expected intensities from a shared set of measurements conditioned to their individual paths, compared it to the current actual measurement, and were weighted using a Gaussian residual weighting function. Over time, particles with the most self-consistent measurements at path crossings survived re-sampling to approximate the errors in the overall flight path. The INS solution was adjusted by the weighted sum of the particles' position errors to provide a new position estimate. This filter's simplicity was deliberate as a straightforward extension of work done by Vallivaara et al. with a Roomba-style robot using an indoor magnetic vector disturbance field [57].

A.1.1   State Partitioning.

The state variable x was partitioned into two horizontal position error particle states x^n, and seven linearized error states x^l: altitude, three-dimensional velocity, and three-dimensional tilt in the body reference frame.

$$x = \begin{bmatrix} x^n \\ x^l \end{bmatrix} \tag{79}$$

The matrix Φ was created at every time step by discretizing the linearized Pinson error dynamics model F which was then partitioned into nonlinear and linear components for the linear dynamics model in equations 81a and 81b. The nonlinear measurement function is represented in equation 81c.

$$\Phi = \begin{bmatrix} \Phi_n^n & \Phi_l^n \\ \Phi_n^l & \Phi_l^l \end{bmatrix} = e^{F \cdot dt} \tag{80}$$

$$
\begin{align}
x_{t+1}^n &= \Phi_{n,t}^n x_t^n + \Phi_{l,t}^n x_t^l + w_t^n, \tag{81a} \\
x_{t+1}^l &= \Phi_{n,t}^l x_t^n + \Phi_{l,t}^l x_t^l + w_t^l, \tag{81b} \\
y_t &= h(x_t^n) + e_t \tag{81c}
\end{align}
$$

The driving noise was defined by $w_t^n = \mathcal{N}\left(\mathbf{0}, \mathbf{Q}^n\right)$, $w_t^l = \mathcal{N}\left(\mathbf{0}, \mathbf{Q}^l\right)$, and $e_t = \mathcal{N}\left(0, R\right)$. The measurement equation $h_t(x_t^n)$ in 81c only provided information about the linear states x_t^l implicitly via the proceeding Kalman filter time update [75].

A.1.2 Gaussian Process Regression as an Expected Measurement Function.

Instead of maintaining an entire map, each particle used a subset of point indices s of it's position history and measurements as inputs into an expected measurement function $\hat{z}^{[i]} = h(x_s^{[i]}, z_s)$. The GPR expected measurement function is written as follows:

$$[\hat{z}_t^{[i]}, R_t^{[i]}] = GPR(x_t^{[i]}, [x_s^{[i]}, z_s], \sigma_{se}, l, \sigma_n) \tag{82}$$

GPR returned an expected value $\hat{z}_t^{[i]}$ for a query point, in this case a particle's current position $x_t^{[i]}$, as well as a covariance $R_t^{[i]}$ for the individual particle at that point in time. In the Louisa Virginia flight test [96], the hyper-parameters σ_{se}, l, and σ_n were used by the squared exponential kernel function and were experimentally determined to be 50, 150, and 1 respectively. For the UAV magnetic SLAM demonstration, values were chosen to be 5, 100, and 5. The function estimated:

$$\hat{z}_t^{[i]} | (x_t^{[i]}, x_s^{[i]}, z_s) = \mathcal{N} \left(\mathbf{K}_* \mathbf{K}^{-1} z_s, \ \mathbf{K}_{**} - \mathbf{K}_* \mathbf{K}^{-1} \mathbf{K}_*^T \right) \tag{83}$$

where $\mathbf{K}$, $\mathbf{K}_*$, and $\mathbf{K}_{**}$ were built by a squared exponential function as described in [77]. The function to compute the individual cross terms between some x_1 and x_2 in $\mathbf{K}$ was:

$$k(x_1, x_2) = \sigma_{se}^2 exp(\frac{(x_1 - x_2)(x_1 - x_2)^T}{2l^2}) + \sigma_n^2 \delta(x_1, x_2) \tag{84}$$

GPR assumes a zero mean multivariate Gaussian process. Therefore, a prior-mean correction was applied by removing the mean of the measurements at each particle's interpolation points. This turns equation 83 into:

$$\hat{z}_t^{[i]} | (x_s^{[i]}, z_s) = \mathcal{N} \left((\mathbf{K}_* \mathbf{K}^{-1} (z_s - E(z_s)) + E(z_s), \ \mathbf{K}_{**} - \mathbf{K}_* \mathbf{K}^{-1} \mathbf{K}_*^T \right) \tag{85}$$

A.2 Sensor Description

Magnetic intensity measurements were collected with a self-oscillating split-beam Cesium-pumped vapor scalar magnetometer. These precision magnetometers are able to precisely resolve the intensity of a magnetic field with heading errors on the order of tenths of nano-Teslas. A scalar magnetometer similar to the one used in the survey is shown in figure 50 and whose characteristics are listed in table 13.

Figure 50. Geometrics Scalar Magnetometer [98]

Table 13. Scalar Magnetometer Characteristics

Characteristic	Value
Size	41,259 cc
Weight	450 g
Type	Self-Oscillating split-beam Cesium vapor
Operating Range	20,000 to 100,000 nT
Heading Error	$\pm$ 0.15 nT
Absolute Accuracy	< 3 nT
Sensitivity	0.003 nT at 10Hz

Appendix B. Calibration Method Comparisons

This appendix presents the investigation of the best calibration data-set and method combination in order to generate a set of aircraft disturbance coefficients from the UAV flights. This appendix describes the different calibration data collections and how well each calibration model fit each dataset. Applying the models to separate flights and observing self-consistency ultimately determined which dataset and model was the most consistent under the same aircraft configuration. Three calibration datasets were compared in conjunction with five aircraft disturbance field model variations.

B.1   Calibration Methodology

Five variations of the seminal Tolles-Lawson aircraft disturbance model [69] were evaluated. These include the standard 18-coefficient model, a modified 21 coefficient model accounting for compass errors, and models accounting for the spatial gradient of magnetic field.

B.1.1   Tolles and Lawson Disturbance Model.

A traditional Tolles and Lawson disturbance model as defined in section 2.2.2.2 was included to compare traditional aeromagnetic surveying methods to low-altitude UAV applications. This model assumes the calibration flight as described in 2.2.2.1 is at a high enough altitude that the spatial gradient of the magnetic field is negligible and that the vector magnetometer is calibrated.

B.1.2   Removing Spatial Gradient.

In reality, a calibration flight will have some spatial gradient as discussed in [99]. The local spatial gradient of a calibration flight can be modeled as a plane and

removed from a calibration dataset. The general form of a three-dimensional planar surface is defined as:

$$0 = ax + by + cz + d. \tag{86}$$

Defining x, y, and z to be easting, northing, and magnetic intensity, respectively, any horizontal planar variation in magnetic intensity is modeled by solving for z:

$$z = -\frac{ax + by + d}{c} \triangleq \begin{bmatrix} x & y & 1 \end{bmatrix} \begin{bmatrix} a_1 \\ a_2 \\ a_3 \end{bmatrix} \tag{87}$$

Adding three horizontal terms, x, y, and 1 to the X matrix isolates the first 18 coefficients from the affects of a spatially varying planar component. This becomes more important when calibrating a small UAV at low altitude where the spatial variance will be greater. This can be extended to model the spatial variance as a quadratic plane:

$$z = -\frac{ax + by + cxy + dx^2 + ey^2 + f}{g} \triangleq \begin{bmatrix} x & y & xy & x^2 & y^2 & 1 \end{bmatrix} \begin{bmatrix} a_1 \\ a_2 \\ a_3 \\ a_4 \\ a_5 \\ a_6 \end{bmatrix} \tag{88}$$

These additional terms account for the spatial variation only when solving for coefficients. Only the first 18 out of 24 coefficients were used to remove the aircraft effects on other datasets.

B.1.3 Modified Tolles And Lawson Model.

The 18-coefficient Tolles and Lawson calibration model assumes calibrated vector magnetometer readings, and a non-varying total field. These premises are invalid when attempting to calibrate a UAV with a noisy MEMS compass at relatively low altitudes where the magnetic field is spatially varying. Han et al. developed an aeromagnetic surveying calibration method robust to strap-down vector magnetometer errors [70]. They incorporate the ratio between the vector norm of the vector magnetometer and the scalar magnetometer measurement, use finite-impulse response (FIR) filtering to isolate correlations in the frequency bandwidth of interest, and include position terms to account for the presence of a spatially varying field. Using a FIR filter is essentially a linear operation which allows correlations to be made between aircraft maneuvers and corresponding signal introduced in the magnetic measurements frequency band of interest. Importantly, the relationship between the calibration coefficients that result from solving a linear equation of FIR band-passed measurements is maintained for whole measurements which can be applied in real time without band-pass filtering. The major contributions from [70] was a 50Hz low pass FIR filter to capture the disrupting frequency components of the aircraft maneuvers with a slow-moving aircraft at low altitudes and the 23 coefficient model used to include compass error terms and spatial gradient.

B.1.4 Determining the Best Model With Real Data.

The traditional Tolles-Lawson method, modified Tolles-Lawson model, and corrections for a spatial gradient were compared using several calibration datasets. The calibration datasets were a ground hand-tumble, a traditional square calibration flight, and using a gridded flight pattern. Figures 51, 52, and 53c compare the magnetic disturbance field to the application of: Tolles and Lawson 18 coefficient model (TL),

modified Tolles and Lawson 21-coefficient model (MTL), Tolles and Lawson accounting for planar field (TLL), Tolles and Lawson accounting for quadratic field (TLQ), and modified Tolles and Lawson accounting for a planar field (MTLL). Biases of 200, 100, 70, 40, 20, and 0 were added to the residual signals to separate them for comparison. The residual signal with the least variance after correction determined the best method to explain the magnetic measurements in that dataset. Any remaining signal which is neither correlated to aircraft orientation nor a linear gradient is the resulting anomalous signal.

B.2   Calibration Datasets

The following subsections describe the three data collections used for calibration using the previously mentioned methods: a stationary ground tumble, a geomagnetic-surveying calibration flight, and a gridded survey flight.

B.2.1   Ground Tumble Dataset.

The first dataset attempted to characterize the aircraft magnetic disturbance field was a ground tumble. The assembled aircraft in it's flight configuration was carried out to a field. All systems were activated except for the engine for obvious safety reasons. A drastic range of aircraft orientations were exercised at three separate physical locations in the field in an attempt to capture a full range of analogous aircraft maneuvers. The technique consisted of three people physically moving the aircraft in roll, pitch, and yaw over a stationary point in a magnetically-quiet area. The concept sought to isolate the aircraft orientation affects in the presence of a non-varying magnetic environment. This method failed to capture the effects from a running engine as well as the electromagnetic servo actuators during aircraft maneuvers. This collection was also likely corrupted from the presence of three people manipulating

the orientation of the aircraft. Figure 51 shows the result of using the tumble calibration to produce coefficients where each method attempts to model the measurements under the assumption that the measurements changed only with aircraft orientation. A perfect model under perfect assumptions should produce a constant value.
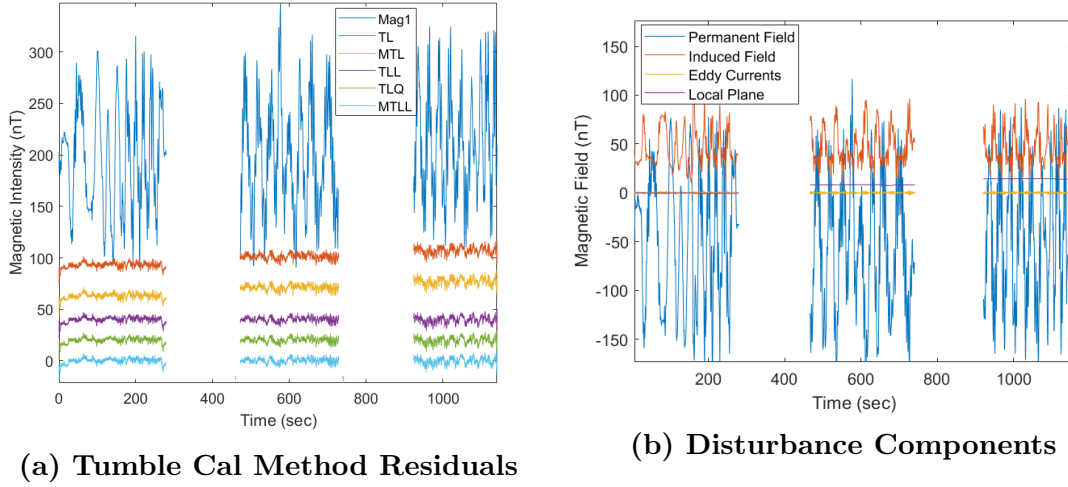

(a) Tumble Cal Method Residuals

(b) Disturbance Components

Figure 51. Ground Tumble Disturbance Modeling

B.2.2 Calibration Flight Squares, Circle, and CloverLeaf.

The second attempted method was a standard industry calibration flight 52a. First, a square flight path was flown at the highest altitude allowed at the time, which was 450 meters AGL according to our safety plan, while actuating control inputs called doublets on each of the straight legs of the square. Next, the square pattern was reversed and control variations were again actuated on each side of the square. This technique seeks to exercise the practical variation of the aircraft's orientation with respect to Earth's magnetic field vector. A loitering circle pattern was held until the cloverleaf mission profile was loaded remotely. Finally, a clover leaf pattern was flown as a means to validate a self-consistent center of the cloverleaf regardless of heading or aircraft orientation. Figure 52 shows the results of each calibration method applied to the entire calibration flight at 450 meters altitude AGL. The band-passed signal

134

was predicted by the modified Tolles-Lawson method with a standard deviation of 0.63 nano-Teslas. The components of the disturbance field model are shown in figure 52b. Of note is the negligible eddy current contribution and significant planar spatial variation. This makes sense due to the wood structure of the aircraft and low-altitude flight. Unfortunately, an aircraft configuration change was required after this flight which made the calibration coefficients invalid for the next flights. The resulting inconsistency in the magnetic field for the gridded flight was observably correlated with heading.
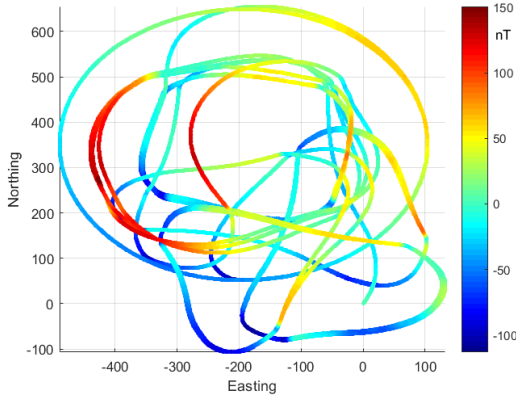
(a) Calibration Trajectory with Raw Measurements (Zero-Mean)
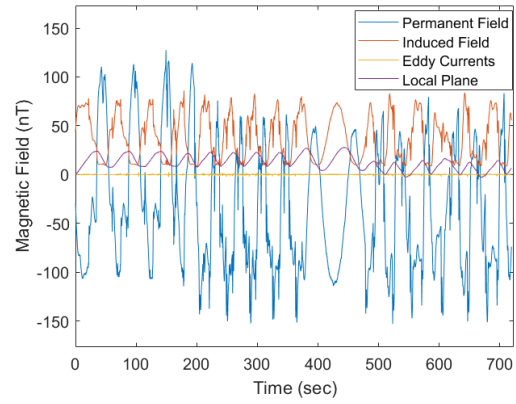
(b) Disturbance Components
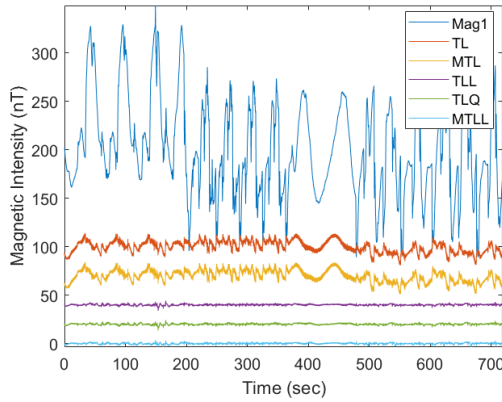
(c) Calibration Method Residuals

(d) MTLL-Calibrated CloverLeaf

Figure 52. Calibration Flight Disturbance Modeling

135

B.2.3 Gridded Flight Dataset.
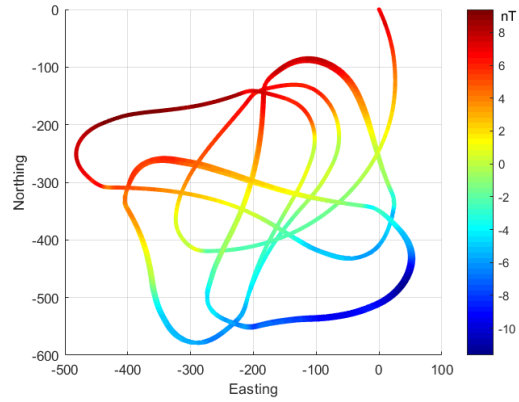
Even with disturbance model coefficients solved from the calibration flight, heading correlated irregularities in the gridded trajectory indicated a remaining heading-dominant error. This was likely due to an aircraft configuration change that occurred between the calibration flight and the gridded flight where aluminum engine mounting bolts were replaced with steel bolts. Since it was observable that the magnetic field for this area was planar, the gridded trajectory data could be used as a calibration dataset instead. This method produced more spatially self-consistent results in the remaining flights than any of the previous calibration datasets. It is possible that using the gridded survey flight to characterize the aircraft coefficients may have given greater distinction between the local planar field and heading errors, in addition to the fact that it was a longer collection.

(a) Raw Measurements (zero mean)

(b) Disturbance Components

(c) Calibration Method Residuals

(d) MTLL-Calibrated (zero-mean)
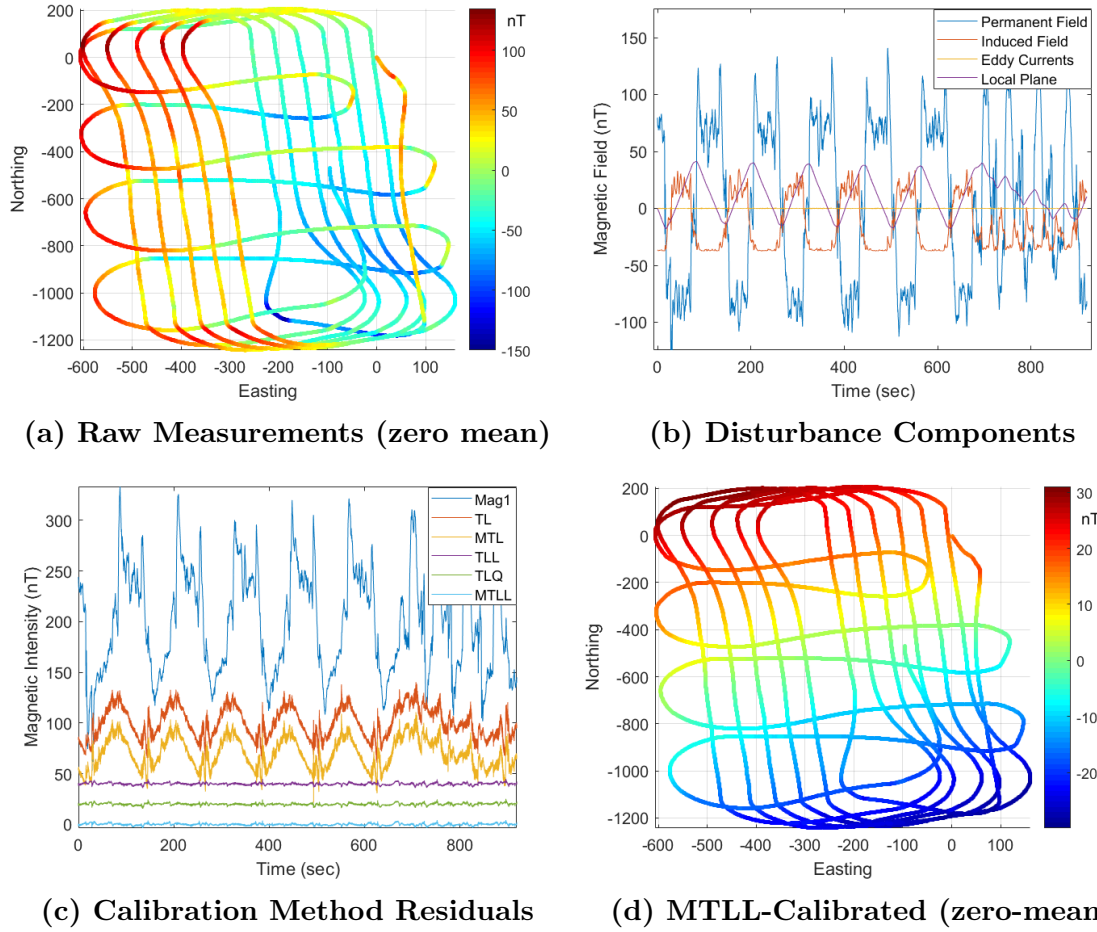
Figure 53. Using the gridded trajectory measurements provided self-consistent calibration coefficients. (a) Gridded survey trajectory at 100m AGL with 50 and 160 meter horizontal and vertical line spacing. (c) Compensation residuals shifted by method

B.3   Calibration Dataset and Method Comparison

The best disturbance model was determined by comparing the standard deviation of the difference between the disturbance measurements and the models as summarized in table 14. The modified Tolles-Lawson method in conjunction with modeling the field as a linear plane had the lowest residual variance and is proposed as the better model in this case. Another indicator of a valid calibration method is when it produces spatially self consistent maps from other sets of measurements. Each dataset was produced a set of MTL coefficients which then attempted to correct the SLAM

137

flight measurements. The 1 Hz low-passed aircraft compensated measurements can be compared visually in figure 54.

Table 14. Calibration Method Residuals

Disturbance Model	Tumble Residual σ	Cal Flight Residual σ	Grid Residual σ
Raw Mag1	51.621 nT	50.014 nT	50.515 nT
TL	6.590 nT	5.946 nT	14.774 nT
MTL	6.576 nT	5.946 nT	14.764 nT
TLL	2.985 nT	0.661 nT	1.049 nT
TLQ	2.983 nT	0.6588 nT	1.007 nT
MTLL	2.984 nT	0.6586 nT	0.975 nT

(a) Tumble Cal Coefficients

(b) Cal Flight Coefficients

(c) Gridded Flight Coefficients
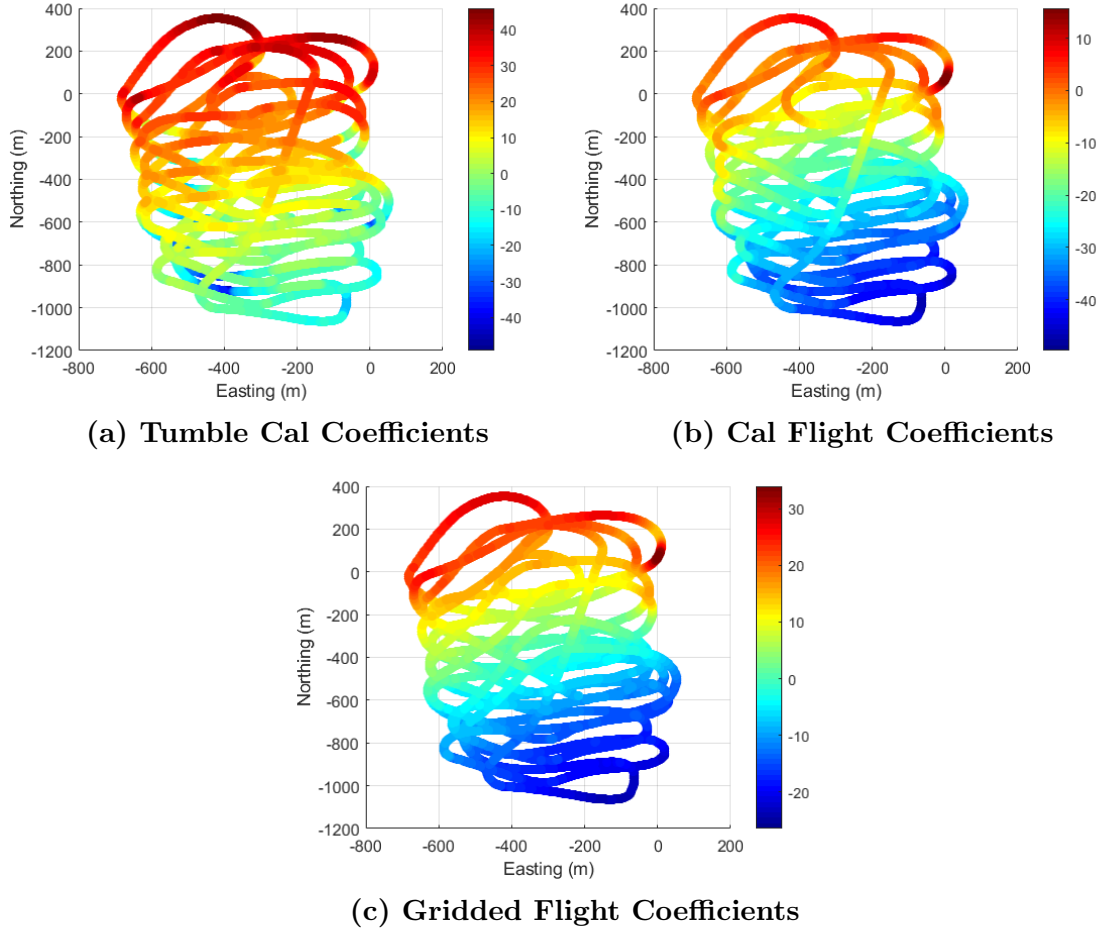
Figure 54. Magnetic intensity measurements for SLAM flight after calibration with different sources of coefficients and 1 Hz low-pass filter

B.3.1 Chosen Calibration Approach.

The modified Tolles-Lawson calibration approach was chosen based on slightly superior performance as can be seen in table 14. Raw measurements were used to solve for the calibration coefficients.

1. Solving For Aircraft Characterization Coefficients

    (a) Use a calibration dataset to generate a $t \times 23$ matrix $\triangle$ according to [70] to include horizontal position measurements.

139

(b) Use a non-linear least squares solver to solve for the 23 coefficients: $argmin_{\eta}(\triangle\eta - (B_s - mean(B_s)))$.

(c) The first 21 coefficients θ characterize the aircraft configuration's disturbance field.

2. Compensating Real Measurements On Subsequent Flights

(a) A row-vector δ from compass direction cosines, their derivatives, and the magnitude ratio between the compass and the scalar magnetometer λ was constructed at each time step.

(b) The row vector δ was multiplied by the calibration coefficients to produce the aircraft disturbance signal.

(c) The aircraft disturbance signal was subtracted from the raw measurements.

(d) The corrected raw measurements were passed through a 1Hz low-pass filter $f_{LP}(B_s - \delta\theta)$

Bibliography

1. A. Chulliat, P. Alken, A. Woods, S. Maus, S. Macmillan, and V. Ridley, "The US/UK World Magnetic Model for 2015-2020," National Geophysical Data Center, NOAA, Tech. Rep., 2015.

2. Cessna 208b Grand Caravan. [Online]. Available: {http://www.sgl.com/PDFs/Cessna%20208B-v3.0.pdf}

3. MFAM Technology. [Online]. Available: {http://mfam.geometrics.com/}

4. A. Canciani and J. Raquet, "Absolute Positioning Using the Earth's Magnetic Anomaly Field," *Navigation, Journal of the Institute of Navigation*, vol. 63, no. 2, 2016.

5. ——, "Self Building World Models for Navigation," in *Proceedings of the 2017 International Technical Meeting of The Institute of Navigation*, 2017.

6. G. T. Schmidt, "Navigation Sensors and Systems in GNSS Degraded and Denied Environments 2018," *2018 25th Saint Petersburg International Conference on Integrated Navigation Systems (ICINS)*, pp. 1–12, 2018.

7. J. A. Volpe, "Vulnerability Assessment of the Transportation Infrastructure Relying on the Global Positioning System," Office of the Assistant Secretary for Transportation Policy U. S. Department of Transportation, Tech. Rep., 2001.

8. J. S. Warner, D. Ph, R. G. Johnston, and D. Ph, "A Simple Demonstration that the Global Positioning System (GPS) is Vulnerable to Spoofing," *The Journal of Security Administration*, 1995.

9. D. H. Titterton and J. L. Weston, *Strapdown Inertial Navigation Technology*. IET, 2004.

10. R. J. Prazenica, A. Watkins, and A. J. Kurdila, "Vision-Based Kalman Filtering for Aircraft State Estimation and Structure from Motion," pp. 1–13, 2005.

11. C. N. Taylor, M. J. Veth, J. F. Raquet, and M. M. Miller, "Comparison of Two Image and Inertial Sensor Fusion Techniques for Navigation in Unmapped Environments," *IEEE Transactions on Aerospace and Electronic Systems*, vol. 47, no. 2, pp. 946–958, 2011.

12. G. Balamurugan, J. Valarmathi, and V. P. Naidu, "Survey on UAV navigation in GPS denied environments," *International Conference on Signal Processing, Communication, Power and Embedded System, SCOPES 2016 - Proceedings*, pp. 198–204, 2017.

13. J. J. Leonard, A. A. Bennett, C. M. Smith, H. Jacob, and S. Feder, "Autonomous Underwater Vehicle Navigation," MIT Marine Robotics Laboratory Technical Memorandum 98-1, Tech. Rep. [Online]. Available: https://pdfs.semanticscholar.org/3b66/970b4f138e14a975d7b05b29c9bffc36486a.pdf

14. M. E. West, T. R. Collins, J. R. Bogle, A. Melim, and M. Novitzky, "An Overview of Autonomous Underwater Vehicle Systems and Sensors at Georgia Tech." [Online]. Available: https://smartech.gatech.edu/bitstream/handle/1853/38875/GTAUVWorkshopPaper-MU3.pdf?sequence=1{\&}isAllowed=y

15. S. Barkby, S. B. Williams, O. Pizarro, and M. V. Jakuba, "Bathymetric SLAM with no map overlap using Gaussian processes," *IEEE International Conference on Intelligent Robots and Systems*, pp. 1242–1248, 2011.

16. J. Kim and S. Sukkarieh, "Autonomous airborne navigation in unknown terrain environments," *IEEE Transactions on Aerospace and Electronic*

Systems, vol. 40, no. 3, pp. 1031–1045, jul 2004. [Online]. Available: http://ieeexplore.ieee.org/document/1337472/

17. J. Cornwall, K. Case, C. Callan, A. Despain, F. Dyson, J. Goodman, R. Jeanloz, G. Joyce, N. W., T. Prince, C. Stubbs, and P. Weinberger, "Non-GPS Methods of Geolocation," DARPA, Tech. Rep., 2002. [Online]. Available: http://www.dtic.mil/dtic/tr/fulltext/u2/a399515.pdf

18. K. A. Fisher, "The Navigation Potential of Signals of Opportunity-Based Time Difference of Arrival Measurements," Ph.D. Dissertation, Air Force Institute of Technology.

19. F. Goldenberg, "Geomagnetic Navigation Beyond the Magnetic Compass," *Record - IEEE PLANS, Position Location and Navigation Symposium*, vol. 2006, pp. 684–694, 2006.

20. V. Pasku, A. De Angelis, G. De Angelis, D. D. Arumugam, M. Dionigi, P. Carbone, A. Moschitta, and D. S. Ricketts, "Magnetic Field-Based Positioning Systems," *IEEE Communications Surveys and Tutorials*, vol. 19, no. 3, pp. 2003–2017, 2017.

21. A. Canciani and J. Raquet, "Validation of a Magnetic Anomaly Navigation Model With Flight Test Data," in *29th International Technical Meeting of the Satellite Division of the Institute of Navigation, ION GNSS 2016*, vol. 2, 2016.

22. G. Shorshi and I. Y. Bar-itzhack, "Satellite Autonomous Navigation and Orbit Determination Using Magnetometers." Proceedings of the 31st Conference on Decision and Control, Tucson, Arizona, 1992, pp. 542–548.

23. K. Kauffman and J. Raquet, "Navigation Via H-field Signature Map Correlation and INS Integration," in *IEEE National Radar Conference*

- *Proceedings.* IEEE, may 2014, pp. 1390–1395. [Online]. Available: http://ieeexplore.ieee.org/document/6875817/

24. C. Tyren, "Magnetic Terrain Navigation," Tech. Rep., 1987.

25. A. Canciani and J. Raquet, "Magnetic Anomaly Navigation Accuracy With Respect to Map Quality and Altitude," in *Institute of Navigation International Technical Meeting 2016, ITM 2016*, vol. 1, 2016.

26. J. Shockley, "Ground Vehicle Navigation Using Magnetic Field Variation," PhD Dissertation, Air Force Institute of Technology, 2012.

27. A. Canciani and J. Raquet, "Airborne Magnetic Anomaly Navigation," *IEEE Transactions on Aerospace and Electronic Systems*, vol. 53, no. 1, pp. 67–80, 2017.

28. Y. Liu, M. Wu, and H. Xie, "Iterative Multi-Level Magnetic Matching for UAV Navigation," in *The 2010 IEEE International Conference on Information and Automation.* IEEE, jun 2010, pp. 1780–1783. [Online]. Available: http://ieeexplore.ieee.org/document/5512212/

29. C. Yang, J. Strader, Y. Gu, A. Hypes, A. Canciani, and K. Brink, "Cooperative UAV Navigation using Inter-Vehicle Ranging and Magnetic Anomaly Measurements." [Online]. Available: https://arc-aiaa-org.afit.idm.oclc.org/doi/pdf/10.2514/6.2018-1595

30. H. M. Beisner, "Arbitrary Path Magnetic Navigation by Recursive Nonlinear Estimation," *Navigation, Journal of the Institute of Navigation*, vol. 16, no. 3, 1969.

31. J. Quintas, F. C. Teixeira, and A. Pascoal, "Magnetic Signal Processing Methods With Application to Geophysical Navigation of Marine Robotic Vehicles," *OCEANS 2016 MTS/IEEE Monterey, OCE 2016*, 2016.

32. M. Lager, E. A. Topp, and J. Malec, "Underwater Terrain Navigation Using Standard Sea Charts and Magnetic Field Maps," *IEEE International Conference on Multisensor Fusion and Integration for Intelligent Systems*, vol. 2017-November, no. Mfi, pp. 78–84, 2017.

33. Y. Zhou, Y. Zhang, and L. Guo, "Simulation of Geomagnetic/Inertial Integrated Navigation System," *Proceedings - 3rd International Conference on Measuring Technology and Mechatronics Automation, ICMTMA 2011*, vol. 3, pp. 253–256, 2011.

34. B. P. Morton, K. Köprübasi, and M. W. L. Thein, "Attitude Determination and Orbital Estimation Using Earth Position and Magnetic Field Vector Measurements," *Proceedings of the American Control Conference*, vol. 5, pp. 4084–4089, 2004.

35. M. Ying and S. Zhao-wei, "Small Satellite Magnetic Autonomous Orbit Determination Based on Modified UKF," in *IMACS Multiconference on "Computational Engineering in Systems Applications"(CESA), Beijing, China*, 2006, pp. 794–798.

36. A. Bellar and M. A. Si Mohammed, "An Autonomous Hybrid Navigation Filter Using Earth Magnetic Field Measurements for Low Earth Orbit Satellite," *3rd International Conference on Control, Engineering and Information Technology, CEIT 2015*, pp. 1–6, 2015.

37. K. Janschek, T. Boge, and K. Doge, "Autonomous onboard navigation system for LEO satellites using data fusion," *1999 European Control*

Conference (ECC), vol. 67, pp. 4849–4854, 1999. [Online]. Available: https://ieeexplore.ieee.org/document/7100104/

38. W. J. Hinze, R. R. B. von Frese, and A. H. Saad, *Gravity and Magnetic Exploration.* Cambridge: Cambridge University Press, 2013. [Online]. Available: http://ebooks.cambridge.org/ref/id/CBO9780511843129

39. B. Li, T. Gallagher, A. G. Dempster, and C. Rizos, "How Feasible Is the Use of Magnetic Field Alone for Indoor Positioning?" *2012 International Conference on Indoor Positioning and Indoor Navigation (IPIN)*, no. November, pp. 1–9, 2012. [Online]. Available: http://ieeexplore.ieee.org/document/6418880/

40. H.-S. Kim, W. Seo, and K.-R. Baek, "Indoor Positioning System Using Magnetic Field Map Navigation and an Encoder System," *Sensors*, vol. 17, no. 3, p. 651, 2017. [Online]. Available: http://www.mdpi.com/1424-8220/17/3/651

41. M. Zhang, T. Qing, J. Zhu, and W. Shen, "Indoor Positioning Tracking With Magnetic Field and Improved Particle Filter," *International Journal of Distributed Sensor Networks*, vol. 13, no. 11, 2017.

42. D. R. Riota, M. B. Kristanda, and M. I. Prasetiyowati, "Multi-Floor Indoor Positioning Mobile Application using Earth's Magnetic Field (Case Study: Universitas Multimedia Nusantara)," in *International Conference on New Media Studies Yogyakarta, Indonesia*, 2017, pp. 131–136.

43. A. Solin, M. Kok, N. Wahlst Om, T. B. Sc On, and S. Ark, "Modeling and Interpolation of the Ambient Magnetic Field by Gaussian Processes." [Online]. Available: https://arxiv.org/pdf/1509.04634.pdf

44. J. Haverinen and A. Kemppainen, "A Global Self-Localization Technique Utilizing Local Anomalies of the Ambient Magnetic Field," *Proceedings - IEEE International Conference on Robotics and Automation*, pp. 3142–3147, 2009.

45. H. Durrant-Whyte and T. Bailey, "Simultaneous Localization and Mapping: Part I History of the SLAM Problem," *IEEE Robotics and Automation Magazine*, pp. 99–108, 2006. [Online]. Available: http://everobotics.org/pdf/SLAMTutorial.pdf

46. C. Cadena, L. Carlone, H. Carrillo, Y. Latif, D. Scaramuzza, J. Neira, I. Reid, and J. Leonard, "Past, present, and future of simultaneous localization and mapping: Towards the robust-perception age," *IEEE Transactions on Robotics*, vol. 32, no. 6, p. 13091332, 2016.

47. S. Thrun, W. Burgard, D. Fox, and R. Arkin, *Probabilistic Robotics*, ser. Intelligent Robotics and Autonomous Agents series. MIT Press, 2005. [Online]. Available: https://books.google.com/books?id=wjM3AgAAQBAJ

48. C. Cadena, A. Dick, and I. D. Reid, "A Fast, Modular Scene Understanding System using Context-Aware Object Detection." [Online]. Available: https: //cs.adelaide.edu.au/{~}cesar/files/ICRA2015{_}ccadena.pdf

49. R. Karlsson, T. Schön, D. Törnqvist, G. Conte, F. Gustafsson, and T. B. Schön, "Utilizing Model Structure for Efficient Simultaneous Localization and Mapping for a UAV Application," 2008. [Online]. Available: http: //www.control.isy.liu.sehttp://www.control.isy.liu.se/publications.

50. T. Oh, S. Jung, S. Song, and H. Myung, "Graph-based SLAM (Simultaneous Localization And Mapping) for Bridge Inspection Using UAV (Unmanned Aerial Vehicle)." [Online]. Available: http://www.i-asem.org/publication{_} conf/asem17/5.SS/T4C.1.SS2323{_}4079F1.pdf

147

51. E. Olson, "Recognizing Places Using Spectrally Clustered Local Matches," *Robotics and Autonomous Systems*, 2009.

52. A. Eliazar and R. Parr, "DP-SLAM: Fast, Robust Simultaneous Localization and Mapping Without Predetermined Landmarks."

53. G. Grisetti, R. Kümmerle, C. Stachniss, and W. Burgard, "A Tutorial on Graph-Based SLAM." [Online]. Available: http://domino.informatik.uni-freiburg.de/teaching/ws10/praktikum/slamtutorial.pdf

54. V. Bichucher, J. M. Walls, P. Ozog, K. A. Skinner, and R. M. Eustice, "Bathymetric Factor Graph SLAM with Sparse Point Cloud Alignment," 2015. [Online]. Available: http://robots.engin.umich.edu/publications/vbichucher-2015a.pdf

55. P. Robertson, M. Frassl, M. Angermann, M. Doniec, B. J. Julian, M. Garcia Puyol, M. Khider, M. Lichtenstern, and L. Bruno, "Simultaneous Localization and Mapping for pedestrians using distortions of the local magnetic field intensity in large indoor environments," in *International Conference on Indoor Positioning and Indoor Navigation*. IEEE, oct 2013, pp. 1–10. [Online]. Available: http://ieeexplore.ieee.org/document/6817910/

56. C. Gao and R. Harle, "MSGD: Scalable Back-end for Indoor Magnetic Field-based GraphSLAM." [Online]. Available: https://www.repository.cam.ac.uk/bitstream/handle/1810/263350/Gao{_}et{_}al-2017-2017-IEEE{_}International{_}Conference{_}on{_}Robotics{_}and{_}Automation{_}{\%}28ICRA{\%}29-AM.pdf?sequence=1{\&}isAllowed=n

57. I. Vallivaara, J. Haverinen, A. Kemppainen, and J. Roning, "Magnetic field-based SLAM method for solving the localization problem in mobile robot floor-cleaning task," in *2011 15th International Conference on Advanced*

Robotics (ICAR). IEEE, jun 2011, pp. 198–203. [Online]. Available: http://ieeexplore.ieee.org/document/6088632/

58. I. Vallivaara, J. Haverinen, A. Kemppainen, and J. Röning, "Simultaneous Localization and Mapping Using Ambient Magnetic Field." [Online]. Available: http://www.ee.oulu.fi/research/bisg/files/pdf/vallivaara10mSLAM.pdf

59. M. Kok, "Scalable Magnetic Field SLAM in 3D Using Gaussian Process Maps," *Proceedings of the 20th International Conference on Information Fusion, Cambridge, UK*, 2018.

60. J. Jung, T. Oh, and H. Myung, "Magnetic field constraints and sequence-based matching for indoor pose graph SLAM," *Robotics and Autonomous Systems*, vol. 70, pp. 92–105, aug 2015. [Online]. Available: https://www.sciencedirect.com/science/article/pii/S0921889015000408

61. J. C. K. Chow, "Drift-Free Indoor Navigation Using Simultaneous Localization and Mapping of the Ambient Heterogeneous Magnetic Field," *ISPRS - International Archives of the Photogrammetry, Remote Sensing and Spatial Information Sciences*, 2017.

62. M. Wu and J. Yao, "Adaptive UKF-SLAM based on magnetic gradient inversion method for underwater navigation," in *Lecture Notes in Computer Science (including subseries Lecture Notes in Artificial Intelligence and Lecture Notes in Bioinformatics)*, vol. 9245. IEEE, jun 2015, pp. 237–247. [Online]. Available: http://ieeexplore.ieee.org/document/7152369/

63. S. M. Chaves, E. Galceran, P. Ozog, J. M. Walls, e. T. I. Eustice, Ryan M.", K. Y. Pettersen, and H. Nijmeijer, *Pose-Graph SLAM for Underwater*

Navigation. Springer International Publishing, 2017, pp. 143–160. [Online]. Available: https://doi.org/10.1007/978-3-319-55372-6_7

64. M. Liu, H. Li, and K. Liu, "Geomagnetic navigation of AUV without a priori magnetic map," *Oceans 2014 - Taipei*, no. 1, 2014.

65. J. Huang, D. Millman, M. Quigley, D. Stavens, S. Thrun, and A. Aggarwal, "Efficient, generalized indoor WiFi GraphSLAM," in *Proceedings - IEEE International Conference on Robotics and Automation*, 2011.

66. C. Reeves, *Aeromagnetic Surveys.* GEOSOFT, 2005.

67. C. Farrow and C. Farrow, "The Effect of Geomagnetic Micropulsations on MAD Systems," Tech. Rep., 1975.

68. S. Bloomer, P. Kowalczyk, J. Williams, T. Wass, and K. Enmoto, "Compensation of magnetic data for autonomous underwater vehicle mapping surveys," *2014 IEEE/OES Autonomous Underwater Vehicles, AUV 2014*, pp. 1–4, 2015.

69. W. E. Tolles and J. D. Lawson, "Magnetic compensation of MAD equipped aircraft," Airbone Instrum. Lab. Inc., Mineola, NY, USA, Rep. 201-1, Tech. Rep., 1950.

70. Q. Han, Z. Dou, X. Tong, X. Peng, and H. Guo, "A Modified Tolles Lawson Model Robust to the Errors of the Three-Axis Strapdown Magnetometer," *IEEE GEOSCIENCE AND REMOTE SENSING LETTERS, VOL. 14, NO. 3*, vol. 14, no. 3, pp. 334–338, 2017.

71. D. Liu, C. Du, M. Xia, and A. C. T.-a. Fluxgate, "Aeromagnetic Compensation Algorithm Based on Calibration of Fluxgate Measurements," *2018 Cross Strait Quad-Regional Radio Science and Wireless Technology Conference (CSQRWC)*, no. 3, pp. 1–3.

72. R. C. Smith, M. Park, and P. Cheeseman, "On the Representation and Estimation of Spatial Uncertainty," *The International Journal of Robotics Research*, vol. 5, no. 4, pp. 56–68, 1986.

73. M. Montemerlo, "FastSLAM : A Factored Solution to the Simultaneous Localization and Mapping Problem With Unknown Data Association," Ph.D. dissertation, The Robotics Institute Carnegie Mellon University, 2003.

74. K. Murphy, "Bayesian map learning in dynamic environments," *Advances in Neural Information Processing Systems (NIPS)*.

75. T. Schön, F. Gustafsson, and P.-J. Nordlund, "Marginalized Particle Filters for Mixed Linear / Nonlinear State-Space Models," *IEEE Transactions on Signal Processing*, vol. 53, no. 7, pp. 2279–2289, 2005.

76. J. S. Liu, "Metropolized independent sampling with comparisons to rejection sampling and importance sampling," *Statistics and Computing*, vol. 6, no. 2, pp. 113–119, 1996.

77. M. Ebden, "Gaussian Processes: A Quick Introduction," *arXiv e-prints*, p. arXiv:1505.02965, 2015.

78. A. Canciani and J. Raquet, "Airborne Magnetic Anomaly Navigation," *IEEE Transactions on Aerospace and Electronic Systems*, vol. 53, no. 1, 2017.

79. A. Reid, "Aeromagnetic survey design," *Geophysics*, 1980.

80. Geomag.Org. World digital magnetic anomaly map. [Online]. Available: http://geomag.org/models/WDMAM/WDMAM_NGDC_V1.1.pdf

81. I. Amidror, "Scattered data interpolation methods for electronic imaging systems: a survey," *Journal of Electronic Imaging*, vol. 11, no. 2, p. 157, 2002.

[Online]. Available: http://electronicimaging.spiedigitallibrary.org/article.aspx?doi=10.1117/1.1455013

82. G. A. Veloski, R. G. Hammack, J. I. Sams III, L. D. Wylie, and K. Heirendt, "Evaluation of the Micro-Fabricated Atomic Magnetometer Deployed From a Small Autonomous Rotorcraft for Locating Legacy Oil & Gas Wells," Tech. Rep., 2018.

83. F. Kolawole, E. A. Atekwana, S. Malloy, D. S. Stamps, R. Grandin, M. G. Abdelsalam, K. Leseane, and E. M. Shemang, "Aeromagnetic, gravity, and differential interferometric synthetic aperture radar analyses reveal the causative fault of the 3 april 2017 mw 6.5 moiyabana, botswana, earthquake," *Geophysical Research Letters*, vol. 44, no. 17, pp. 8837–8846. [Online]. Available: https://agupubs.onlinelibrary.wiley.com/doi/abs/10.1002/2017GL074620

84. "Gradient Magnetometer UAV - GEM MONARCH," 2017. [Online]. Available: http://www.gemsys.ca/wp-content/themes/gemsystems/pdf/GEM{_}MONARCH{_}UAV.pdf

85. C. Samson, P. Straznicky, J. Laliberté, R. Caron, S. Ferguson, R. Archer, and S. G. Limited, "Designing and building an unmanned aircraft system for aeromagnetic surveying," pp. 1167–1171, 2010.

86. T. A. G. S. Thompson, "Unmanned Aerial Vehicle - Fixed Wing Magnetics Survey System (UAM II)." [Online]. Available: http://www.thomsonaviation.com.au/uav/

87. Uavex, "EX-Mag^{TM}," 2019. [Online]. Available: https://www.uavex.com/drone-magnetic-surveying

88. Geoscan, "Geoscan 401." [Online]. Available: https://www.geoscan.aero/en/products/geoscan401/geophysics

89. M. S. Huq, R. Forrester, M. Ahmadi, and P. Straznicky, "Short Papers Magnetic Characterization of Actuators for an Unmanned Aerial Vehicle," *IEEE/ASME Transactions on Mechatronics*, vol. 20, no. 4, pp. 1986–1991, 2015.

90. C. Zhiwen, C. Dongsheng, Y. Fei, W. Haijuan, and Z. Zhihui, "EMI suppression of UAV power in aeromagnetic survey," *IEEE Electromagnetic Compatibility Magazine*, vol. 2, pp. 45–53, 2013.

91. S. Cherkasov and D. Kapshtan, "Unmanned aerial systems for magnetic survey," in *Drones*, G. Dekoulis, Ed. Rijeka: IntechOpen, 2018, ch. 9. [Online]. Available: https://doi.org/10.5772/intechopen.73003

92. B. Sterligov and S. Cherkasov, "Reducing Magnetic Noise of an Unmanned Aerial Vehicle for High-Quality Magnetic Surveys," *International Journal of Geophysics*, 2016.

93. H. Li, J. Ge, H. Dong, X. Qiu, W. Luo, H. Liu, Z. Yuan, J. Zhu, and H. Zhang, "Aeromagnetic compensation of Rotor UAV Based on Least Squares," *2018 37th Chinese Control Conference (CCC)*, pp. 10 248–10 253, 2018.

94. Geometrics INC., "MFAM Development Kit User Guide," Tech. Rep., 2018.

95. R. Zhang, K. Smith, and R. Mhaskar, "Highly sensitive miniature scalar optical gradiometer," *Proceedings of IEEE Sensors*, vol. 1, pp. 1–3, 2017.

96. T. N. Lee and A. J. Canciani, "Aerial Simultaneous Localization and Mapping by the Earth 's Magnetic Anomaly Field," in *Institute of Navigation Interchange Technical Meeting 2019*, 2019, pp. 1–15.

97. ——, "Flight Test Results for an Unmanned Aerial Magnetic Surveying Vehicle," 2019.

98. Geometrics. (2016) G-823a cesium magnetometer. [Online]. Available: {http://www.tez.com.tr/media/G823A05.pdf}

99. S. H. Bickel, "Small signal compensation of magnetic fields resulting from aircraft maneuvers," *IEEE Transactions on Aerospace and Electronic Systems*, 1979.

REPORT DOCUMENTATION PAGE

Form Approved
OMB No. 0704–0188

1. REPORT DATE *(DD–MM–YYYY)*	2. REPORT TYPE	3. DATES COVERED *(From — To)*
03–21–2019	Master's Thesis	Sept 2017 — Mar 2019

4. TITLE AND SUBTITLE

Aerial Simultaneous Localization and Mapping Using Earth's Magnetic Anomaly Field

5a. CONTRACT NUMBER

5b. GRANT NUMBER

5c. PROGRAM ELEMENT NUMBER

6. AUTHOR(S)

1st Lieutenant Taylor N. Lee

5d. PROJECT NUMBER

5e. TASK NUMBER

5f. WORK UNIT NUMBER

7. PERFORMING ORGANIZATION NAME(S) AND ADDRESS(ES)

Air Force Institute of Technology
Graduate School of Engineering and Management (AFIT/EN)
2950 Hobson Way
WPAFB OH 45433-7765

8. PERFORMING ORGANIZATION REPORT NUMBER

AFIT-ENG-MS-19-M-039

9. SPONSORING / MONITORING AGENCY NAME(S) AND ADDRESS(ES)

Intentionally Left Blank

10. SPONSOR/MONITOR'S ACRONYM(S)

11. SPONSOR/MONITOR'S REPORT NUMBER(S)

12. DISTRIBUTION / AVAILABILITY STATEMENT

DISTRIBUTION STATEMENT A:
APPROVED FOR PUBLIC RELEASE; DISTRIBUTION UNLIMITED.

13. SUPPLEMENTARY NOTES

14. ABSTRACT

Aerial magnetic navigation has been shown to be a viable GPS-alternative, but requires a prior-surveyed magnetic map. The miniaturization of atomic magnetometers extends their application to small aircraft at low altitudes where magnetic maps are especially inaccurate or unavailable. This research presents a simultaneous localization and mapping (SLAM) approach to constrain the drift of an inertial navigation system (INS) without the need for a magnetic map. The filter was demonstrated using real measurements on a professional survey flight, and on an AFIT unmanned aerial vehicle.

15. SUBJECT TERMS

LaTeX,Thesis

16. SECURITY CLASSIFICATION OF:

a. REPORT	b. ABSTRACT	c. THIS PAGE
U	U	U

17. LIMITATION OF ABSTRACT

UU

18. NUMBER OF PAGES

170

19a. NAME OF RESPONSIBLE PERSON
Captain Aaron Canciani, PhD, AFIT/ENG

19b. TELEPHONE NUMBER *(include area code)*
(937) 255-3636, x4618; aaron.canciani@afit.edu

Standard Form 298 (Rev. 8–98)
Prescribed by ANSI Std. Z39.18